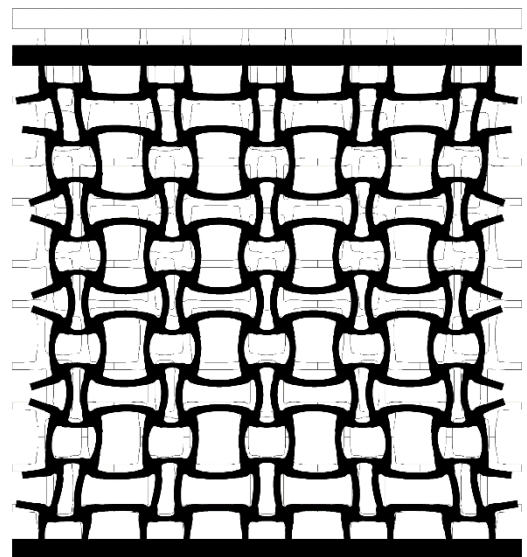
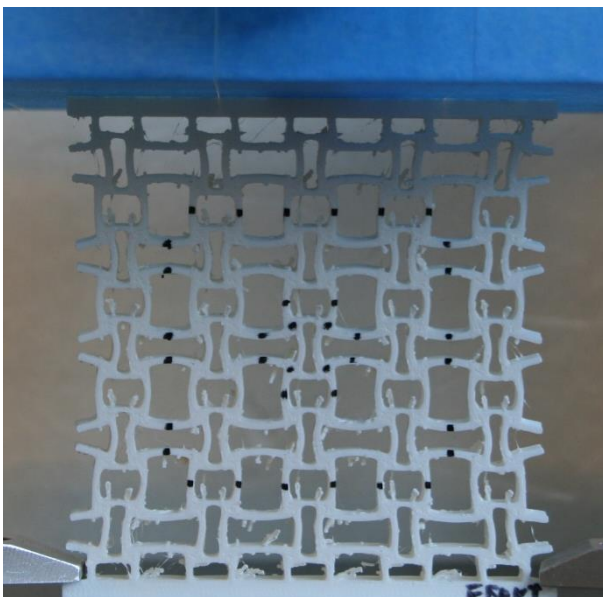


## Department of Precision and Microsystems Engineering

### Mechanical Metamaterials by Topology Optimization

G. Blokland (Geert)

Report no : 2019.040  
Coach : Ir. S. Koppen  
Professor : Dr. Ir. M. Langelaar  
Specialisation : Structural Optimization and Mechanics (SOM)  
Type of report : Master Thesis  
Date : 4 December 2019





# Mechanical Metamaterials by Topology Optimization

Generation, fabrication and validation of auxetic mechanical metamaterials

by

G. Blokland

to obtain the degree of Master of Science  
at the Delft University of Technology,  
to be defended publicly on 4 December 2019 at 13:00.

Student number: 4318978  
Project duration: 7 January 2019 – 4 December 2019  
Thesis committee: Dr. ir. M. Langelaar TU Delft, HTE  
Dr. ir. R.A.J. van Ostayen TU Delft, HTE  
Ir. S. Koppen TU Delft, HTE  
Dr. ir. J. de Vreugd TNO  
Dr. ir. H.C.B. Florijn TNO

An electronic version of this thesis is available at <http://repository.tudelft.nl/>.

# Preface

Before you lies the thesis 'Mechanical Metamaterials by Topology Optimization', which consists of an extensive research towards the generation, fabrication and validation of materials with exceptional properties, metamaterials. A huge variety of topics are covered in this thesis: finite elements, optimization, validation by simulations and experimental testing in practice. So, both fundamental mechanics, as well mechanical aspects in practice are thoroughly investigated and reported. Initially, this project starts at the TU Delft and while the project advances I got the opportunity to do part of my research at the TNO department Optomechatronics.

However, this thesis work could not be accomplished by the support of supervisors and external staff. Firstly, I would like to say thanks to my supervisors, Matthijs en Stijn for their critical altitude during progress meetings and keep me sharp during the writing phase. Both, engineering (hard) and soft skills have been improved, for which I am grateful.

Also, I would like to thanks Jan en Bastiaan to give me the opportunity to do part of my research at TNO. Your critical thoughts and relevant reviews significantly contribute to the professionalism of this thesis work.

Moreover, I enormously would like to thanks the study mates from 'The PME office' for mental and physical support during my graduation period. Next to in-dept discussions and suggestions, also relaxing moments occurred, which usually gave me an energy-boost.

Finally, I am grateful for the support and interest friends and family showed during my graduation period. It was nice to observe that 'outsiders' do show interest (by asking curious and thoughtful questions) in the field of mechanical metamaterials.

*Geert Blokland  
November 2019*

# Contents

|          |                                                                 |           |
|----------|-----------------------------------------------------------------|-----------|
| <b>1</b> | <b>Introduction</b>                                             | <b>7</b>  |
| 1.1      | Background                                                      | 7         |
| 1.2      | Mechanical metamaterials                                        | 7         |
| 1.3      | Auxetic structures                                              | 9         |
| 1.4      | Design approach                                                 | 9         |
| 1.5      | Problem definition                                              | 11        |
| 1.5.1    | Validation of mechanical metamaterials                          | 11        |
| 1.5.2    | Research scope                                                  | 12        |
| 1.6      | Outline                                                         | 12        |
| <b>2</b> | <b>Design by topology optimization</b>                          | <b>14</b> |
| 2.1      | Homogenization                                                  | 14        |
| 2.2      | From numerical homogenization to a homogenized stiffness tensor | 15        |
| 2.3      | Towards auxetic designs with TO                                 | 16        |
| 2.4      | Optimization formulation                                        | 17        |
| <b>3</b> | <b>Numerical implementation</b>                                 | <b>18</b> |
| 3.1      | Objective function                                              | 18        |
| 3.2      | Periodic boundary conditions                                    | 19        |
| 3.2.1    | Numerical solutions                                             | 20        |
| 3.3      | Optimization settings                                           | 21        |
| 3.4      | Condition initial density field                                 | 21        |
| 3.5      | Results                                                         | 21        |
| 3.6      | Comparison to reported designs                                  | 23        |
| <b>4</b> | <b>Numerical validation</b>                                     | <b>24</b> |
| 4.1      | Motivation                                                      | 24        |
| 4.2      | Methodology and assumptions                                     | 25        |
| 4.3      | Measuring the Poisson's ratio                                   | 26        |
| 4.3.1    | Energy method                                                   | 26        |
| 4.3.2    | Strain method                                                   | 27        |
| 4.3.3    | Comparison                                                      | 27        |
| 4.4      | System size effects                                             | 29        |
| 4.4.1    | Observations                                                    | 30        |
| 4.4.2    | Discussion of observations                                      | 31        |
| 4.5      | Physical testing simulations                                    | 32        |
| 4.5.1    | Observations for varying boundary conditions                    | 32        |
| 4.5.2    | Compression test modeling with fixed boundaries                 | 33        |
| 4.6      | Conclusions                                                     | 36        |
| <b>5</b> | <b>Physical experiments</b>                                     | <b>37</b> |
| 5.1      | Additive Manufacturing                                          | 37        |
| 5.1.1    | FDM                                                             | 37        |
| 5.1.2    | Manufacturing of designs using FDM                              | 38        |
| 5.1.3    | Manufacturing of designs using a mold of FDM                    | 40        |

|          |                                                                |           |
|----------|----------------------------------------------------------------|-----------|
| 5.2      | Notch flexures testing . . . . .                               | 41        |
| 5.2.1    | Design procedure . . . . .                                     | 41        |
| 5.2.2    | Experimental procedure . . . . .                               | 42        |
| 5.2.3    | Notch flexure stiffness results . . . . .                      | 42        |
| 5.3      | Benchmark design testing . . . . .                             | 43        |
| 5.3.1    | Mechanism fabrication . . . . .                                | 43        |
| 5.3.2    | Experimental procedure . . . . .                               | 44        |
| 5.3.3    | Compliant mechanism testing results . . . . .                  | 45        |
| 5.4      | Auxetic structures testing . . . . .                           | 46        |
| 5.4.1    | Experimental procedure . . . . .                               | 46        |
| 5.4.2    | Image processing . . . . .                                     | 46        |
| 5.4.3    | Results . . . . .                                              | 48        |
| 5.4.4    | Non-auxetic behavior . . . . .                                 | 51        |
| 5.4.5    | Influence of measuring location . . . . .                      | 51        |
| 5.4.6    | Clamping aspects . . . . .                                     | 52        |
| <b>6</b> | <b>Discussion</b>                                              | <b>53</b> |
| 6.1      | Optimization . . . . .                                         | 53        |
| 6.2      | Manufacturing . . . . .                                        | 54        |
| 6.3      | Numerical validation . . . . .                                 | 54        |
| 6.3.1    | Geometrically non-linear effects . . . . .                     | 54        |
| 6.3.2    | Asymmetry of auxetic designs . . . . .                         | 54        |
| 6.4      | Experiments . . . . .                                          | 55        |
| <b>7</b> | <b>Conclusions</b>                                             | <b>56</b> |
| <b>8</b> | <b>Outlook</b>                                                 | <b>59</b> |
|          | <b>Appendices</b>                                              | <b>61</b> |
| <b>A</b> | <b>Derivations of design sensitivities</b>                     | <b>62</b> |
| A.1      | Design sensitivities for minimal compliance . . . . .          | 62        |
| A.2      | Design sensitivities for maximal output displacement . . . . . | 63        |
| <b>B</b> | <b>Mesh convergence of auxetic unit cells</b>                  | <b>64</b> |
| <b>C</b> | <b>Auxetic structures comparison</b>                           | <b>66</b> |
| <b>D</b> | <b>Notch flexures</b>                                          | <b>67</b> |
| <b>E</b> | <b>Design of a compliant inverter</b>                          | <b>69</b> |

# Acronyms

|       |                                                      |
|-------|------------------------------------------------------|
| AM    | Additive Manufacturing. 12, 38, 60                   |
| BVOH  | Butenediol Vinyl Alcohol Co-polymer. 41              |
| CAD   | Computer-aided design. 38                            |
| DoF's | Degrees of Freedom. 11, 67                           |
| FDM   | Fused Deposition Modeling. 38, 42, 59, 60            |
| FEA   | Finite Element Analysis. 19                          |
| FEM   | Finite Element Modeling. 25                          |
| MMA   | Method of Moving Assymptotes. 19, 22                 |
| PBC   | Periodic Boundary Conditions. 11, 20–22              |
| PDMS  | Polydimethylsiloxane. 40, 41, 49, 56, 59             |
| PLA   | polylactic acid. 42, 43                              |
| SIMP  | Solid Isotropic Material with Penalization. 18, 70   |
| TO    | Topology Optimization. 11–14, 22, 38, 58, 60, 61, 70 |

# Symbols

|                            |                                                                                  |
|----------------------------|----------------------------------------------------------------------------------|
| $E_0$                      | solid material Young's modulus. 18                                               |
| $E_e$                      | element Young's modulus. 18                                                      |
| $E_{\min}$                 | minimal Young's modulus. 18                                                      |
| $V_{\max}$                 | volume upper bound. 18, 22, 70                                                   |
| $c_{ijkl}^H$               | homogenized stiffness tensor. 16                                                 |
| $C_{ij}^H$                 | homogenized stiffness matrix. 17–19                                              |
| $c_{pqrs}$                 | stiffness tensor. 16                                                             |
| $\Omega$                   | unit cell domain. 16                                                             |
| $\varepsilon_{ij}^*$       | fluctuation strain. 16                                                           |
| $\varepsilon_{pq}^{A(ij)}$ | superimposed strain field. 16                                                    |
| $\varepsilon_{ij}^0$       | test strain. 16                                                                  |
| $\varepsilon_u$            | applied uniaxial strain for auxetic design validation. 26, 34, 47–49, 51, 53, 56 |
| $\varepsilon_{ij}$         | strain applied on the material. 16                                               |
| $\mathbf{F}$               | global force vector. 21, 63, 64, 70                                              |
| $\mathbf{k}_0$             | element stiffness matrix with unit Young's modulus. 18                           |
| $\mathbf{k}_e$             | element stiffness matrix. 16, 18                                                 |
| $\mathbf{K}$               | global stiffness matrix. 21, 63, 64, 70                                          |
| $f$                        | objective function. 18, 19, 63, 64, 70                                           |
| $p$                        | penalization factor. 18                                                          |
| $\mathbf{u}_e^{A(kl)}$     | element displacement vector. 16, 18                                              |
| $\mathbf{u}_e^{A(ij)}$     | element displacement vector. 16, 18                                              |
| $\mathbf{u}$               | global displacement vector. 18, 21, 22, 63, 64, 70                               |
| $v_e$                      | element volume. 18                                                               |
| $\rho_e$                   | design variable. 18, 70                                                          |
| $\rho$                     | vector of design variables. 63, 64                                               |

# Chapter 1

## Introduction

### 1.1 Background

To protect the human body against external attacks protection devices are needed. For example, soldiers in the army must be equipped with an armor that absorbs the energy of a shot bullet. Such protecting devices are usually made out of high-tech fibers, preferably with a low mass and high stiffness. However, their functionality is limited by material properties. Similar, an impact is also present during walking or running. The shoe touches the ground for a while and the sole absorbs the impact. The shoe's sole is often made out lightweight materials, like *e.g.* rubber. However, such a material will readily change in shape and is disadvantageous for absorbing the energy during an impact [24]. For structural engineering purposes, the functionality of mechanisms and structures can be exploited by tuning the material properties. Common materials are limited by their *natural* properties which limit the energy absorption or the possibility to rapidly change in shape. So, to come up with better and more efficient solutions, materials with extraordinary properties are needed. Instead of using existing materials, materials with uncommon properties are designed. This kind of materials are called “metamaterials”, with the following definition:

**Definition 1.** *Metamaterials are engineered materials with exceptional properties usually not seen in nature. They derive their unusual properties from their architecture, rather than from their composition, and are usually arranged in a repeating pattern [33].*

In various fields, like optics, acoustics, thermics and magnetics metamaterials are developed and used for certain applications. Optical metamaterials (or photonic metamaterials) are developed and exhibit of a negative refractive index [34]. This metamaterial opens prospects for the reversed Doppler effect, superlenses, optical tunnelling devices and compact resonators. Also, acoustic metamaterials are generated with an extremely negative bulk modulus at a certain frequency [19]. Materials exhibiting a negative bulk modulus seems to be stable with respect to the band gap. Recently, a thermal metamaterial is generated capable of guiding convective heat flux around an object [35]. Such a material allows the channeling of thermal energy which is beneficial for thermal cloaks or concentrators. Lastly, magnetic metamaterials find their purpose in making objects invisible: cloaking. Recently, a cloak to steer microwave frequencies around an object was constructed [28]. The results of above-mentioned authors are visualized in Figure 1.1

### 1.2 Mechanical metamaterials

The focus of this thesis is on mechanical metamaterials. Mechanical metamaterials are of high interest and seem advantageous for absorbing energy during compression. Next to energy absorption, mechanical metamaterials are beneficial for mechanical cloaking, soft robotics, filtering by opening pore shapes and fiber reinforced composites [33]. A field that is attracting increasing interests is the design of stiff and lightweight materials using *auxetic* structures.

Existing studies towards characterizing the mechanical properties are already performed and bundled in the work of Kolken *et. al* [18]. Most well-known structures are the auxetics. The term auxetics is derived from the Greek word auxetikos, which means something like “that which tends to increase” and was introduced in 1978 [40]. The formal definition goes as follows:

**Definition 2.** *A material is auxetic if and only if the material becomes thicker or thinner in transversal direction while stretched or compressed in axial direction, respectively.*

This is in contrast with stretching a common material, where a shrinkage occurs in transverse direction. An illustration for a square block of material is given in Figure 1.2. The auxetic behavior is determined by the elastic property  $\nu$ : the negative

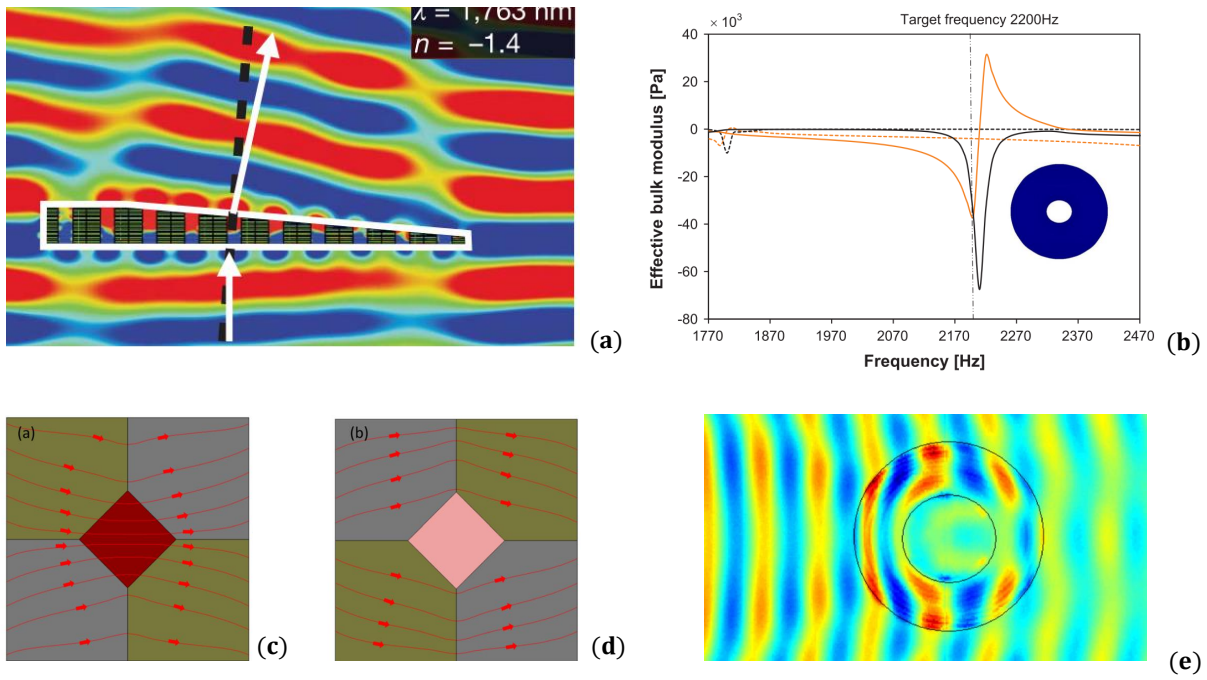


**Figure 1.1:** Metamaterials from existing literature. (a) An optical metamaterial with a negative refractive index. (b) The effective bulk modulus response of an acoustic metamaterial with corresponding unit cell. (c+d) A thermal concentrator and attractor which focuses heat towards and repels heat from an object, respectively. (e) Electric field pattern around the cloak: the cloak lies in the annular region between the black circles. The sources of (a)-(e) are [34], [19], [35], [35] and [28], respectively.

ratio between the transversal and axial strains which is called the Poisson's ratio:

$$\nu = -\frac{\epsilon_x}{\epsilon_y}. \quad (1.1)$$

For common materials, this ratio is between 0 and 0.5, with  $\nu = 0.5$  for a perfect incompressible material and while showing a very little expansion when compressed  $\nu$  is zero. Rubber has a Poisson's value of almost 0.5, while a cork consists of a Poisson's value close to 0. However, the Poisson's ratio of auxetic materials is negative and is between 0 and -0.999. An auxetic material exhibiting a Poisson's value of -1 is impossible according to Hooke's law. This law which describes a linear relationship between stresses and strains of a continuous elastic material and will have components of the elasticity tensor which are infinity in terms of magnitude for  $\nu = -1$ .

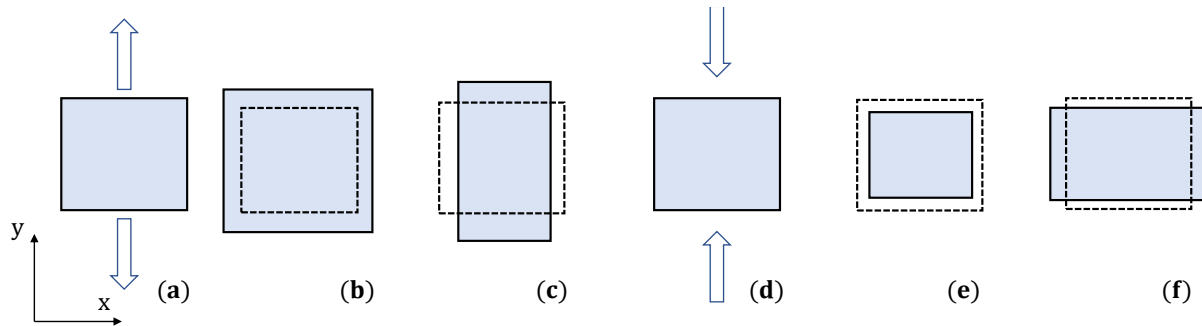


**Figure 1.2:** Stretching of a material (a) which expands (b) and shrinks (c) in transverse direction for an auxetic and non-auxetic material, respectively. Compressing of a material (d) which shrinks (e) and expands (f) for an auxetic and non-auxetic material, respectively.

### 1.3 Auxetic structures

Auxetic behavior is mainly obtained by (i) the internal geometry of the material and (ii) the way this geometry deforms. Relevant literature classify their geometry (at small scale) in several type of mechanisms: re-entrant, chiral structures and rotating structures, as in Figure 1.3. In this thesis, the focus is on the studies in the re-entrant and chiral type of mechanisms, because these geometries could be designed by a compliant mechanism design synthesis, which is fully explained in Section 1.4.

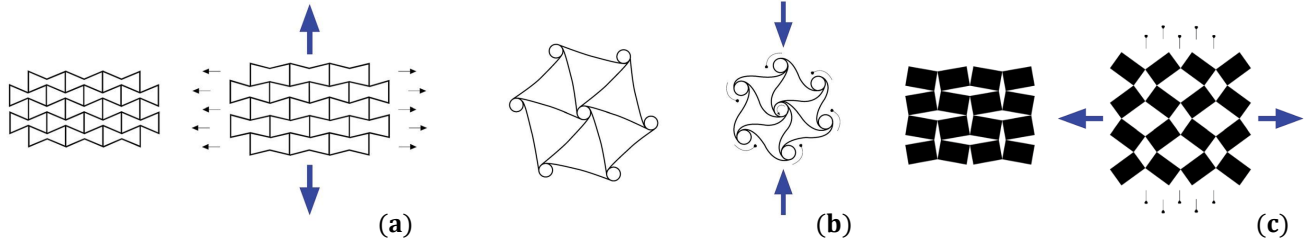


**Figure 1.3:** Unit cell geometries of a mechanical metamaterial: a re-entrant (a), chiral (b) and rotating rigid (c) structure in undeformed and deformed configuration [18]. The periodic arrangement of the mechanisms give a shrinkage or expansion of the material due to a compressive or extension load, respectively.

Re-entrant structures deform by re-alignment of the cell ribs (hinging), although deflection and axial deformation (stretching) also contribute to the auxetic behavior. These structures are beneficial in absorbing energy compared to conventional foams: indentation tests of re-entrant foams results in higher yield strengths and energy absorption than conventional foams [27]. Since the hardness of a material scales with  $\sim 1 - \nu^2$ , an absolute higher Poisson's value does decrease the indentation hardness. Such mechanical behavior is advantageous for protecting applications.

For chiral structures, rotations of the geometry cause auxetic behavior. Therefore, ligaments fold or unfold under a compressive or tensile load, respectively. This results in a rotation of the most central disk, Figure 1.3(b). The main advantages of chiral structures are: (i) the Poisson's ratio stability with respect to the applied strain, (ii) the possibility to approach a Poisson's ratios of -1 and (iii) the low sensitivity with respect to changes of the design parameters [18]. Due to their bending dominated response, these type of structures are candidates for flexible designs applications like Micro electromechanical systems (MEMS) and shape morphing structures (deployable antennas) [23]. A detailed comparison between re-entrant and chiral structures is included in Appendix C.

### 1.4 Design approach

From the previous section, the question arises: *How can these metamaterials be designed?* Therefore, inspired on the work of Gallego and Herder [11] design methods for developing auxetic structures are generated to (i) give an overview of design approaches for engineering a metamaterial and (ii) to select an appropriate design method. The design approach must be chosen such, that the following requirements are met:

**Requirement 1.** *A metamaterial must be composed of adjacent unit cells.*

One may call it a metamaterial, if and only if, the design at macro scale is composed of multiple unit cells at micro scale.

**Requirement 2.** *Unit cells must be periodically patterned in the design.*

Consequently, only one unit cell has to be designed.

**Requirement 3.** *The approach is capable of generating an auxetic design exhibiting a desired effective elastic property.*

So, the design method must be capable of generating an auxetic design which approximates a desired material property value. To avoid confusion, the following definitions are maintained throughout this report:

**Definition 3.** *A unit cell is a repeatable structure.*

**Definition 4.** *An auxetic design is an arrangement of multiple unit cells.*

**Definition 5.** *A layout is the 2D material distribution.*

Several design methods exist to come up with a mechanical metamaterial. Literature classifies a kinematic approach, a building blocks approach and an optimization approach [11] which are schematically shown in Figure 1.4. Firstly, the kinematic approaches aim to obtain designs by focusing on kinematic requirements. Desired motions are obtained by constraining or releasing Degrees of Freedom (DoF's) in the design space. Secondly, the building blocks approach splits the overall mechanism into smaller repeatable mechanisms. So, multiple compliant mechanisms perform simple functions to create compliant mechanisms that can perform more complex functions. Lastly, structural optimization approaches can be used to design metamaterials: the design is obtained by minimizing the objective while satisfying the constraints. Size, shape and topology optimization methods can be used in which sizing variables, optimal shape and layout of the architecture are optimized, respectively.

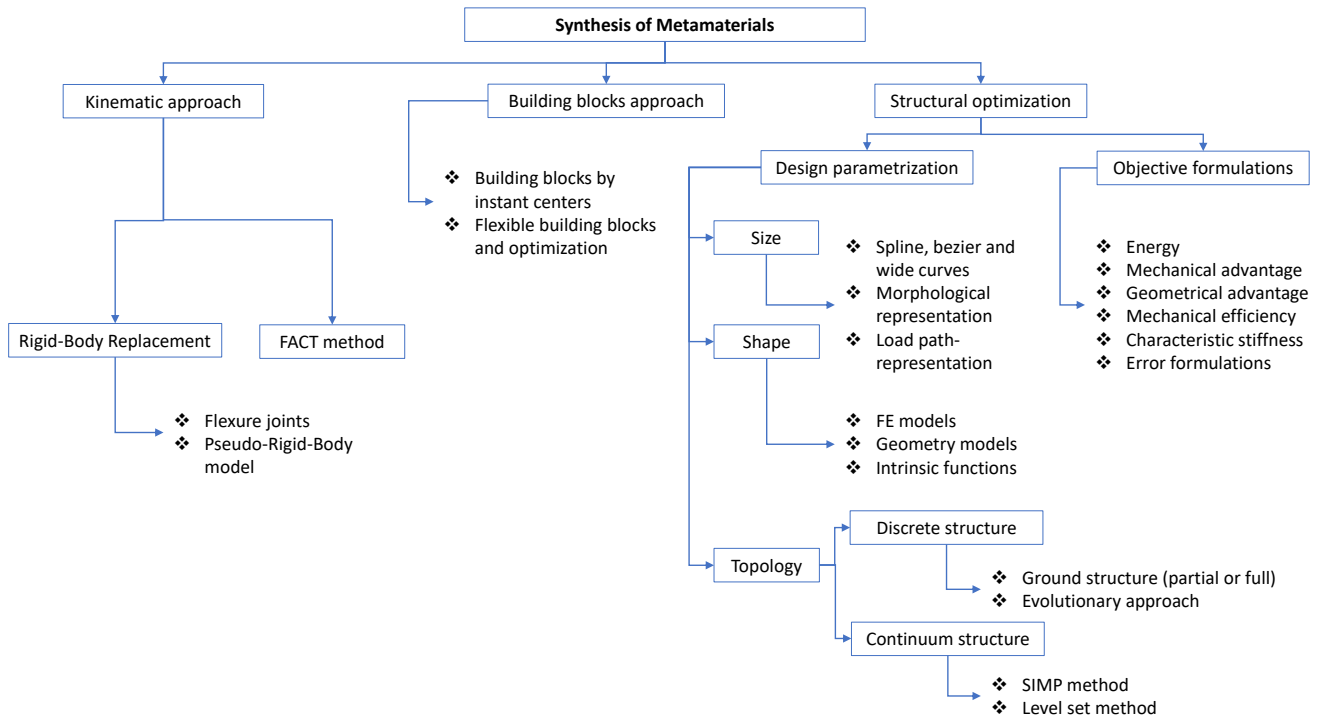


**Figure 1.4:** Design methods for mechanical metamaterials [11].

For both the building blocks as well the kinematic approach, the architecture is both challenging and limited to engineer. Moreover, both methods can fulfill the function (Requirement 3), but the final designs may not optimal. Also, achieving the combination of desired DoF's is limited for the first two approaches. Auxetic behavior is limited by the design parameters and could be enlarged using optimization strategies [2, 5, 23]. Such a strategy belongs to the structural optimization branch of Figure 1.4 and opens novel design possibilities, especially when utilizing Topology Optimization (TO). This method is used to define the topology of a structure (in a certain design domain) to obtain the best structural performance. Because of the following, TO seems beneficial to generate auxetic designs:

- TO strategies already exist (Section 1.5.1) which satisfy Requirement 1 and Requirement 2.
- Optimization strategies make use of constraints, which are beneficial to satisfy Requirement 3.
- Designing materials with TO gives an enormous design freedom.

One of the challenges is that a unit cell is optimized under Periodic Boundary Conditions (PBC) whereas in practice designs composed of a *finite number* of unit cells are employed. Ideally, an infinite amount of unit cells are used, but this is infeasible in practice. This brings the challenge to evaluate auxetic behavior of an periodic arrangement of unit cells, whereas the optimization scheme only designs one unit cell. This unit cell must be representative for the material both at micro and macro scale.

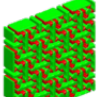
## 1.5 Problem definition

The verification of the obtained designs as introduced in Section 1.4 raises the following question: *How can it be verified that designs show auxetic behavior?* To address this question, a patch of unit cells must be arranged, fabricated and tested to validate the auxetic behavior. However, it is unclear whether from designs composed of a finite amount of unit cells the elastic properties matches the desired properties. Moreover, system size effects might be present during loading of the design. Logically, the elastic effective properties vary throughout the structure and deviations with respect to the desired value grows while tracking properties close to the outer boundaries. Therefore, numerical studies have been performed to investigate these topics. However, numerical studies prove the concept of an auxetic design under ideal conditions. There is only known that for increasing unit cells in the design, the compliance increases [25]. Numerical validation studies of auxetic designs are already proposed by , but scarcely applied [36, 48].

In this thesis, the feasibility of the optimized designs is demonstrated by utilizing Additive Manufacturing (AM) techniques and performing experiments. The focus is on AM since typical metamaterial geometries generated by TO can only be fabricated using this technology.

### 1.5.1 Validation of mechanical metamaterials

The most relevant generated mechanical metamaterials (or individual unit cells) obtained by a TO approach are shown in Table 1.1. This table shows that optimized mechanical metamaterials are neither validated numerically nor experimentally.

|                                |                                                                                   |                                                                                   |                                                                                   |                                                                                   |                                                                                    |                                                                                     |                                                                                     |                                                                                     |
|--------------------------------|-----------------------------------------------------------------------------------|-----------------------------------------------------------------------------------|-----------------------------------------------------------------------------------|-----------------------------------------------------------------------------------|------------------------------------------------------------------------------------|-------------------------------------------------------------------------------------|-------------------------------------------------------------------------------------|-------------------------------------------------------------------------------------|
|                                |  |  |  |  |  |  |  |  |
| <b>Year</b>                    | 2014 [4]                                                                          | 2015 [7]                                                                          | 2015 [16]                                                                         | 2016 [8]                                                                          | 2017 [36]                                                                          | 2018 [37]                                                                           | 2018 [43]                                                                           | 2018 [48]                                                                           |
| <b>Repeatable?</b>             | Yes                                                                               | Yes                                                                               | No                                                                                | Yes                                                                               | Yes                                                                                | Yes                                                                                 | Yes                                                                                 | Yes                                                                                 |
| <b>Experimental validated?</b> | Yes                                                                               | Yes                                                                               | No                                                                                | No                                                                                | No                                                                                 | No                                                                                  | No                                                                                  | Yes                                                                                 |
| <b>Numerical validated?</b>    | No                                                                                | No                                                                                | No                                                                                | No                                                                                | Yes                                                                                | Yes                                                                                 | Yes                                                                                 | No                                                                                  |

**Table 1.1:** Previous research towards auxetic designs in chronological sequence. Remarks: Clausen *et al.* [7] use both topology and shape optimization to optimize auxetic unit cells and in the work of Zong *et al.* [48] a two-step optimization method is utilized.

Existing literature shows that one of the first successfully 3D printed mechanical metamaterials was generated by Andreassen *et al.* [4]. Promising further research is described by Wang, which developed a 3D auxetic lattice materials with programmable Poisson's ratios [37]. Recently, Zong *et al.* published relevant findings about validation of auxetic metamaterials, however they utilized a vague described two-step optimization method [48]. The knowledge gap of fabricating and testing of mechanical metamaterials, using a TO approach is as follows:

- Shortcoming of above-mentioned research lies in both the numerical as well the experimental validation of the optimized designs. Their proposed designs are barely experimentally tested. Also, discrepancies between the mechanical response of the fabricated designs and the expected outcome are unaddressed and unexplained.
- The influences of experimental test conditions are unclear.
- For 2D structures, only re-entrant structures are experimentally investigated and chiral structures scarcely. As already discussed, chiral structures are beneficial for low Poisson's value and flexible compliant mechanisms.
- A user-friendly class of 3D printing techniques (details in Chapter 5) is hardly used for the fabrication of mechanical metamaterials and seems applicable.

## 1.5.2 Research scope

Based on the existing work and knowledge gaps from Section 1.5.1, the following research aim is defined:

**The generation and numerical and experimental validation of manufacturable and functional mechanical metamaterials using topology optimization.**

To fulfill this prospect, the following approach is defined:

**Task 1.** *Realize a TO formulation capable of optimizing unit cells;*

**Task 2.** *Exploit the possibilities of additive manufacturing for auxetic designs;*

**Task 3.** *Validate the optimized designs by performing numerical experiments;*

**Task 4.** *Validate the optimized designs by performing physical experiments.*

The scope of this thesis project is as follows:

- Only 2D structures are optimized. Subsequently, the working principles of an auxetic design can be rapidly explored, since less expensive optimizations are needed and it allows for a better understanding of the working principle of an optimized design.
- The auxetic responses of the optimized structures are valid in the linear elastic, small deflections regime. Developing an optimization method for auxetic designs for large strains and deflections is challenging and a project on itself.
- Designs which belong to the class of auxetic mechanical metamaterials are generated and tested.

The procedure to fulfill the tasks is visualized in Figure 1.5. These tasks are done in an iterative setting. Namely, knowledge of task 3 is used to execute task 4. And manufacturing results from task 2 could be improved by incorporating manufacturing aspects into the optimization, task 1. So, during the process, observations both for numerical modeling and physical experiments are reported and used for further improvements towards testing.

## 1.6 Outline

The method to generate auxetic unit cells using topology optimization is described in Chapter 2. Implementation aspects of this optimization method are reported in Chapter 3. Next, numerical validation of auxetic designs and the corresponding outcome are discussed in Chapter 4. Manufacturing aspects are discussed and explored in Chapter 5, followed by the experimental procedure and corresponding results. Finally, results are discussed (Chapter 6), conclusions are drawn (Chapter 7) and further prospects (Chapter 8) are given.

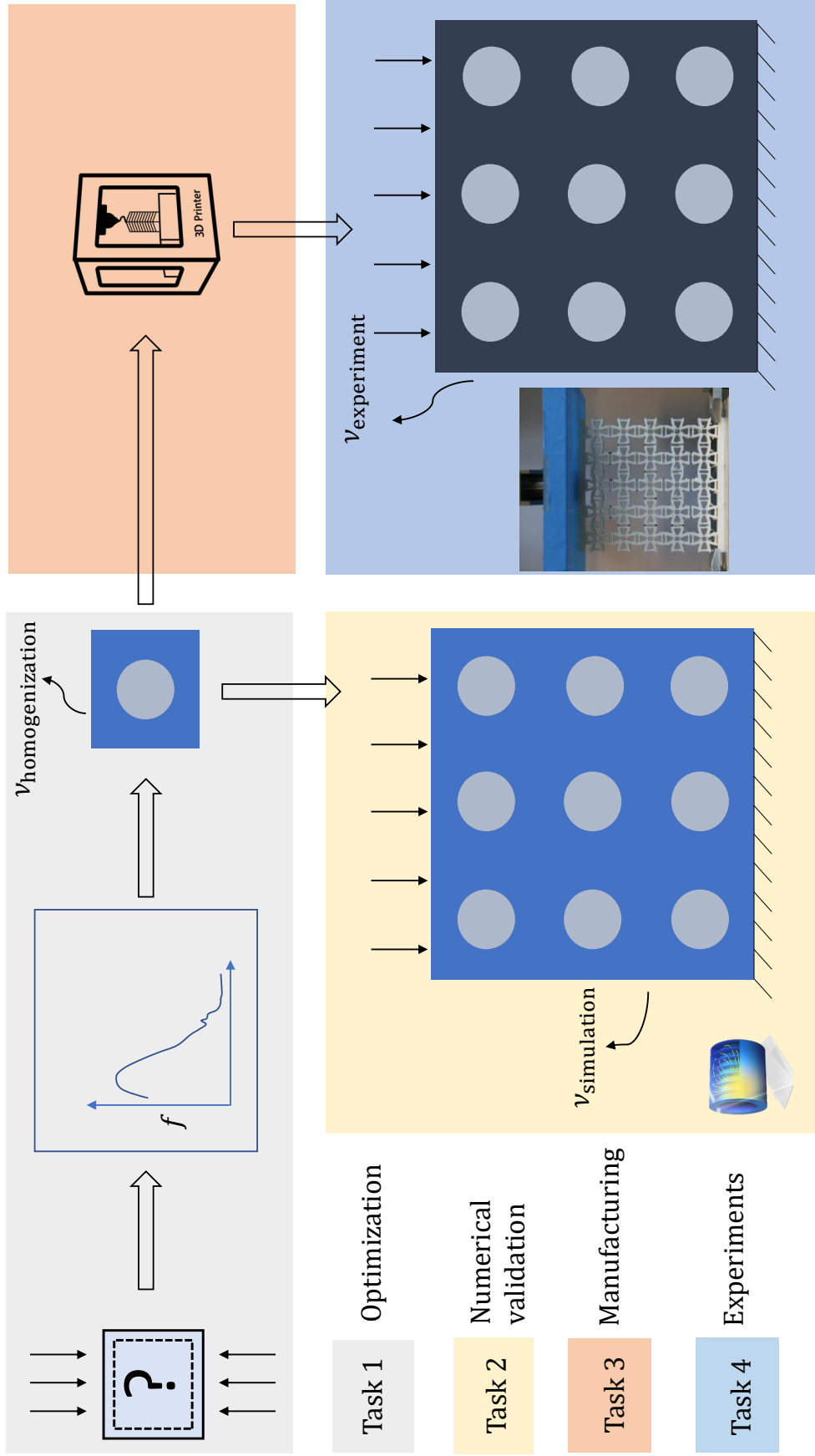


**Figure 1.5:** Approach to optimize, fabricate and validate auxetic designs during this thesis project. The final layout after optimization of the unit cell consists of a homogenized Poisson's ratio  $\nu_{homogenization}$ . The experimentally and numerically obtained Poisson's ratios ( $\nu_{experiment}$  and  $\nu_{simulation}$ ) are measured and discrepancies between those values and the homogenized values are investigated. The procedure is as follows: a unit cell with a certain Poisson's ratio is generated using TO (gray box). Thereafter, a design composed of multiple unit cells is numerically tested (yellow box) to investigate (i) the influence of boundary conditions and (ii) valid testing conditions. Finally, auxetic designs are fabricated (orange box) and they are experimentally tested (blue box). This procedure is repeated and the gathered knowledge is used to fulfill the tasks as well as possible.

## Chapter 2

# Design by topology optimization

This section motivates (i) the choice for the implemented optimization method for designing auxetic structures and (ii) forms the basis for optimized results obtained further on (Chapter 3). Firstly, a theoretical explanation of the used method is given. From there on, expressions for an objective function are derived. Finally, the complete optimization problem is formulated.

### 2.1 Homogenization

The numerical homogenization theory is applicable to obtain and analyze the homogenized elastic properties for an inhomogeneous material. This analysis is performed on a unit cell: the smallest representative volume element in a material as shown in Figure 2.1 This method is already proposed previously [14] and widely used to determine effective properties of repeatable

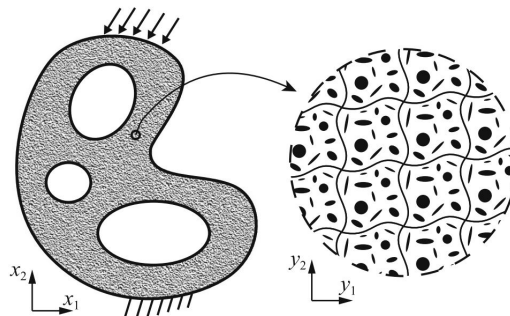


**Figure 2.1:** A material which consists of periodically arranged unit cells [41].

structures in a design. However, for the purpose of this project the (inhomogeneous) material must be ‘engineered’. In fact, a repeatable unit cell needs to be designed, exhibiting a negative Poisson’s ratio. Therefore, an ‘inverse’ homogenization approach is applied [29]. Instead of obtaining the homogenized properties, they are defined on forehand. So, given a desired material property there is searched for a structure during the optimization which has that effective property. Figure 2.2 illustrates this procedure: while requiring a negative Poisson’s value  $\nu$ , a unit cell is generated such that a material comes out which satisfies that property. To ensure the unit cell is applicable to design a material, the following requirements are defined:

1. The micro-structure needs to be periodically patterned in the bulk material.
2. The scale of the material micro structure must be significantly smaller than the scale of the material at the macro scale.

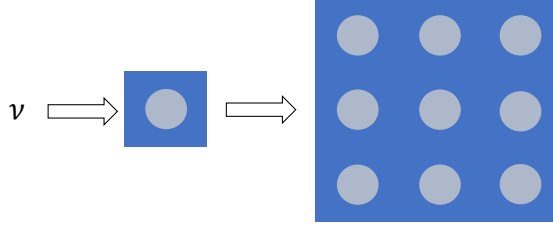


**Figure 2.2:** The 'inverse' homogenization method: for a desired Poisson's ratio a unit cell (at micro scale) is optimized towards this Poisson's value. The unit cell is repeated such that a metamaterial (at bulk scale) arises.

## 2.2 From numerical homogenization to a homogenized stiffness tensor

Starting from an asymptotic homogenization as in detail proposed [30] and already demonstrated [41], expressions for the homogenized stiffness tensor are derived. The displacement field at the micro scale can be described with respect to the size of the unit cell using an asymptotic expansion

$$u(x) = u^0(x, y) + \gamma u^1(x, y) + \gamma^2 u^2(x, y) + \text{H.O.T.}, \quad \text{using } y = \frac{x}{\gamma}, \quad (2.1)$$

where  $\gamma$  is the aspect ratio between the structures at macro and micro scale, which must be smaller than 1.  $x$  and  $y$  are the macroscopic and microscopic variables according to Figure 2.1. While considering only the first order terms of the asymptotic expansions and using the notation  $\varepsilon_{ij}^* = \frac{1}{2} \left( \frac{\partial u_i^1}{\partial x_j} + \frac{\partial u_j^1}{\partial x_i} \right)$  and  $\varepsilon_{ij}^0 = \frac{1}{2} \left( \frac{\partial u_i^0}{\partial x_j} + \frac{\partial u_j^0}{\partial x_i} \right)$  the strain fields can be written as

$$\varepsilon_{ij} = \varepsilon_{ij}(u) \approx \varepsilon_{ij}^* + \varepsilon_{ij}^0, \quad (2.2)$$

where  $\varepsilon_{ij}^*$  and  $\varepsilon_{ij}^0$  represent the average displacements over the base cell and the fluctuation strain, respectively. The homogenized stiffness tensor  $c_{ijkl}^H$  is evaluated by taking only the first order terms of the asymptotic expansion as in Equation (2.1) and averaging the integral over the base cell domain  $\Omega$  as

$$c_{ijkl}^H = \int_{\Omega} c_{pqrs} \varepsilon_{ij}(v) \varepsilon_{pq}^{*(kl)} d\Omega = \int_{\Omega} c_{pqrs} \varepsilon_{ij}(v) \varepsilon_{pq}^{0(kl)} d\Omega, \quad (2.3)$$

with  $v$  a kinematic admissible displacement field satisfying the periodic condition and  $\varepsilon_{pq}^{0(kl)}$  the test unit tensor. So,  $\varepsilon^{0(11)} = (1, 0, 0)$ ,  $\varepsilon^{0(22)} = (0, 1, 0)$ ,  $\varepsilon^{0(21)} = (0, 0, 1)$ . Equation (2.3) is rewritten expressed in terms of mutual energies

$$c_{ijkl}^H = \frac{1}{\Omega} \int_{\Omega} c_{pqrs} \varepsilon_{pq}^{A(ij)} \varepsilon_{rs}^{A(kl)} d\Omega, \quad (2.4)$$

with  $\varepsilon_{pq}^{A(ij)}$  and  $\varepsilon_{rs}^{A(kl)}$  the superimposed strain fields. The base cell is discretized into  $N$  finite elements such that the homogenized constitutive matrix can be approximated as

$$c_{ijkl}^H = \sum_{e=1}^N (\mathbf{u}_e^{A(ij)})^T \mathbf{k}_e \mathbf{u}_e^{A(kl)}, \quad (2.5)$$

with  $\mathbf{u}_e^{A(ij)}$  and  $\mathbf{k}_e$  the element displacement solutions corresponding to the test unit strains and the element stiffness matrix, respectively. The evaluated properties are only valid for linear elasticity, since only first order terms are taken into account. Reducing indices notations like  $11 \rightarrow 1$ ,  $22 \rightarrow 2$  and  $12 \rightarrow 3$  the components of the stiffness tensor are as follows for 2D cases:

$$\mathbf{C}^H = \begin{bmatrix} c_{1111}^H & c_{1122}^H & c_{1112}^H \\ c_{2211}^H & c_{2222}^H & c_{2212}^H \\ c_{1211}^H & c_{1222}^H & c_{1212}^H \end{bmatrix} \equiv \begin{bmatrix} C_{11}^H & C_{12}^H & C_{13}^H \\ C_{21}^H & C_{22}^H & C_{23}^H \\ C_{31}^H & C_{32}^H & C_{33}^H \end{bmatrix}. \quad (2.6)$$

## 2.3 Towards auxetic designs with TO

As already explained in Section 2.1, based on elastic energy terms materials are designed with desired properties. Therefore, components of the elasticity tensor must be involved in the objective function. Logically, the question arises: *How to obtain an expression for the Poisson's ratio based on components of the stiffness tensor?* Because the design problems are in the linear elastic regime, Hooke's law is used to give an expression for the effective stiffness tensor. According to Hooke's law

$$\sigma_i = C_{ij}\varepsilon_j, \quad (2.7)$$

which can be fully written for isotropic materials in matrix form by

$$\begin{bmatrix} \sigma_{11} \\ \sigma_{22} \\ \sigma_{33} \\ \sigma_{23} \\ \sigma_{13} \\ \sigma_{12} \end{bmatrix} = \frac{E}{(1-2\nu)(1+\nu)} \begin{bmatrix} 1-\nu & \nu & \nu & 0 & 0 & 0 \\ \nu & 1-\nu & \nu & 0 & 0 & 0 \\ \nu & \nu & 1-\nu & 0 & 0 & 0 \\ 0 & 0 & 0 & \frac{1-2\nu}{2} & 0 & 0 \\ 0 & 0 & 0 & 0 & \frac{1-2\nu}{2} & 0 \\ 0 & 0 & 0 & 0 & 0 & \frac{1-2\nu}{2} \end{bmatrix} \begin{bmatrix} \varepsilon_{11} \\ \varepsilon_{22} \\ \varepsilon_{33} \\ 2\varepsilon_{23} \\ 2\varepsilon_{13} \\ 2\varepsilon_{12} \end{bmatrix}. \quad (2.8)$$

Designs are obtained in 2D: thus it is assumed stresses are applied in a single frame. Therefore, plane stress conditions ( $\sigma_{33}=0$ ,  $\sigma_{23}=0$  and  $\sigma_{13}=0$ ) are used to reduce the stress-strain relation to

$$\begin{bmatrix} \sigma_{11} \\ \sigma_{22} \\ \sigma_{12} \end{bmatrix} = \frac{E}{(1-2\nu)(1+\nu)} \begin{bmatrix} 1-\nu & \nu & \nu & 0 & 0 & 0 \\ \nu & 1-\nu & \nu & 0 & 0 & 0 \\ 0 & 0 & 0 & 0 & 0 & \frac{1-\nu}{2} \end{bmatrix} \begin{bmatrix} \varepsilon_{11} \\ \varepsilon_{22} \\ \varepsilon_{33} \\ 2\varepsilon_{23} \\ 2\varepsilon_{13} \\ 2\varepsilon_{12} \end{bmatrix}. \quad (2.9)$$

Since  $\sigma_{33} = 0$ , the following relation holds from Equation (2.8).

$$\nu\varepsilon_{11} + \nu\varepsilon_{22} + (1-\nu)\varepsilon_{33} = 0 \quad (2.10)$$

Solving  $\varepsilon_{33}$  from Equation (2.10),

$$\varepsilon_{33} = -\frac{\nu\varepsilon_{11} + \nu\varepsilon_{22}}{1-\nu} \quad (2.11)$$

and inserting this relation into Equation (2.9) results in the reduced stress strain relation

$$\begin{bmatrix} \sigma_{11} \\ \sigma_{22} \\ \sigma_{12} \end{bmatrix} = \frac{E}{(1-\nu^2)} \begin{bmatrix} 1 & \nu & 0 \\ \nu & 1 & 0 \\ 0 & 0 & \frac{1-\nu}{2} \end{bmatrix} \begin{bmatrix} \varepsilon_{11} \\ \varepsilon_{22} \\ 2\varepsilon_{12} \end{bmatrix}. \quad (2.12)$$

From Equation (2.6) and Equation (2.12), the homogenized components  $C_{ij}^H$  can be expressed as

$$\begin{bmatrix} C_{11}^H & C_{12}^H & C_{13}^H \\ C_{21}^H & C_{22}^H & C_{23}^H \\ C_{31}^H & C_{32}^H & C_{33}^H \end{bmatrix} = \frac{E}{(1-\nu^2)} \begin{bmatrix} 1 & \nu & 0 \\ \nu & 1 & 0 \\ 0 & 0 & \frac{1-\nu}{2} \end{bmatrix}, \quad (2.13)$$

from where the Poisson's value appears as the ratio between the elastic coefficients  $C_{12}^H$  and  $C_{11}^H$ .

$$\nu = \frac{C_{12}^H}{C_{11}^H} \quad (2.14)$$

## 2.4 Optimization formulation

An extensive research towards optimization approaches is out of scope for this thesis project. Therefore, most of the choices for a material interpolation function, type of optimizer and objective function are motivated by existing literature of optimizing strategies for mechanical metamaterials [41, 43]. Terms from Equation (2.14) must be incorporated into the objective function to obtain auxetic structures. The mathematical formulation of the optimization problem is defined as

$$\begin{aligned}
 & \underset{\rho}{\text{minimize}} && f(C_{ij}^H(\rho)) \\
 & \text{subject to} && \mathbf{K}\mathbf{u} = \mathbf{F} \\
 & && \frac{1}{|\Omega|} \sum_{e=1}^N v_e \rho_e \leq V_{\max} \\
 & && 0 \leq \rho_e \leq 1, \quad e = 1, \dots, N
 \end{aligned} \tag{2.15}$$

in which the components of the homogenized stiffness tensor  $C_{ij}^H$  are incorporated into the objective function  $f$  and  $\rho$  denotes the vector of design variables.  $\mathbf{K}$  denotes the global stiffness matrix and  $\mathbf{u}$  and  $\mathbf{F}$  the global displacement and external force vector, respectively. Solutions for  $\mathbf{u}$  result from cases involving the test unit strains, which are described in Chapter 3. The unit cell is discretized using first-order rectangular elements. A density-based approach is used: each element  $e$  is assigned to a density that determines the Young's modulus. The material density of the design domain is constrained by the design volume  $V_{\max}$ . The modified Solid Isotropic Material with Penalization (SIMP) scheme is used to avoid singularities in the stiffness matrix. Therein, a minimal stiffness  $E_{\min}$  is introduced and assigned to the void elements. The expression goes as

$$E_e(\rho_e) = E_{\min} + \rho_e^p (E_0 - E_{\min}), \tag{2.16}$$

with a penalization factor  $p$  to avoid intermediate densities such that black-and-white solutions arise [15]. Combining Equation (2.5) and Equation (2.16) the components of the objective function become the following

$$C_{ij}^H = (E_{\min} + \rho_e^p (E_0 - E_{\min})) \sum_{e=1}^N (\mathbf{u}_e^{A(ij)})^\top \mathbf{k}_e \mathbf{u}_e^{A(kl)}. \tag{2.17}$$

The sensitivities of the components of the objective function with respect to the design variables are calculated using an adjoint method [15] and fully derived in Appendix A.1. The result reads

$$\frac{\partial C_{ij}^H}{\partial \rho_e} = \frac{1}{|\Omega|} p \rho_e^{p-1} (E_0 - E_{\min}) (\mathbf{u}_e^{A(ij)})^\top \mathbf{k}_e \mathbf{u}_e^{A(kl)}. \tag{2.18}$$

# Chapter 3

## Numerical implementation

This section reports the choice for an objective function, the numerical implementation of periodic boundary conditions, and the optimization settings. Finally, optimized layouts are presented and discussed. The complete optimization procedure for the design of unit cells is shown in Figure 3.1.

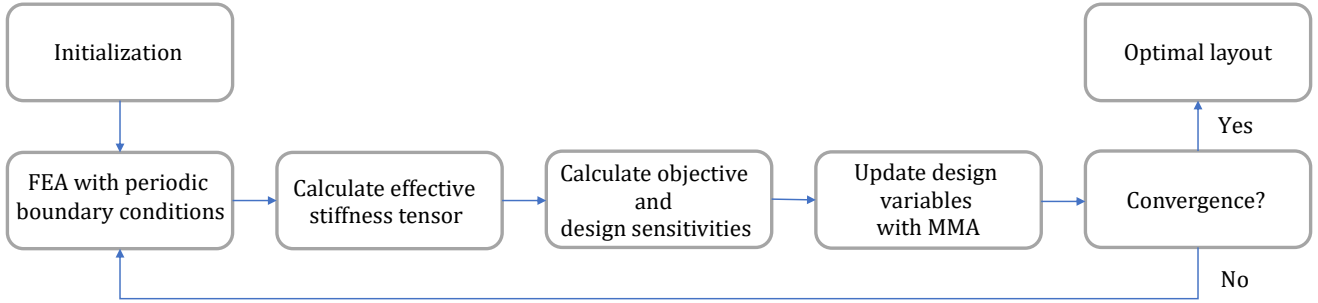


**Figure 3.1:** The optimization procedure. First, the initial values of the design variables are given. The Finite Element Analysis (FEA) with periodic boundary conditions is then performed on the unit cell. From the finite element solutions, the effective material properties, the objective function, the constraints and the corresponding sensitivities are obtained. Finally, the design variables are updated by Method of Moving Assymptotes (MMA) and the optimization continues until a convergence criterion is satisfied.

### 3.1 Objective function

Many objective functions are possible to obtain structures with a negative Poisson's ratio. For example, the objective can be defined as the minimization of the Poisson's ratio with additional isotropy constraints [4]. Zong *et al.* define the objective as a minimization of the weighted square difference between the target elasticity property and the optimized property [48]. Xia and Breitkopf propose a relaxed formulation of the objective[41], in which the components of the elasticity tensor  $C_{ij}^H$  are involved as :

$$f = C_{12}^H - \alpha^q (C_{11}^H + C_{22}^H) \quad (3.1)$$

where  $\alpha^q$  denotes the continuation function.  $q$  is set to 0.8 [41] and an exponential  $q$  is the design iteration number and changes every iteration. Figure 3.2 shows the decay of the continuation function. The optimizer tends to maximize stiffness in principal (horizontal and vertical) directions during the first iterations. When  $q$  increases,  $C_{11}^H$  and  $C_{22}^H$  becomes less dominant and the optimizer tends to minimize the value of  $C_{12}^H$ . It has been chosen to use such a type of objective function, because of the following:

- The objective function is gradually minimized such that auxetic structures arise [13].
- There is guaranteed stiffness in principal directions due to the relaxed formulation.

- Previous researchers also used this objective and it works well. When the optimizer advances, a minimization of the Poisson's value appears and the objective function goes to a stable minimum [41, 43].

The main disadvantage is that the objective will always consist of the terms  $C_{11}^H$  and  $C_{22}^H$ . For a Poisson's value optimization the term  $C_{21}^H$  needs to be optimized and small contributions of other terms means that there is no full optimization of Poisson's values. However, the relaxation term almost vanishes when the optimization advances, such that an almost complete Poisson's value optimization procedure arises.

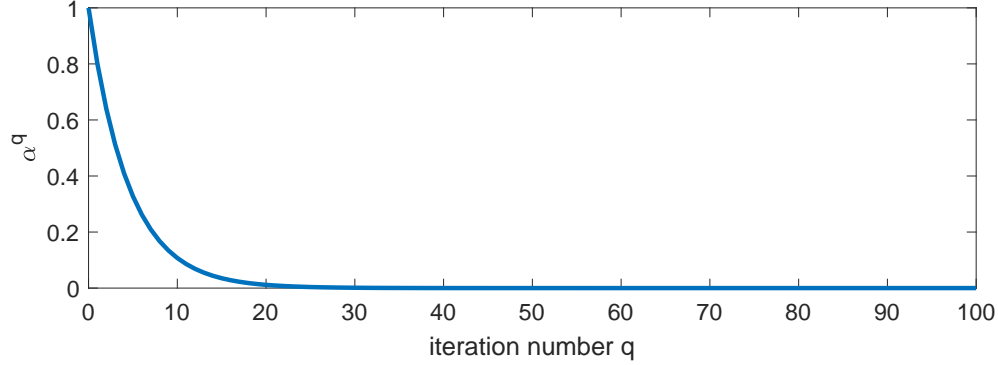


**Figure 3.2:** Curve of the continuation function. After 20 iterations,  $\alpha^q$  takes the value of 0.01, which means there is 1% contribution of elastic components in principal directions.

## 3.2 Periodic boundary conditions

The previous chapter described the idea of homogenization and how the elastic properties can be determined. It is required that the scale of the microstructure are much smaller than that of the bulk material. A crucial step is to impose periodic boundary conditions on the base cell to ensure repeatability of the unit cell throughout the design at bulk scale. Geometrical symmetry constraints are used to impose these boundary conditions. The unit cell domain  $\Omega$  is split up into pairs of negative and positive sides (Figure 3.3):  $\Omega_i^-$  and  $\Omega_i^+$  and  $\Omega_j^-$  and  $\Omega_j^+$ . For PBC, the displacement fluctuations on the negative side must be equal the corresponding ones on the positive side

$$\tilde{u}_i^- = \tilde{u}_i^+ \quad \text{on } \Omega_i \quad (3.2a)$$

and

$$\tilde{u}_j^- = \tilde{u}_j^+ \quad \text{on } \Omega_j. \quad (3.2b)$$

These conditions are valid for a kinematically admissible fluctuation field at the microscale. The displacements of the structure must be such that they satisfy the PBC and the continuity requirements. For PBC, the displacement difference between the pair of nodes on the negative side,  $u^-$ , and the positive side,  $u^+$  must be constant and are linearly linked with each other:

$$u_i^- - u_i^+ = w_i \quad (3.3a)$$

and

$$u_j^- - u_j^+ = w_j, \quad (3.3b)$$

with  $w_i$  and  $w_j$  a constant difference displacement field between opposite boundaries. Further details about this methodology can be found in an existing implementation [41]. This type of boundary conditions is directly imposed in the finite element model. By constraining the corresponding pairs of nodal displacements using a 'master-slave' (or constraint elimination) method, periodicity is guaranteed. To use such a boundary condition, the discretized base cell is separated in 4 sets of nodes, according to Figure 3.3.

Corner nodes (set 1) are defined separately to avoid redundant constraints. Opposite pairs of nodes set 3 (slave) and set 4 (master), are dependent of each other and described by a prescribed displacement field. The interior nodes (set 2) are described as an independent set of nodes. Since the nodal displacements of set 4 follows from the displacement solutions of set 3, only the nodal displacements for set 2 and set 3 need to be solved. Next, the loading scenario's are defined to solve the finite element problem. Since there are no external forces acting on the design domain, unit test strains are applied on the outer faces as shown in Figure 3.4.

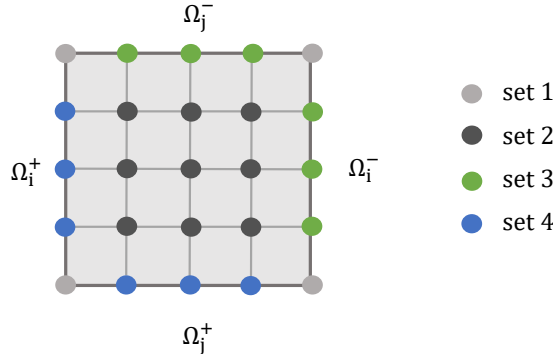


**Figure 3.3:** Discretized base cell with clustered set of nodes to impose PBC.

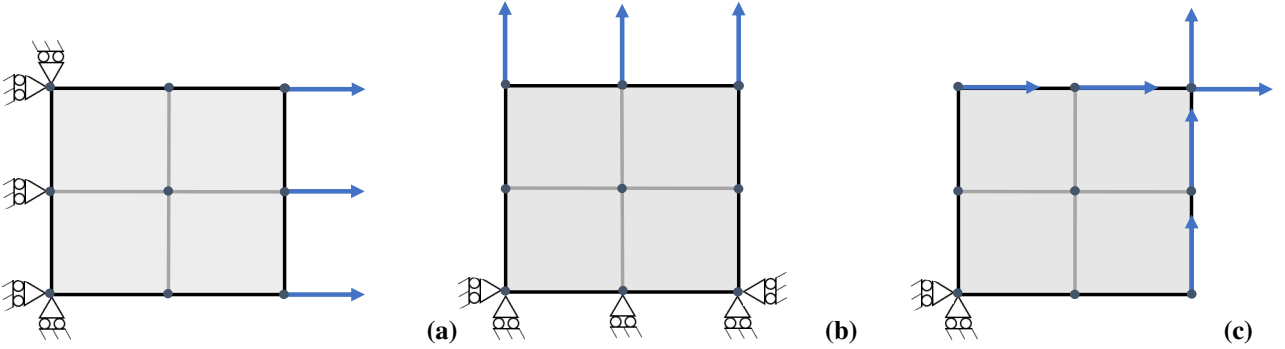


**Figure 3.4:** A discretized base cell with 2x2 elements. Test unit strains are applied corner nodes as  $\varepsilon = \{1 \ 0 \ 0\}$ ,  $\varepsilon = \{0 \ 1 \ 0\}$  and  $\varepsilon = \{0 \ 0 \ 1\}$  for configuration (a), (b) and (c), respectively.

### 3.2.1 Numerical solutions

To obtain numerical solutions based on these boundary conditions, the equilibrium equations ( $\mathbf{Ku} = \mathbf{F}$ ) are expanded in matrix notation as

$$\begin{bmatrix} \mathbf{K}_{11} & \mathbf{K}_{12} & \mathbf{K}_{13} & \mathbf{K}_{14} \\ \mathbf{K}_{21} & \mathbf{K}_{22} & \mathbf{K}_{23} & \mathbf{K}_{24} \\ \mathbf{K}_{31} & \mathbf{K}_{32} & \mathbf{K}_{33} & \mathbf{K}_{34} \\ \mathbf{K}_{41} & \mathbf{K}_{42} & \mathbf{K}_{43} & \mathbf{K}_{44} \end{bmatrix} \begin{bmatrix} \mathbf{u}_1 \\ \mathbf{u}_2 \\ \mathbf{u}_3 \\ \mathbf{u}_4 \end{bmatrix} = \begin{bmatrix} \mathbf{F}_1 \\ \mathbf{F}_2 \\ \mathbf{F}_3 \\ \mathbf{F}_4 \end{bmatrix}, \quad (3.4)$$

where the indices denote the set of nodes as defined in Figure 3.3, so  $\mathbf{u}_1$  represents the displacements of nodes in set 1,  $\mathbf{u}_2$  represents the displacements of nodes in set 2, *etc.* The system of equations can be reduced, under following assumptions:

- $\mathbf{u}_4 = \mathbf{u}_3 + \mathbf{W}$ , with  $\mathbf{W}$  a constant difference displacement between the opposite pair of boundaries;
- $\mathbf{u}_1$  is prescribed, so the first row of the stiffness matrix is redundant and is therewith eliminated;

and is reduced to

$$\begin{bmatrix} \mathbf{K}_{21} & \mathbf{K}_{22} & \mathbf{K}_{23} & \mathbf{K}_{24} \\ \mathbf{K}_{31} & \mathbf{K}_{32} & \mathbf{K}_{33} & \mathbf{K}_{34} \\ \mathbf{K}_{41} & \mathbf{K}_{42} & \mathbf{K}_{43} & \mathbf{K}_{44} \end{bmatrix} \begin{bmatrix} \mathbf{u}_1 \\ \mathbf{u}_2 \\ \mathbf{u}_3 \\ \mathbf{u}_3 + \mathbf{W} \end{bmatrix} = \begin{bmatrix} \mathbf{F}_2 \\ \mathbf{F}_3 \\ \mathbf{F}_4 \end{bmatrix}. \quad (3.5)$$

Also, the following holds:

- $\mathbf{F}_2 = 0$ , because there are no external forces acting on the interior nodes;
- $\mathbf{F}_3 + \mathbf{F}_4 = 0$ , because of the periodic displacement on the outer faces.

Adding the 2<sup>th</sup> and 3<sup>rd</sup> row of Equation (3.5), and allowing  $\mathbf{F}_2 = 0$ , the following holds:

$$\begin{bmatrix} \mathbf{K}_{21} \\ \mathbf{K}_{31} + \mathbf{K}_{41} \end{bmatrix} \mathbf{u}_1 + \begin{bmatrix} \mathbf{K}_{22} & \mathbf{K}_{23} + \mathbf{K}_{24} \\ \mathbf{K}_{32} + \mathbf{K}_{42} & \mathbf{K}_{33} + \mathbf{K}_{34} + \mathbf{K}_{43} + \mathbf{K}_{34} \end{bmatrix} \begin{bmatrix} \mathbf{u}_2 \\ \mathbf{u}_3 \end{bmatrix} + \begin{bmatrix} \mathbf{K}_{24} \\ \mathbf{K}_{34} + \mathbf{K}_{44} \end{bmatrix} \mathbf{W} = 0. \quad (3.6)$$

And finally, the unknown displacements  $\mathbf{u}_2$  and  $\mathbf{u}_3$  can be solved from Equation (3.6) and are

$$\begin{bmatrix} \mathbf{u}_2 \\ \mathbf{u}_3 \end{bmatrix} = \begin{bmatrix} \mathbf{K}_{22} & \mathbf{K}_{23} + \mathbf{K}_{24} \\ \mathbf{K}_{32} + \mathbf{K}_{42} & \mathbf{K}_{33} + \mathbf{K}_{34} + \mathbf{K}_{43} + \mathbf{K}_{34} \end{bmatrix}^{-1} \left( - \begin{bmatrix} \mathbf{K}_{21} \\ \mathbf{K}_{31} + \mathbf{K}_{41} \end{bmatrix} \mathbf{u}_1 - \begin{bmatrix} \mathbf{K}_{24} \\ \mathbf{K}_{34} + \mathbf{K}_{44} \end{bmatrix} \mathbf{W} \right). \quad (3.7)$$

### 3.3 Optimization settings

To ensure the existence of solutions, sensitivity and design filtering schemes are implemented [3]. Moreover, the formation of checkerboard patterns and mesh-dependency issues can be avoided using a density filter. A Heaviside filter is implemented to stimulate (i) black and white solutions and (ii) achieve a minimum length scale. Details about filtering are consulted from the work of Wang *et al.*[37]. Microstructures are optimized using MMA. This method allows for additional constraints onto the design variables. The optimization settings are mainly motivated by similar research in the field of generating auxetic materials by TO [4, 42, 43], and the complete list of settings is shown in Table 3.1.

| Parameter  | Setting    | Description                                                |
|------------|------------|------------------------------------------------------------|
| $N^2$      | 22500      | amount of finite elements*                                 |
| R          | 4 elements | filter radius                                              |
| $\eta$     | 0.5        | threshold value for the Heaviside projection               |
| $\beta$    | $1.05^q$   | regularization parameter of the Heaviside projection**     |
| $V_{\max}$ | 0.3        | upper volume bound of the design domain                    |
| $\alpha$   | 0.8        | fixed value of continuation part of the objective function |

**Table 3.1:** Parameter settings as used during the optimization.

\*Design domains are of equal length and width, thus discretized with  $N$  by  $N$  finite elements.

\*\* $q$  represents the iteration number and  $\beta$  is increased until it reaches the value of 20.

### 3.4 Condition initial density field

An important implementation aspect with regards to the initial layout is the initial density distribution. This defines before the optimization at which location in the design domain material is present. In common structural compliance minimization designs, the initial density field is usually uniformly distributed to avoid local minima [41]. However, this cannot be applied for the design of auxetic materials, because the PBC would result in a uniformly distributed sensitivity field. For equal sensitivities throughout the design, it is unclear for the optimizer in which direction to optimize. Consequently, an update of the design variables is impossible and this means the design variables cannot be updated. Thus, the design field (or material distribution) do not changes and remains equal. The influence of an initial guess on the final designs is recently extensively investigated [46] and to a lesser extent also by Zhang *et al.* [44]. Their work is used to exploit the possible auxetic designs for a varying initial guess. Since, chiral type of auxetic designs were scarcely generated using an energy-based topology optimization strategy, an effort has been made to generate themselves.

### 3.5 Results

The reader is reminded that the focus of this thesis is to *validate* the final designs. Parametric studies for varying optimization settings are out of scope and most of the parameter settings itself are (if needed) taken from existing literature. Therefore, only results are reported which are numerically and/or physically tested in the upcoming sections. Parameters are used as listed in Table 3.1 and the final layouts for an initial material layout are shown in Figure 3.5. Examples of the convergence towards a negative Poisson's ratio throughout the optimization is shown in Figure 3.6. A set of final layouts is chosen for further validation, while requiring different types of geometries (re-entrant and chiral) and a spread in Poisson's value magnitude ( $0 \leq \nu \leq -0.71$ ) of the unit cell.

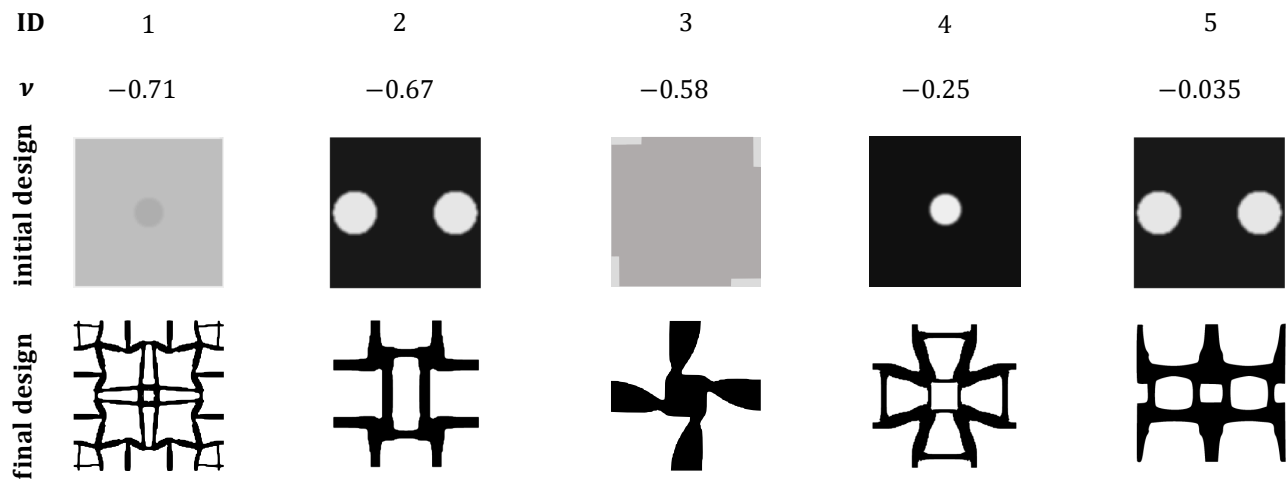
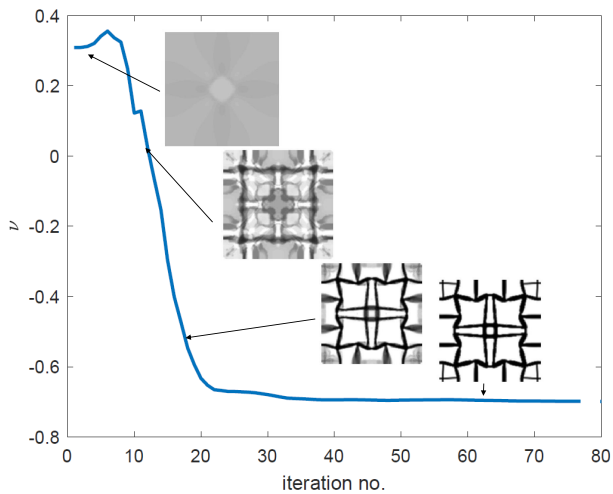
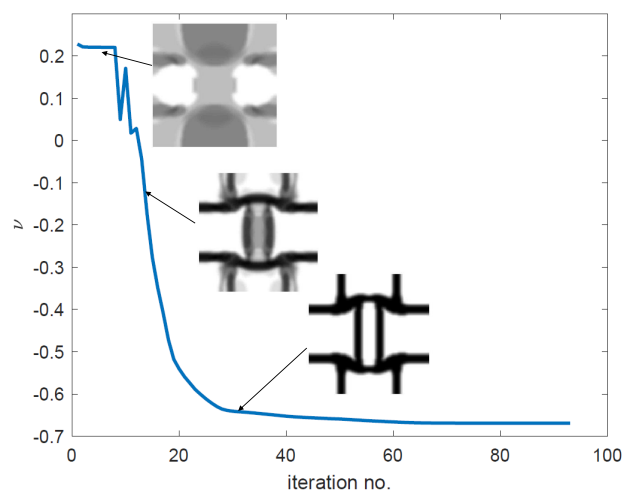


**Figure 3.5:** Initial and final density distributions of auxetic designs (most lower rows) obtained by an energy-based homogenization optimization procedure.  $\nu$  denotes the homogenized Poisson's value. Already, by a varying initial density field unit cells with different Poisson's value appear. For design ID5 a target Poisson's value has been defined at 0. Note: unit cells in this figure has been optimized by the author.



**(a)** Evolution of the Poisson's value and some snapshots of intermediate designs. Non-converged designs are picked at iteration number 2, 7, 17 en 62.



**(b)** Evolution of the Poisson's value and some snapshots of intermediate designs. Non-converged designs are picked at iteration number 5, 10 and 30.

**Figure 3.6:** Poisson's values minimization for design ID 1 and 2.

### 3.6 Comparison to reported designs

Rational design of and research towards auxetic structures is already ongoing and a variety of auxetic designs already exist and are summarized in review papers [5, 23]. From existing work, a similar layout compared to optimized layout ID2 appears. Figure 3.7 shows both layouts: the final layout shows similarities with an *anti-tetra-chiral* unit cell. Both structures are composed of 4 disks, connected to each other by slender ligaments. For a compressive load, the disks rotate towards each other such that a transverse shrinkage occurs. The main difference is that the optimized geometry consists of solid material located at the disks, whereas the geometry from literature does show cylindrical void regions at that positions. Experiments have already been carried out for the anti-tetra chiral unit cell and auxetic behavior was observed [20]. Therefore, the author predicts that this design obtained by optimization shows auxetic behavior in testing environments.

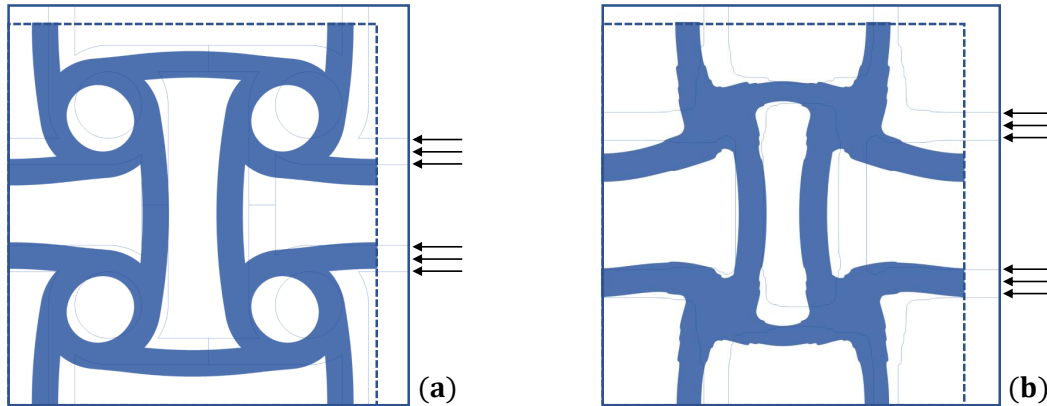


**Figure 3.7:** (a) Shrinkage of a periodic unit cell geometry copied from literature [23] and (b) generated by optimization (design ID2). Poisson's values are -0.9 and -0.67, respectively. Displacements at most left and lower boundary are constrained with rollers. The solid and dashed lines represent the boundaries of the undeformed and deformed unit cell, respectively. Deformed geometries are enlarged with a factor 3 and obtained by a linear elastic analysis.

# Chapter 4

## Numerical validation

### 4.1 Motivation

As discussed in Section 2.3, Poisson's ratios are expressed in terms energies. However, the commonly used definition of the Poisson's ratios is based on the ratio between transversal and longitudinal strains. Instead of elastic energies, strains (in the linear elastic regime) quantify this ratio. Using both measures for an identical unit cell, a difference in resulting outcome might be present. Therefore, the first question arises:

**RQ 1.** *Does a Poisson's value measured by elastic energy terms results in equivalent values compared to a Poisson's value measure based on strains?*

Note, that both measuring strategies are obtained numerically. In existing literature, this question is unanswered. Usually, the Poisson's ratio is measured by the ratio of strain for the validation of auxetic designs. For the validation of fabricated designs, this method is most applicable, because of the complexity to measure elastic energy during an experiment. However, Finite Element Modeling (FEM) is suitable to extract elastic energy terms for a loaded structure. Therefore, a study is performed towards this issue and reported in Section 4.3. The follow-up research questions mainly focus on boundary effects and system sizes; two barely investigated aspects in the field of validation and verification of Poisson's ratio for auxetic designs. To avoid confusion, the following definition is given:

**Definition 6.** *System size refers to the amount of unit cells a design is composed of.*

For a design composed of multiple unit cells, the validity of the negative Poisson's ratio is investigated by locally evaluating the auxetic behavior:

**RQ 2.** *Does the system size influences the auxetic behavior throughout the design?*

This research question also incorporates challenges concerning the utilized homogenization approach. An infinite amount of unit cells is assumed using this method, whereas only a finite amount is feasible in practice. Related to this research is the following question:

**RQ 3.** *Do different types of applied boundary conditions influence the auxetic behavior throughout the design?*

These questions are answered in this chapter (Section 4.4) and the outcome is used (i) to test the validity of the optimized designs numerically, (ii) to define a suitable setup for the physical experiment and (iii) to predict the physical test outcome. Finally, the physical test is modeled (Section 4.5) to later compare experimental and numerical obtained auxetic behavior.

## 4.2 Methodology and assumptions

Using COMSOL Multiphysics, designs are uniaxially loaded with a uniform displacement  $u_{\text{top}}$  applied at the top of the structure. In the studies, displacements are pointing downwards. Boundary conditions at the bottom of the design vary (to answer RQ 3) as shown in Figure 4.4. The following settings/assumptions are made and used during the numerical studies:

- The finite element models are discretized with four-noded elements with mesh sizes obtained from a mesh convergence study (Appendix B): the size of the elements has been chosen such that the element size do not influence the numerical outcome.
- The analysis is performed in 2D (a single frame) and plane stress conditions are applied.
- A linear elastic analysis is performed since designs are optimized for the linear elastic regime.
- Material properties for a flexible filament material are used with values of  $E = 95 \text{ MPa}$  and  $\rho = 1230 \frac{\text{kg}}{\text{m}^3}$  [1]. The material's Poisson's value denotes a typical value for a polymer,  $\nu = 0.3$  [9].
- Uniaxial strains are often plotted in graphs in this thesis work and are defined as

$$\varepsilon_u = \frac{u_{\text{top}}}{L} \cdot 100\%, \quad (4.1)$$

with  $u_{\text{top}}$  and  $L$  as in Figure 4.4.

- The homogenized value represents the Poisson's value of the final optimized layout, in this case  $\nu = -0.25$ .

To load the 2D geometry of the optimized designs into finite element software, a manual B-spline curve fitting is performed as visualized in Section 4.2. This will affect the design's performance to some extent, however a similar approach is used in literature [45] which does not show significant discrepancies in terms of Poisson's values between the fitted and optimized structure.

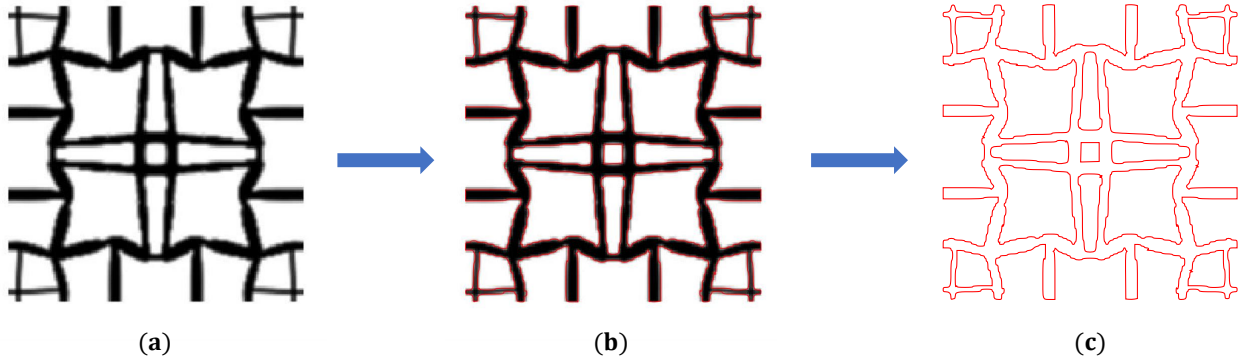


**Figure 4.1:** Example of B-spline curve fitting: the layout of the unit cell (a) is traced (b) using a density value of 0.5. The fitted contour (c) is used as geometry for the numerical studies.

### 4.3 Measuring the Poisson's ratio

RQ 1 is answered by defining and testing methods which extract Poisson's ratios based on energy terms (energy method) and strain terms (strain method). Both methods are explained in the upcoming part and are visualized in Figure 4.2. For two different geometries both methods are executed and the results are compared with each other.

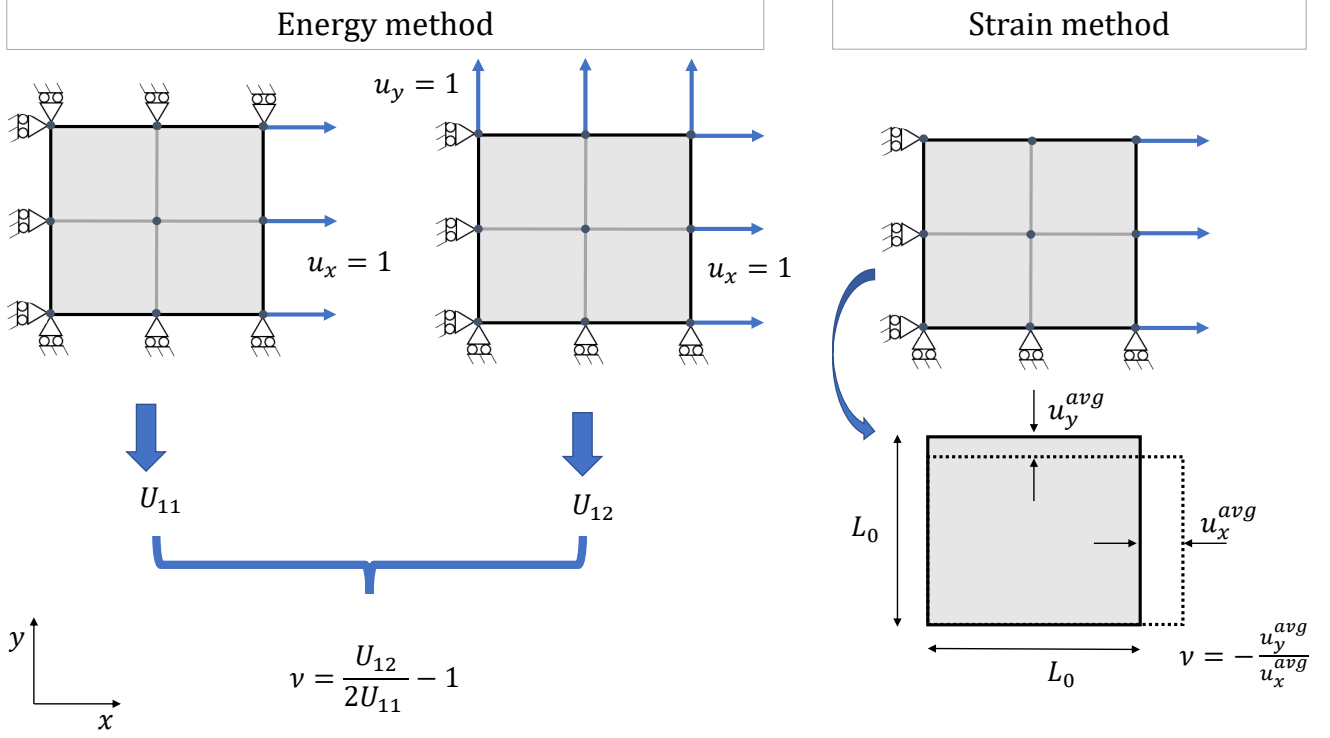


**Figure 4.2:** The procedure to determine Poisson's values for both the energy and strain method.

#### 4.3.1 Energy method

In the energy procedure, elastic strain energy terms are calculated. Therefore, uniform displacement fields in principal directions are applied at the domain faces. Loading cases as in Figure 4.2 are applied and from there on, required elastic energy terms are calculated. Using the generalized form Hooke's law which states that  $\sigma = \mathbf{C}^H \epsilon$ , the strain energy for loading in x-direction is defined as

$$U_{11} = \frac{1}{2} \int \sigma^T \epsilon_{11} d\Omega = \frac{1}{2} \int \epsilon_{11}^T (\mathbf{C}^H)^T \epsilon_{11} d\Omega. \quad (4.2)$$

For a unit volume  $\Omega = 1$ , the elastic energy is as follows

$$U_{11} = \frac{1}{2} \begin{bmatrix} 1 \\ 0 \\ 0 \end{bmatrix}^T \begin{bmatrix} C_{11}^H & C_{12}^H & C_{13}^H \\ C_{21}^H & C_{22}^H & C_{23}^H \\ C_{31}^H & C_{32}^H & C_{33}^H \end{bmatrix} \begin{bmatrix} 1 \\ 0 \\ 0 \end{bmatrix} = \frac{1}{2} C_{11}^H. \quad (4.3)$$

In a similar way, the strain energy for loading both in horizontal and vertical direction is calculated by

$$U_{12} = \frac{1}{2} \begin{bmatrix} 1 \\ 1 \\ 0 \end{bmatrix}^T \begin{bmatrix} C_{11}^H & C_{12}^H & C_{13}^H \\ C_{21}^H & C_{22}^H & C_{23}^H \\ C_{31}^H & C_{32}^H & C_{33}^H \end{bmatrix} \begin{bmatrix} 1 \\ 1 \\ 0 \end{bmatrix} = \frac{1}{2} (C_{11}^H + C_{12}^H + C_{22}^H + C_{21}^H). \quad (4.4)$$

Assuming an isotropic material,  $C_{11}^H = C_{22}^H$  and  $C_{12}^H = C_{21}^H$ , reduces Equation (4.4) to

$$U_{12} = C_{11}^H + C_{12}^H. \quad (4.5)$$

The components of the homogenized elasticity tensor can be calculated from Equation (4.3) and Equation (4.5) and are

$$C_{11}^H = 2U_{11} \quad (4.6a)$$

and

$$C_{12}^H = U_{12} - 2U_{11}. \quad (4.6b)$$

Finally, the Poisson's ratio is calculated from Equation (2.14):

$$\nu = \frac{C_{12}^H}{C_{11}^H} = \frac{U_{12}}{2U_{11}} - 1. \quad (4.7)$$

### 4.3.2 Strain method

In this method, a uniform displacement field is applied in x-direction, while constraining the normal direction by rollers as shown at the most right box in Figure 4.2. From the unconstrained boundary vertical displacements are evaluated. The engineering strains are calculated as

$$\varepsilon_x = \frac{\Delta x}{L_x} = \frac{u_x^{\text{avg}}}{L_0} \quad (4.8a)$$

and

$$\varepsilon_y = \frac{\Delta y}{L_y} = \frac{u_y^{\text{avg}}}{L_0} \quad (4.8b)$$

and consequently the Poisson's value is the following ratio

$$\nu = -\frac{\varepsilon_y}{\varepsilon_x} = -\frac{u_y^{\text{avg}}}{u_x^{\text{avg}}}, \quad (4.9)$$

with  $u_x^{\text{avg}}$  and  $u_y^{\text{avg}}$  the average displacements.

### 4.3.3 Comparison

Using finite elements, a square unit cell is modelled in 2D, with 10 mm length. The design domain is discretized into a square, four-noded, element. Under plane-stress assumptions both strategies are executed on the unit cell using COMSOL Multiphysics. Also, both strategies are executed for an auxetic structure to check whether this approach holds for more complex geometries. The deformed geometries are shown in Figure 4.3 and the calculated Poisson's values for both methods are listed in Table 4.1.

| Method | Difference to target Poisson's value in % |                   |
|--------|-------------------------------------------|-------------------|
|        | Square unit cell                          | Auxetic unit cell |
| Strain | $\mathcal{O}(10^{-10})$                   | 0.75              |
| Energy | 0                                         | 5.95              |

**Table 4.1:** Outcome from the strain and energy method. For the unit cell, a material Poisson's value of 0.3 magnitude is defined as target value. The target value of the auxetic unit cell is defined as homogenized Poisson's value,  $\nu = -0.67$  for this particular geometry.

The analysis shows that both methods results in equivalent values. The differences with respect to the target value in terms of Poisson's values for the unit cell is negligible. For the auxetic unit cell, probably the asymmetry of the unit cell itself mainly causes a difference in outcome between both methods. As a consequence, the structure might not be completely isotropic, which is in contradiction with the assumption made by the energy method (isotropic material). Nevertheless, the outcome of the strain method (which is preferable) is consistent with the target values for both methods. Thus, the answer of RQ 1 goes as follows:

*Yes, both methods result in equivalent value. Measuring strains is a valid approach to evaluate Poisson's ratios in the linear elastic regime.*

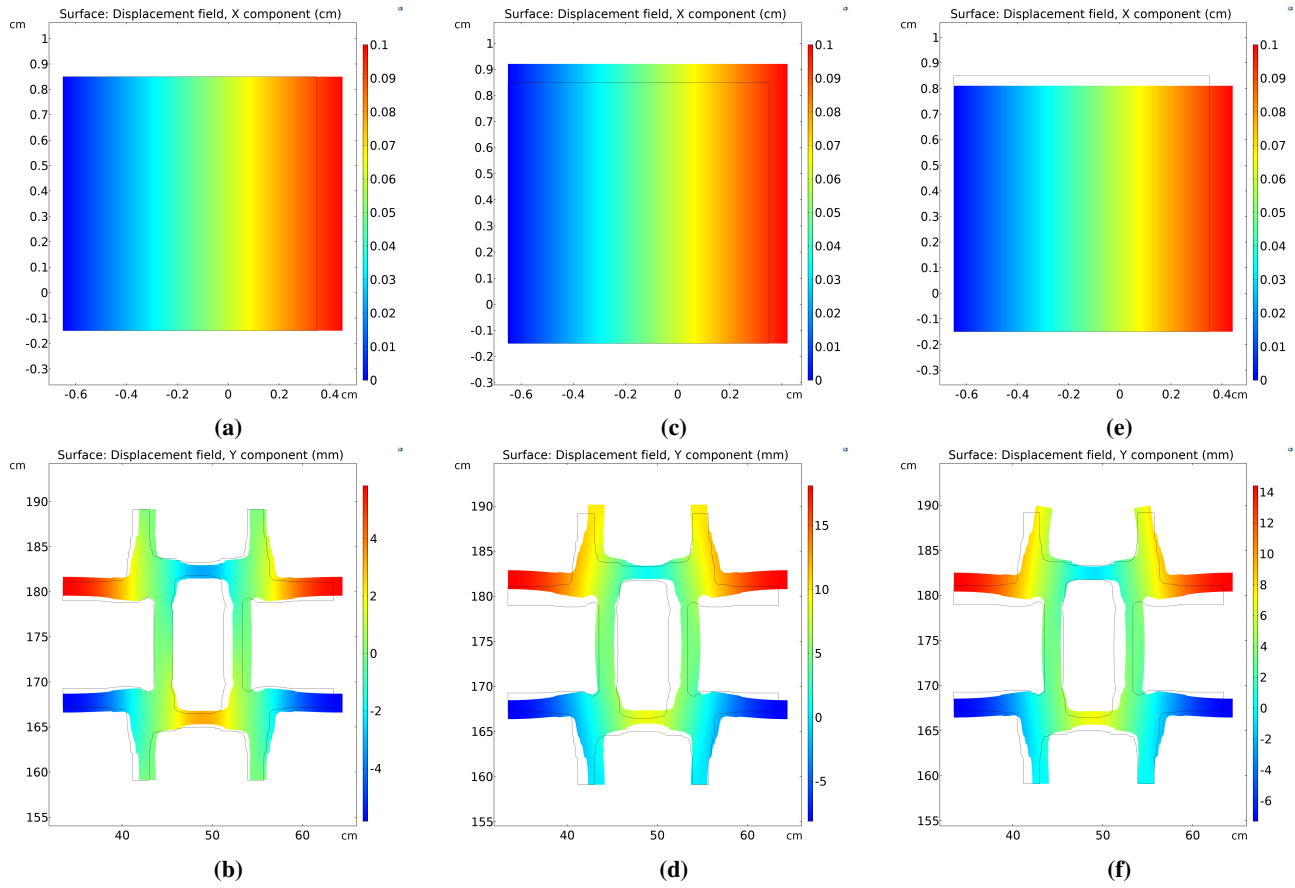


**Figure 4.3:** Deformed configuration for loading scenarios to calculate energy terms  $U_{11}$  (a-b),  $U_{12}$  (c-d) and to evaluate direct displacements for the strain method (e-f), for the unit cell and auxetic design, respectively.

## 4.4 System size effects

The questions to be answered in this section are RQ 2 and RQ 3. To answer these questions designs of  $n$  by  $n$  unit cells are uniaxially loaded with uniform displacements and boundary conditions as shown in Figure 4.4. Since the influence of the boundary conditions is unclear, two type of boundary conditions are numerically investigated. For scenario A, rollers are imposed on the most lower boundaries to constrain as little as possible, mimicking a zero friction contact. For Scenario B, the bottom part is fully fixed to the ground, mimicking a high friction contact surface. The designs are composed of  $n$  by  $n$  unit cells for  $n = 3, 5, 7, 9$  and a uniform displacement  $u_{\text{top}}$  of 1 mm is applied at the top of the structure. For each unit cell individually, Poisson's ratios are defined as the ratio of averaged displacements as illustrated in Figure 4.4 for scenario B. Poisson's ratios are in a similar method calculated for scenario A. and the corresponding expression is,

$$\nu = -\frac{\Delta\bar{x}_a - \Delta\bar{x}_c}{\Delta\bar{y}_d - \Delta\bar{y}_b} \quad (4.10)$$

with  $\bar{x}$  and  $\bar{y}$  the average displacements and sides a-d as defined in Figure 4.4.

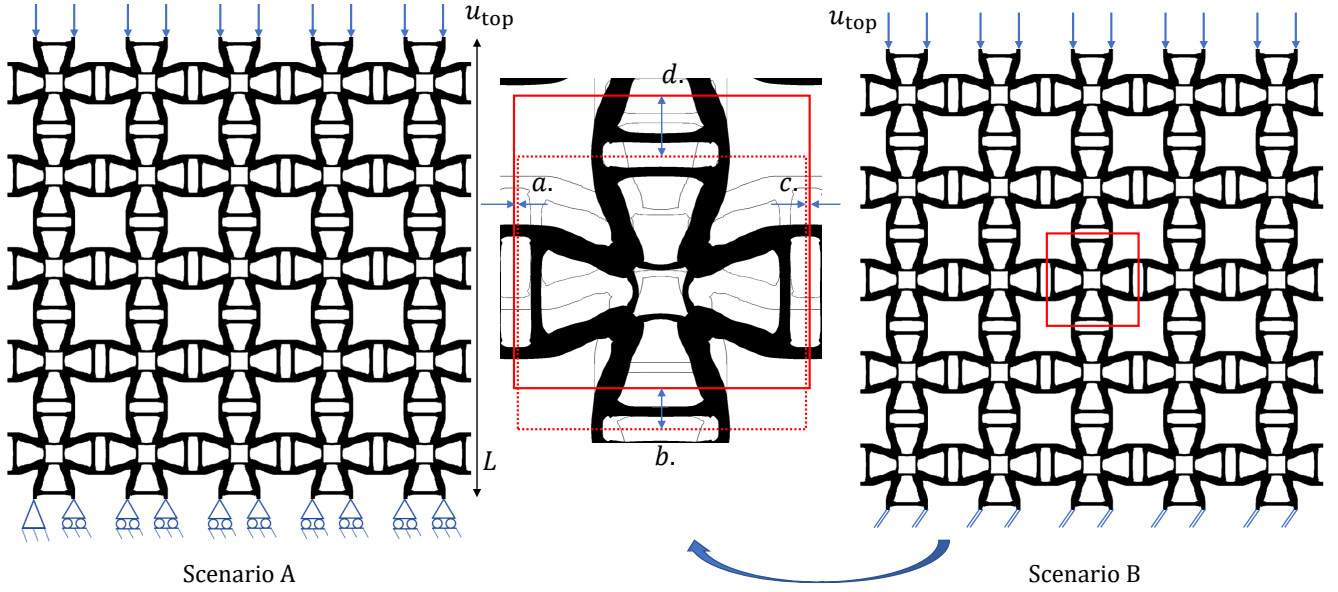


**Figure 4.4:** Loading scenario's for numerical modeling with  $n=5$  and a close-up of the most central unit cell. For scenario A, the most lower left node is fixed for adequate boundary conditions at the lower section and for scenario B the horizontal bottom lines are fixed. The filled and dashed box outline the undeformed and deformed configuration, respectively. For each individual unit cell, Poisson's values are calculated based on the ratio of displacements at the unit cell boundaries by Equation (4.10).

Following above mentioned strategy, the Poisson's value for each unit cell individually for both increasing system sizes and varying loading scenarios are plotted in Figure 4.5.

### 4.4.1 Observations

For loading scenario A, an almost constant Poisson's ratio is observed throughout the design. Small differences are present at the most left and right boundaries, probably caused by periodic constraints which are neglected. More interestingly, is the almost constant Poisson's ratio of the most inner cell for increasing system sizes. Using a small amount of unit cells, the boundary effects do not significantly influence the auxetic behavior.

Loading scenario B clearly illustrates the effect of fixed boundaries on the Poisson's value locally. Most lower unit cells suffer from the fixed boundaries and show a significantly lower Poisson's ratio compared to other locations at the design. This study also shows that unit cells positioned at the top of the structure suffer less from the boundary conditions, compared to the bottom cells. The maximal Poisson's value difference of the most central unit cell is 2%, which is the case for  $n = 9$ . For both scenarios, the most central unit cell shows an increase in Poisson's value difference for increasing system size. In comparison with scenario A, the values are less uniformly distributed throughout the designs. Whereas, a design loaded as in scenario A shows almost identical values at the most left and right side, there is no tendency to symmetries for scenario B. Relevant discussion points from this study are reported in the upcoming section.

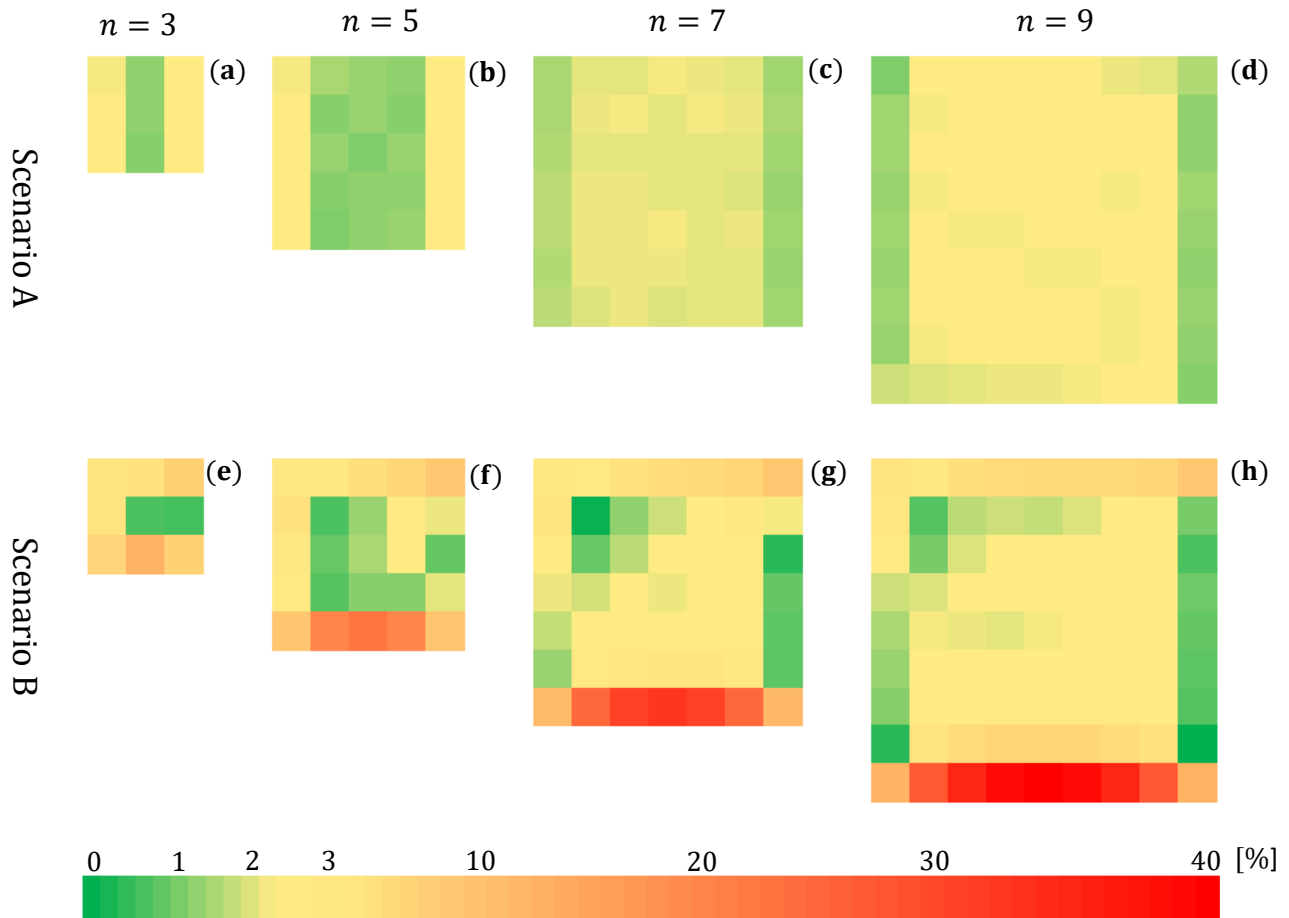


**Figure 4.5:** Magnitudes of Poisson's values differences in % with respect to the homogenized value for scenario A (a-d) and scenario B (e-h). The Poisson's ratio for each cell individually is calculated using Equation (4.10).

### 4.4.2 Discussion of observations

The asymmetric response of the auxetic design is probably caused by the asymmetry of the unit cells geometry. To investigate the asymmetric of the auxetic design, two orientations of the geometry are simulated as in Figure 4.6(a-b). The red bar indicates the orientation of the geometry: the geometry is rotated counterclockwise with 90 degrees. For a linear elastic analysis, the design is loaded on top with a uniform displacement field and Poisson's values are calculated for each cell individually as described in the previous sections. The absolute differences in terms of Poisson's values between the rotated and non-rotated orientation is shown in Figure 4.6c. The color spread in this figure shows that this particular design is quite asymmetric: a rotated geometry results in significantly different values compared with the non-rotated geometry. For a symmetric structure, one would expect that the orientation of the geometry does not influence the auxetic response. So, this numerical investigation shows that asymmetry of the geometry is present for this particular design since a spread in colors is present.

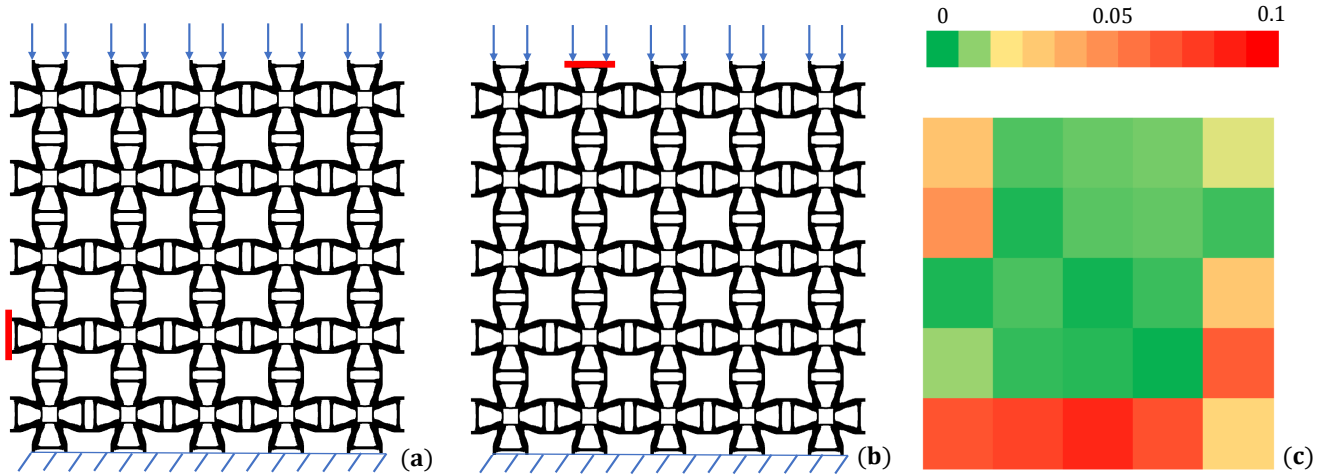


**Figure 4.6:** (a) Loading scenario for the non-rotated geometry and (b) rotated geometry. (c) The absolute difference in magnitude between the unit Poisson's values resulting from (a) and (b).

## 4.5 Physical testing simulations

For physical testing purposes, a rectangular bar is added to the upper and lower part of the design. It is assumed that the additional part consists the same material properties as the auxetic design itself. The main motivation for this addition is:

- (i) Research which executes similar compression tests blame their measurement errors to boundary effects [4, 37]. Within these tests, the design is just placed between the press and the platform without additional clamping between the design and the testing interface. For such a clamped boundary, the numerical outcome can be predicted on forehand and compared with the experimental outcome, using same test conditions.
- (ii) Frictional effects, like stick-slip might be present by releasing horizontal displacements at the lower part of the design.

Before the physical experiment starts, a numerical experiment is executed to investigate whether an adjacent bar to the design restricts the auxetic behavior. Therefore, a similar study is performed as in Section 4.4 using boundary conditions as in Figure 4.7; which represents loading scenario C. The horizontal displacements of the upper part are constrained to mimic physical test conditions. In physical testing circumstances frictional forces between the top of the design and the head of the press are present, which constrain the motion at that position. A static frictional force is present between the two surfaces and therefore there is chosen to use this type of boundary condition.

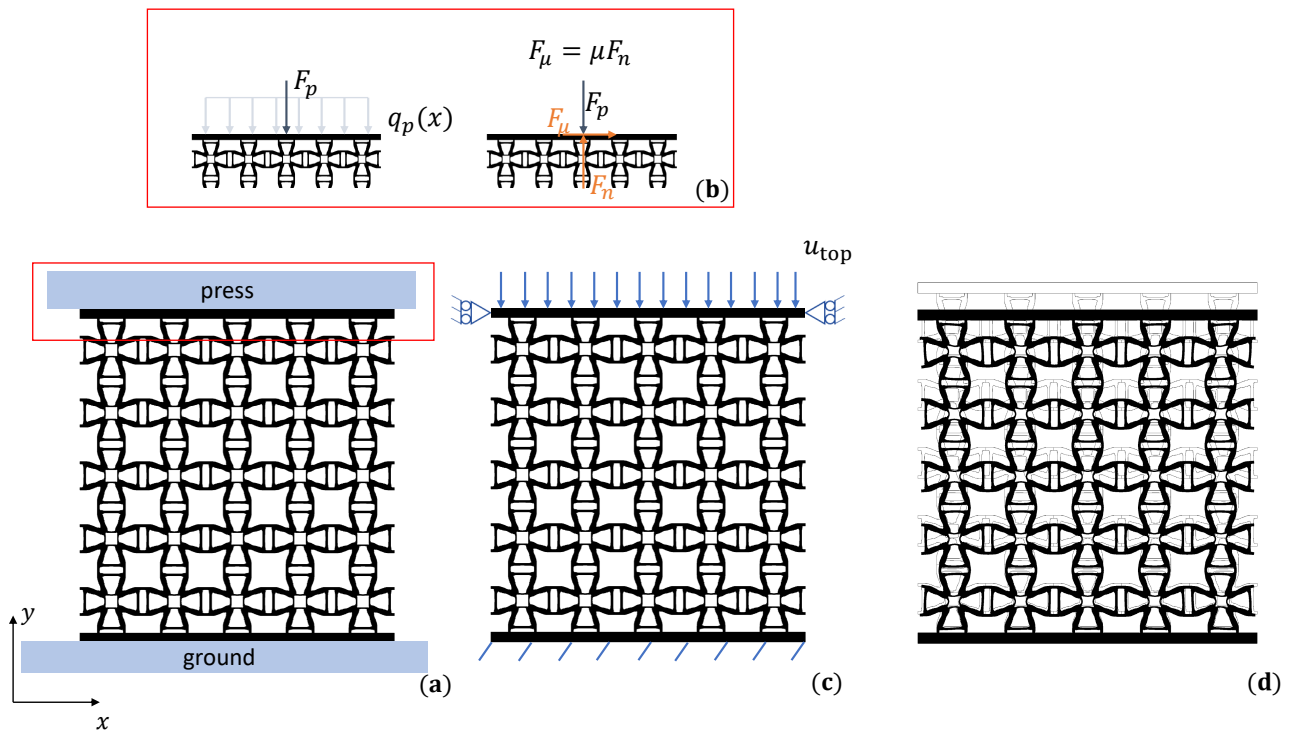


**Figure 4.7:** Loading scenario C. The test setup in schematics (a) is modeled with boundary conditions as in (c). The motivation for this type of loading is shown in (b): the press exerts a distributed load  $q_p(x)$  with a resultant force  $F_p$ . The normal force  $F_n$  is equal to the resultant force and a static frictional force  $F_\mu$  constrains horizontal displacements at the upper region.  $F_p$  will never overcome by external forces in x-direction (they are except friction negligible) and the upper part will remain in horizontal position. The deformed configuration is shown in (d).

### 4.5.1 Observations for varying boundary conditions

Loading scenario C is compared with the earlier obtained results for scenario A and B and is shown in Figure 4.8. The contour plot clearly shows the effect of the boundary conditions: for a fixed bottom part of the design Poisson's values significantly differs from the homogenized value at the most outer unit cells. Moreover, the numerical analysis shows that the bars connected to the design (scenario C) do have an influence on the auxetic behavior of unit cells close to these bars. Fortunately, these bars do barely limit the auxetic behavior in the most central cell: the green color of this cell indicates

that significantly differences with respect to the homogenized value are not present. Thus, adjacent bars hardly influence the auxetic behavior, evaluated at the most central part of the design. Therefore, it is chosen to manufacture a rectangular bar adjacent to the top and bottom unit cells of the design for physical testing.

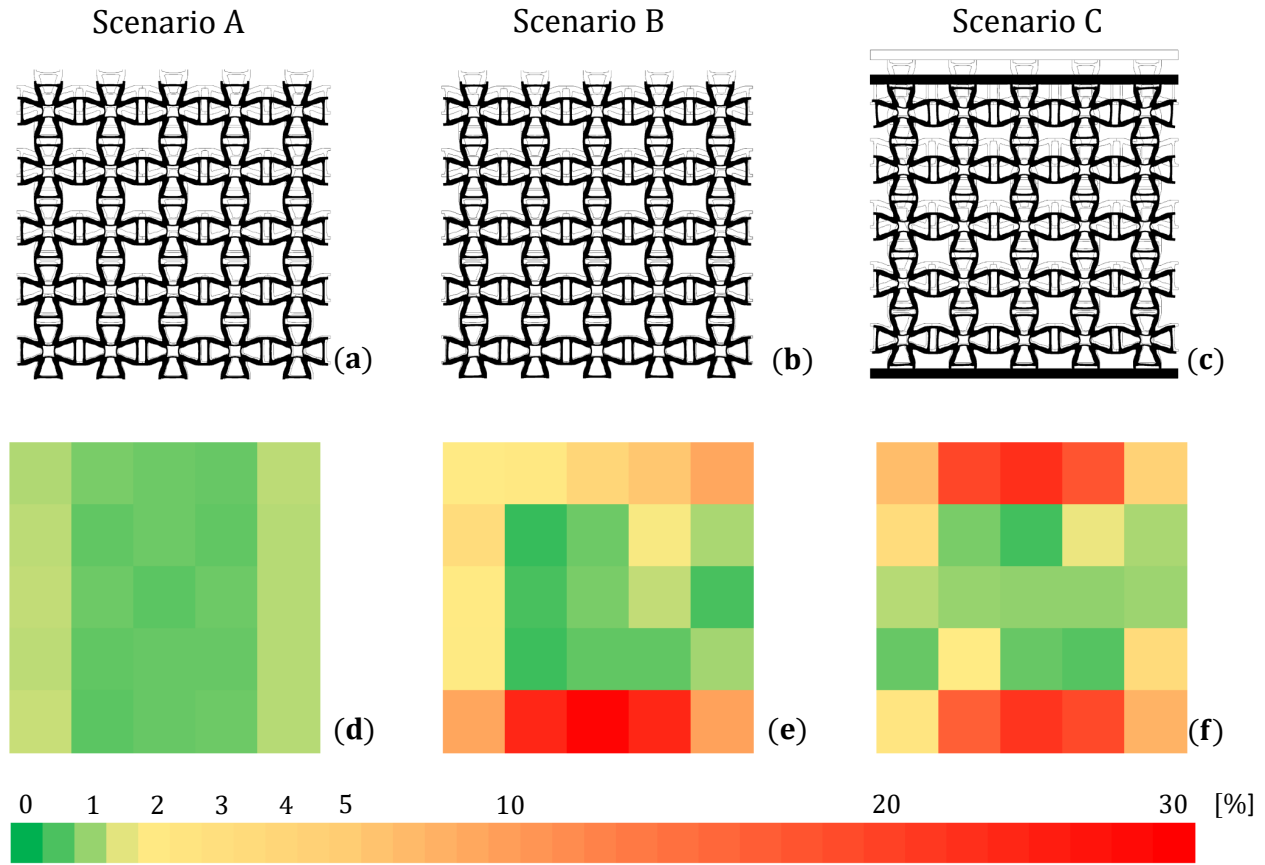


**Figure 4.8:** Deformed configurations (a-c) and Poisson’s values differences in % with respect to the homogenized value (d-f) for system size  $n=5$ . The Poisson’s ratio for each cell individually is calculated from Equation (4.10).

### 4.5.2 Compression test modeling with fixed boundaries

To predict the physical test outcome, the geometries of the 3D printed designs are simulated using finite element software. A 2D analysis, using plane-stress conditions (assuming negligible stress-variations out of plane), is performed with boundary conditions as in Figure 4.7. Geometrical non-linearities are taken into account to obtain deformed configurations for finite strains. Designs are compressed until 4% uniaxial strain  $\epsilon_u$  and gravity loads are neglected. The Poisson’s values are evaluated from the displacements of the most central frame and are plotted as function of the uniaxial strain (Equation (4.1)). Relevant observations are as follows:

- The red and blue geometries are stable in terms of Poisson’s values magnitudes with respect to the applied uniaxial strain. When the uniaxial strain increases, auxetic designs which exhibiting a more negative Poisson’s value are unstable with respect to the homogenized Poisson’s value. Nevertheless, auxetic behavior is preserved, since the magnitude of Poisson’s values remains negative.
- For small strains ( $\epsilon_u \leq 1\%$ ) the results (Figure 4.10) are consistent with the homogenized values of the unit cells. Outside this regime, the geometrically non-linear effects play a dominant role and Poisson’s value diverge from the target value. This type of non-linearity is not incorporated in the optimization scheme, which supports the deviation of the numerical response compared to the homogenized value for finite strains.
- For increasing strains, the response of the red geometry shows a closer match with the homogenized value in terms Poisson’s value. This is in contrast with other designs, where Poisson’s values more deviates from the target value for

increasing strains.

- The kink in the response curve for the chiral geometry (in green) is a result of in-plane buckling of the structure. This phenomena only occurs while performing a geometrically non-linear study and cannot be observed for a geometrically linear analysis. For a linear analysis, the equilibrium equations are formulated in the undeformed state and are not updated with the deformation. This result in a linear force-displacement response with a constant slope (the stiffness). Consequently, a change in the slope and therewith a change in stability (which refers to buckling) might not happen. Also, buckling was observed in the physical test, so possible causes for buckling of this geometry are discussed in an experimental section of this thesis, Section 5.4.4.

In literature, a similar experiment has been founded for the structure in black [20]. They noticed a steep decrease of the Poisson's ratio for small uniaxial strains, followed by a slow decrease with an almost stabilization. Therefore, higher magnitudes of uniaxial strains are applied for this particular design to check whether this trend occurs. Figure 4.9 shows that still the absolute Poisson's value slightly increases for uniaxial strains above 4%. This trend curve is in line with the mentioned literature. From this literature source, it can be concluded that the experiment seems representative executed. Moreover, the preservation of a negative Poisson's value for this particular geometry is promising for auxetic behavior for large uniaxial strains.

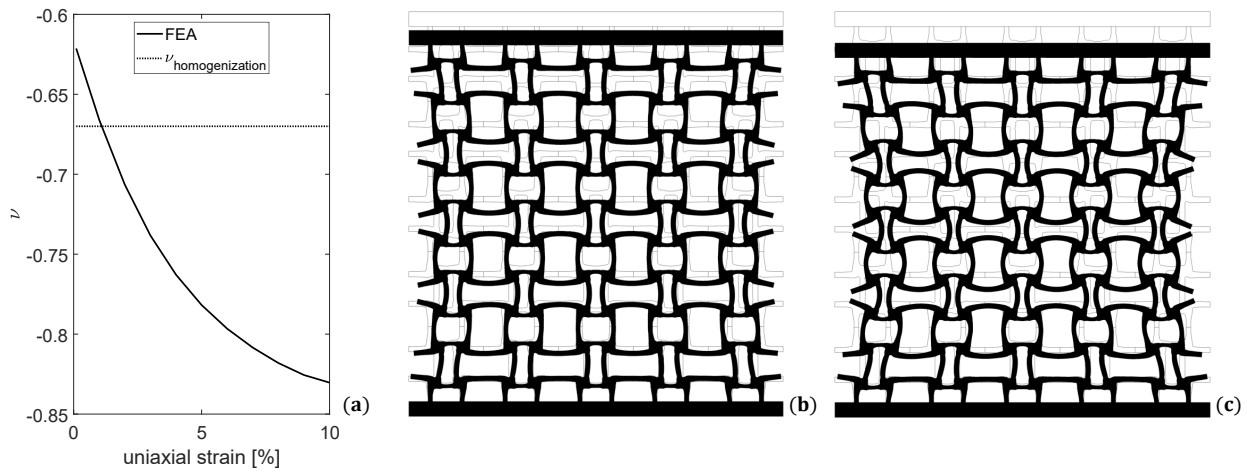


**Figure 4.9:** Auxetic behavior for large strains. (a) The numerically obtained Poisson's value for large uniaxial strains and compressed configurations at (b) 5% and (c) 10% uniaxial strain, respectively.

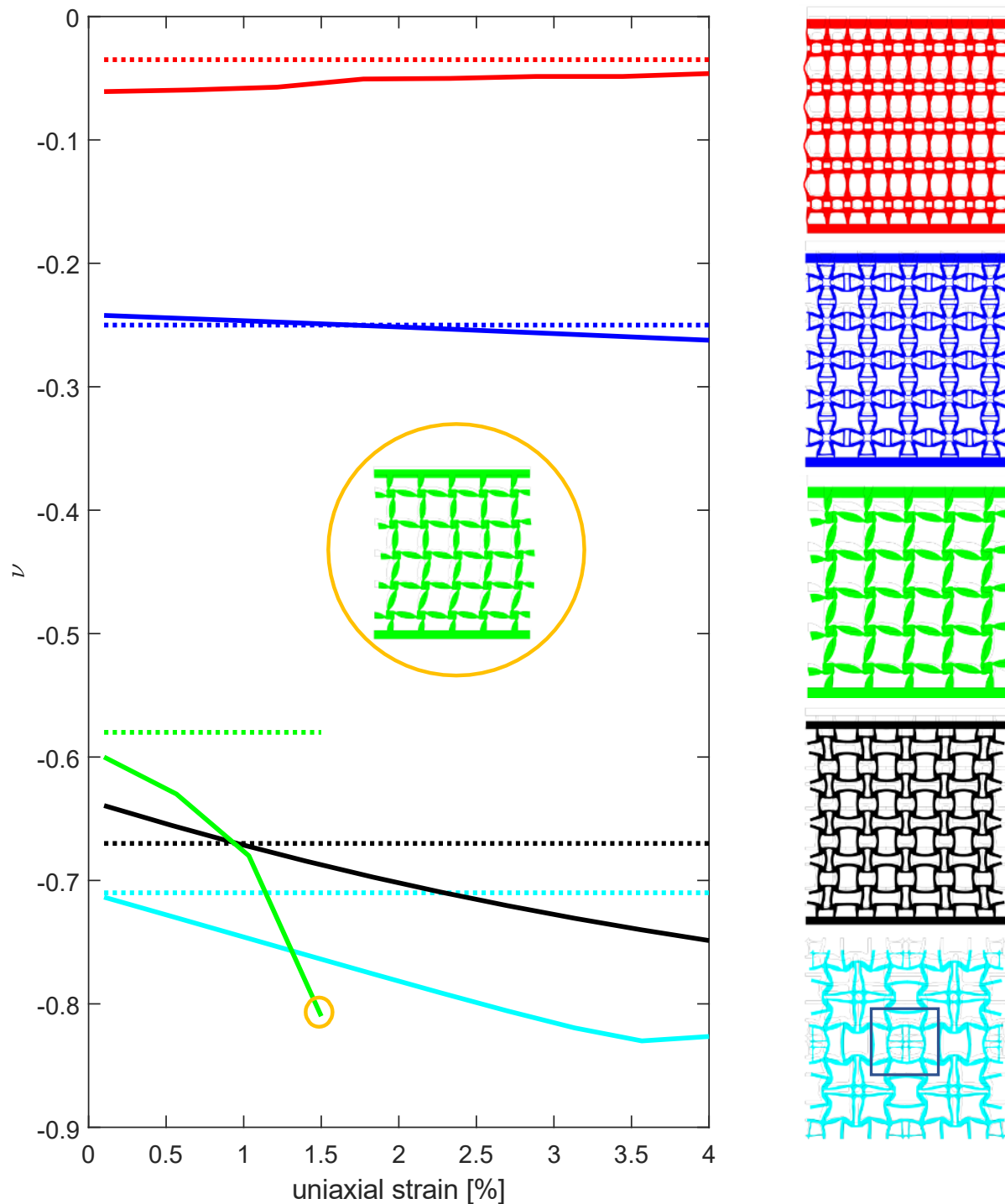


**Figure 4.10:** Numerically obtained Poisson's values as function of the uniaxial strain (solid curves) on the left. Poisson's values are tracked from the most central frame; for the geometry in light blue the Poisson's values are tracked from the solid frame (dark blue). The horizontally dashed lines represent the homogenized value. Colorized deformed configurations are taken for a uniaxial strain of 2% (except the green geometry) and the color of the geometry is linked to the color of the curves. The encircled green geometry represents the buckled configuration at 1.5% uniaxial strain.

## 4.6 Conclusions

The conclusions of this section are given by answering the research questions (RQ) as proposed in the introduction.

**RQ 1.** *Does a Poisson's ratio measured by elastic energy terms results in equivalent values compared to a Poisson's measure based on strains?*

Yes. For a numerical test on a square unit cell, both methods result in equivalent values. For an auxetic unit cell, both methods are quite consistent. However, a difference in terms of Poisson's values of 6% between the result of the strain method and the homogenized value came out.

**RQ 2.** *Does the system size influences the auxetic behavior throughout the design?*

For a zero friction boundary at the bottom (scenario A): no. An almost constant Poisson's value is found at the most central cells. A maximal difference of 2% with respect to the target value has been observed.

For a maximum (fixed) boundary at the bottom (scenario B): yes. The clamped boundaries become more dominant for increasing system sizes, since auxetic behavior is constrained close to the fixed regions. Probably, more unit cells in a design do give more stiffer unit cells at the bottom, since they are highly constrained by the fixed boundaries. The Poisson's value of the most central unit cell remains almost constant for increasing system sizes.

**RQ 3.** *Does the type of applied boundary conditions influence the auxetic behavior throughout the design?*

For a maximum friction (fixed) boundary at the bottom and a horizontal constraint boundary at the top (scenario C), Poisson's values differ at that position with respect to the target value. Compared to scenario A and B, the boundary conditions of this scenario strongly limit auxetic behavior. Typical values in terms of Poisson's values difference for a design with system size  $n = 5$  are 0.9 %, 5.2 % and 6.3% for scenario A, B and C, respectively. For scenario B, the auxetic behavior is mainly limited at the lower section of the design. Fortunately, the most central unit cell is almost equal for all three loading scenario's and therefore fabricated designs are experimental tested under loading conditions as in scenario C. This study also shows that for scenario B and C, asymmetric auxetic behavior comes in: Poisson's values at the most left column are not identical to those at the most right column. A follow-up numerical investigation shows that the geometry of the tested auxetic design is not symmetric: the auxetic behavior is dependent on the orientation of the geometry.

# Chapter 5

## Physical experiments

The main goal of this section is to validate the auxetic behavior of a patch of unit cells by means of physical experiments. So far, auxetic behavior of optimized unit cells has been analysed numerically. Even more interestingly, is the behavior of such structures in practice. As motivated in the introduction, the knowledge gap of validating auxetic designs mostly is in the experimental area. Therefore, the manufacturing possibilities are discussed (Section 5.1) to fabricate auxetic designs. Based on an AM technique, relevant mechanical behavior of fabricated specimens is tested (Section 5.2) and demonstrated on a benchmark mechanism in Section 5.3. Further on, the auxetic designs are experimentally tested (Section 5.4), with testing conditions as derived from numerical modeling studies. Also, the AM discoveries are used to motivate choices for experimental testing.

### 5.1 Additive Manufacturing

AM techniques are advantageous for fabricating designs composed of unit cells. Namely, the layout obtained from the TO process is often complex and AM can easily fabricate such designs. The idea behind AM is that an initially generated model, using 3D Computer-aided design (CAD), can be fabricated without the need for process planning. AM significantly simplifies the process of producing complex 2D or 3D structures. Whereas other manufacturing processes require a careful and detailed analysis of the order of fabrication, choice of tools and processes, requires AM no process planning. Several printing techniques exist and in this project it is chosen to fabricate designs using a Fused Deposition Modeling (FDM) technique, because of the following:

1. The user-friendly of fabrication auxetic designs with the FDM technique is definitely an advantage. Since the author wants to make the designs by himself (and not to outsource the process), it is helpful that one can be quickly familiarized with this technique.
2. Previous work focuses on the fabrication by making use of Selective Laser Sintering (SLS) or Sterolithography (SLA) techniques [4, 36, 37]. Fabricating auxetic designs using FDM is quite unexplored.

A more in-depth overview of available AM techniques and their pros and cons is given by Wang *et. al* [39].

#### 5.1.1 FDM

The fabrication process using FDM is visualized in Figure 5.1. A movable platform is continuously positioned to ensure the desired geometry is printed (1). If the platform is aligned properly, a plastic filament (2) is fed through rollers (3) pushing the thread through a heated nozzle (4). At the nozzle, the wire is heated and ejected from the nozzle at a constant speed. After each printed layer, the platform is lowered and the next layer is deposited. Optionally, support structures (5) are printed to allow overhangs.

This process is quite cheap and user-friendly, but brings the challenge that the printed geometry is composed of multiple layers, in which each layer consist of adjacent wires. During printing, the sequence and pattern of these wires is uncontrolled for the user and already brings in inhomogeneities and therewith anisotropy into the material. A possible solution of this challenge is described in Section 5.1.3. Moreover, the anisotropic nature of 3D printed parts using FDM is experimentally investigated in Section 5.1.2.

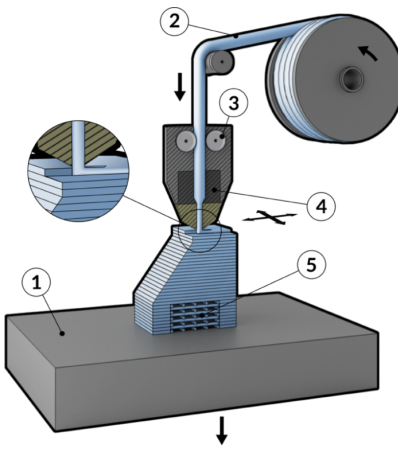


**Figure 5.1:** The fused deposit modeling technique [21].

### 5.1.2 Manufacturing of designs using FDM

To fabricate the auxetic designs a filament is chosen such that the following requirements are satisfied:

- (i) The filament must be compliant, such that the fabricated designs deform under a compressive load.
- (ii) The filament must be both bendable and flexible.

Based on these requirements and expert opinion, a flexible type of filament (FLEX65) has been chosen, with a typical Young's modulus of 95 MPa [1]. Fabricated designs are composed of 5 by 5 unit cells<sup>1</sup>, for practical reasons. The main limitation is the build area of the 3D printer: designs with more unit cells do not fit on the buildplate. However, an increase of the amount of patterned unit cells in an auxetic design results in an increase of manufacturing costs and designs become sensitive for out-of-plane buckling. Designs are manufactured by extruding the geometry with a certain thickness; overall dimensions are listed in Table 5.1. Based on empirical finding extruded thicknesses are estimated to avoid out-of plane buckling. Fabricated designs are shown in Figure 5.2 with labeling numbers according to designs listed in Section 3.5. The main observed printing error is the out-of-plane warping of the fabricated sample as illustrated in the left figure of Table 5.1. Due to material shrinkage while 3D printing, the corners of the material lift up and detach from the build plate. An attempt is made to tackle this phenomena using best practices of experts, but still some warping remains. The reader must be aware that the amount of parameter settings is enormous and time constraints do not allow to obtain the optimal settings to fabricate designs using this filament.

|   | ID    | $L^a$ [mm] | $L^d$ [mm] | $t^a$ [mm] | $t^d$ [mm] |
|---|-------|------------|------------|------------|------------|
|   | 1.1   | 94.35      | 94.50      | 9.56       | 9.50       |
|   | 1.2   | 55.05      | 55.00      | 7.02       | 7.00       |
|   | 2     | 103.96     | 104.00     | 9.95       | 10         |
|   | 3     | 73.44      | 73.50      | 6.06       | 6          |
|   | 4     | 133.01     | 133.00     | 9.94       | 10         |
| 5 | 78.70 | 79.00      | 6.51*      | 6.5        |            |

**Table 5.1:** Dimensions of the as-printed designs ( $L^a$  and  $t^a$ ) and the designed dimensions ( $L^d$  and  $t^d$ ).

\*The as-printed thickness has been taken at the thickest part of the design, as pointed in red in the figure on the left.

<sup>1</sup>Design 1.1 and 1.2 are composed of 2 by 2 unit cells, because the numerical study towards system size effects was not performed at that moment. However, the experimental outcome results in valuable practices for experimental testing.

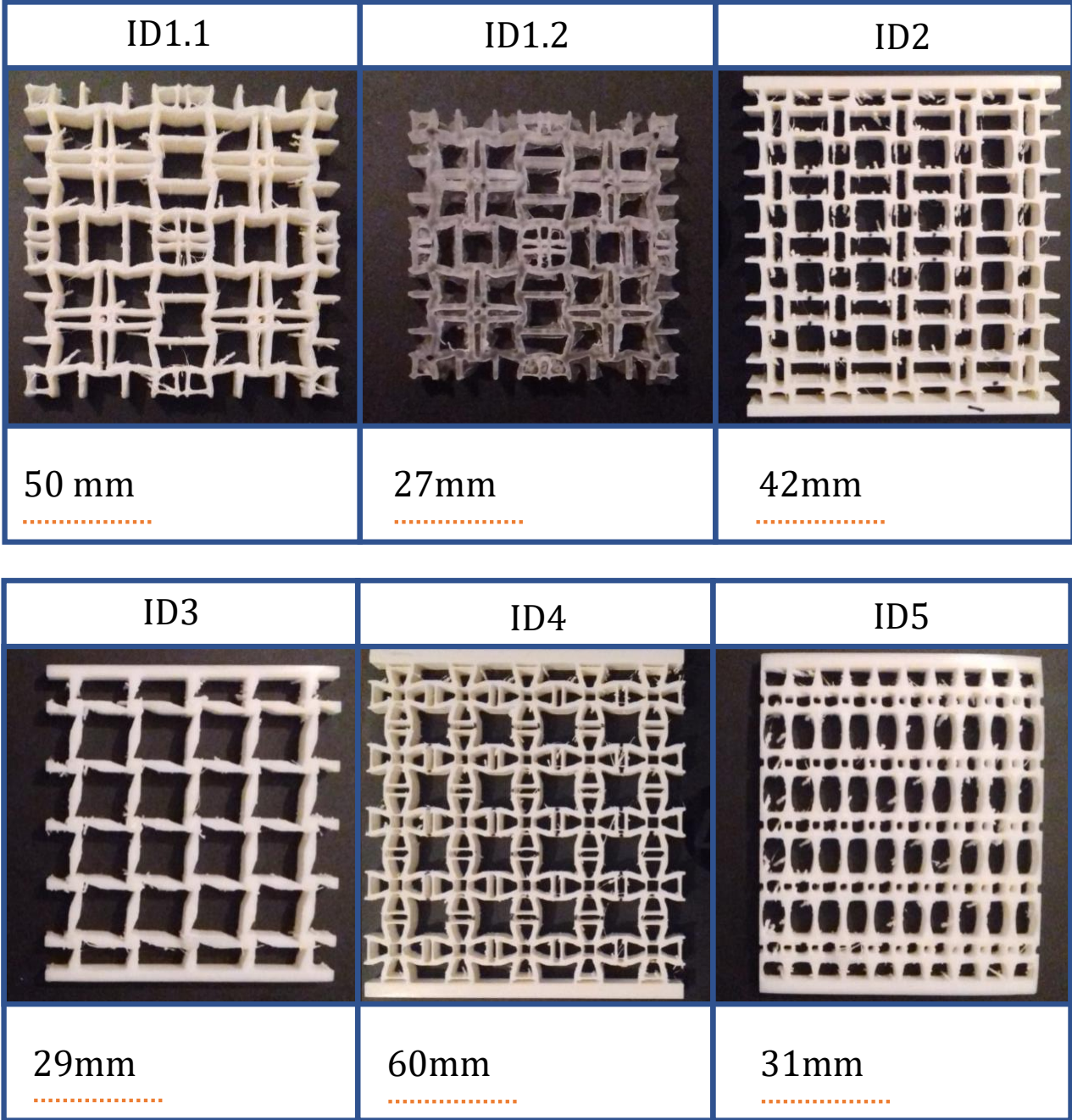


**Figure 5.2:** Fabricated designs using 3D printing. Design 1.2 has the same geometry as design 1.1, but is made out of Polydimethylsiloxane (PDMS). The fabrication process for design 1.2 is reported in the next section.

### 5.1.3 Manufacturing of designs using a mold of FDM

A fabrication method is proposed to get rid of layering into the material. The printed layers might give inhomogeneities into the material and bring unwanted effects as explored in Section 5.2. The fabrication method is executed for unit cell with ID1. By making a mold of the 3D printed design, this mold is filled with a certain polymer, PDMS. Instead of manufacturing the optimized layout, the surrounding material is fabricated. This ‘inverse’ way of prototyping auxetic designs is quite innovative and reported once before [7]. The fabrication method is shown in Figure 5.3 and choices are made based on expert opinion. The executed fabrication process takes a lot of time, since the PDMS sample is (i) cured at room temperature and (ii) the mold is dissolved. However, the process can be speed up to cure the (initially liquid) PDMS in a hotter environment, like an oven. Also, the sample can be peeled of the mold without solving the mold itself, however some tiny parts of the structure might be damaged using such a strategy.

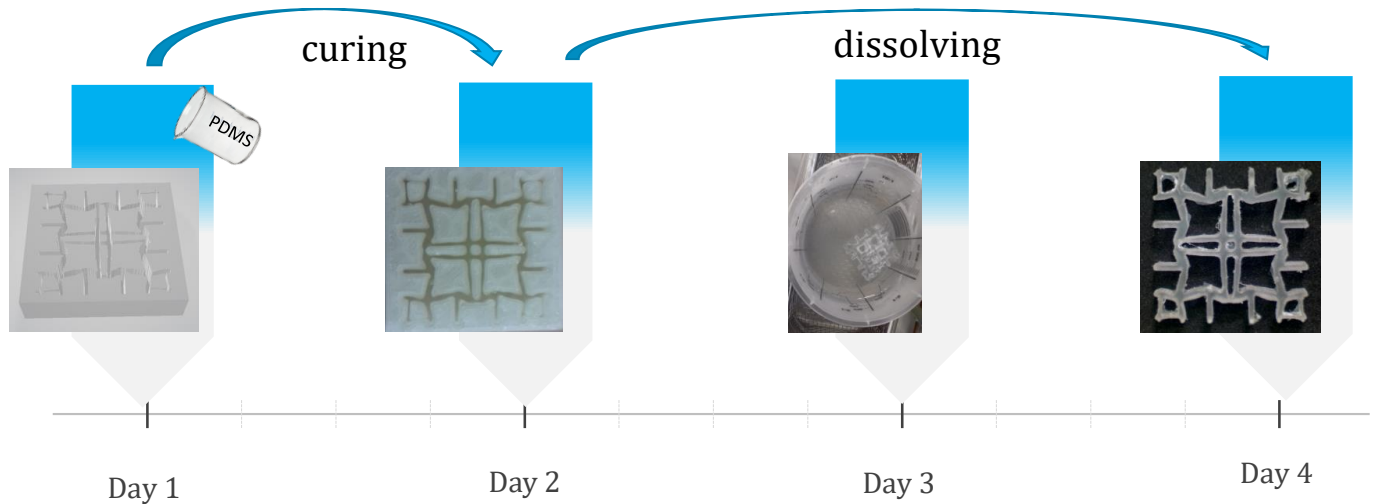


**Figure 5.3:** Time line for the fabrication process of an auxetic unit cell made out PDMS. Firstly, a negative of the design is fabricated using a dissolvable filament Butenediol Vinyl Alcohol Co-polymer (BVOH). Next, a PDMS mixture is created with a curing agent to elastomer ratio of 1:10. The mold is filled with the mixture and cured for approximately 2 days. Finally, the sample is pulled out the mold by dissolving the mold in water. Initially, this process is performed for a unit cell to familiarize with the process. Similarly, a design composed of 2 by 2 unit cells was fabricated.

Note: despite best practices some of the support material remains in the narrow regions. This might influence the experimental outcome for this sample.

## 5.2 Notch flexures testing

In fact, a mechanical metamaterial is a compliant mechanism. Such mechanisms are flexible and transfer an input force/displacement ( $u_{in}$ ) at one or multiple ports to an output force/displacement ( $u_{out}$ ) at one or multiple output ports through elastic behavior of the structure. Some compliant benchmark mechanisms and an auxetic unit cell are shown in Figure 5.4. The elastic body

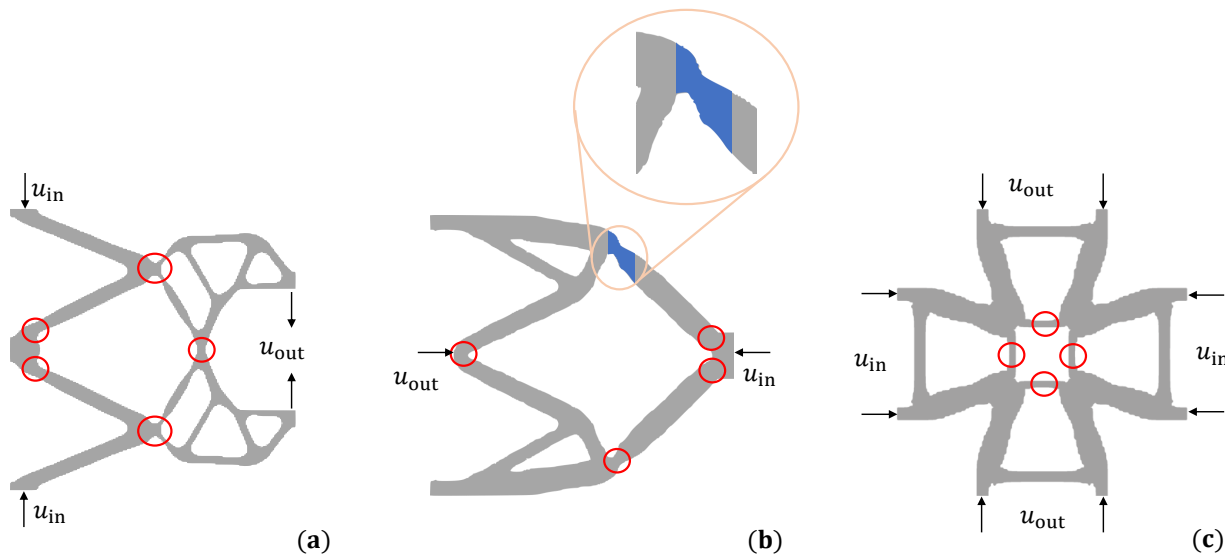


**Figure 5.4:** Benchmark compliant mechanisms (a-b) designed by topology optimization. Both the inverter (a) and gripper (b) obtain their transformation from an input to an output by the compliant hinges (encircled parts). The auxetic unit cell (c) deforms by bending of the slender ligaments.

deformation is mainly obtained by bending of the encircled parts of the mechanism. The position and orientation of such slender parts in a mechanism will ensure that the structure deforms in a certain manner. Ideally, a mechanism is composed of homogeneous material with equal material properties throughout the whole structure. However, mechanisms fabricated with FDM techniques are composed of multiple layers which could lead to anisotropy and inhomogeneities in the material. Moreover, printing uncertainties of the filament can give material deposition at unwanted locations. This may affect the stiffness locally and also the output displacement. It is unclear whether fabricated mechanisms printed under an angle with respect to the build plate, still obtain their desired displacement behavior. This research field is quite unexplored; only a study is performed [6] in which polylactic acid (PLA) material properties are investigated under varying printing conditions. Therefore, an experiment is performed, where the stiffness of 3D printed notch flexures is evaluated for fabricated specimens. Such a flexure consists of a thin cut-out of both sides of a thick piece of material as in Figure 5.5(a). Since designs as in Figure 5.4 are also composed of hinge kind of flexures it is chosen to test this flexure. The method is as follows: several samples are printed with varying angles with respect to the print plate. The geometry is kept equal for varying orientations and discussed in the design procedure. Next, the experimental procedure is described, results based on these experiments are discussed and further prospects are outlined.

### 5.2.1 Design procedure

A notch hinge with dimensions according Figure 5.5(a) is designed, with an elastic hinge parameter ( $t/2 \cdot r$ ) between 0.01 and 0.5. Designs with values below 0.01 do not allow for manufacturability and values above 0.5 lose their functionality [10]. 10 notch flexures are 3D printed using flexible filament under varying angles with respect to the baseplate; Figure 5.5(b). The fabricated results are showed in Figure 5.5(d) and a detailed drawing of the notch flexure are attached in Appendix D.

## 5.2.2 Experimental procedure

To evaluate the stiffness of each of the samples a 3-point bending test is executed, as shown in Figure 5.5(c). To allow a proper bending of the specimens, displacements are constrained with point impositions at the bottom. The vertical displacement of the hinge is obtained by a press which gradually applies displacements downwards, halfway the length of the sample. A maximal displacement of 2mm, with load steps of 0.05mm/s, is applied to stay in the linear elastic regime. The press goes up and down 5 times for each sample, without re-positioning the sample. From the obtained force-deflection curves (Figure D.2 from Appendix D) the stiffness is extracted with a linear fit between the data points.

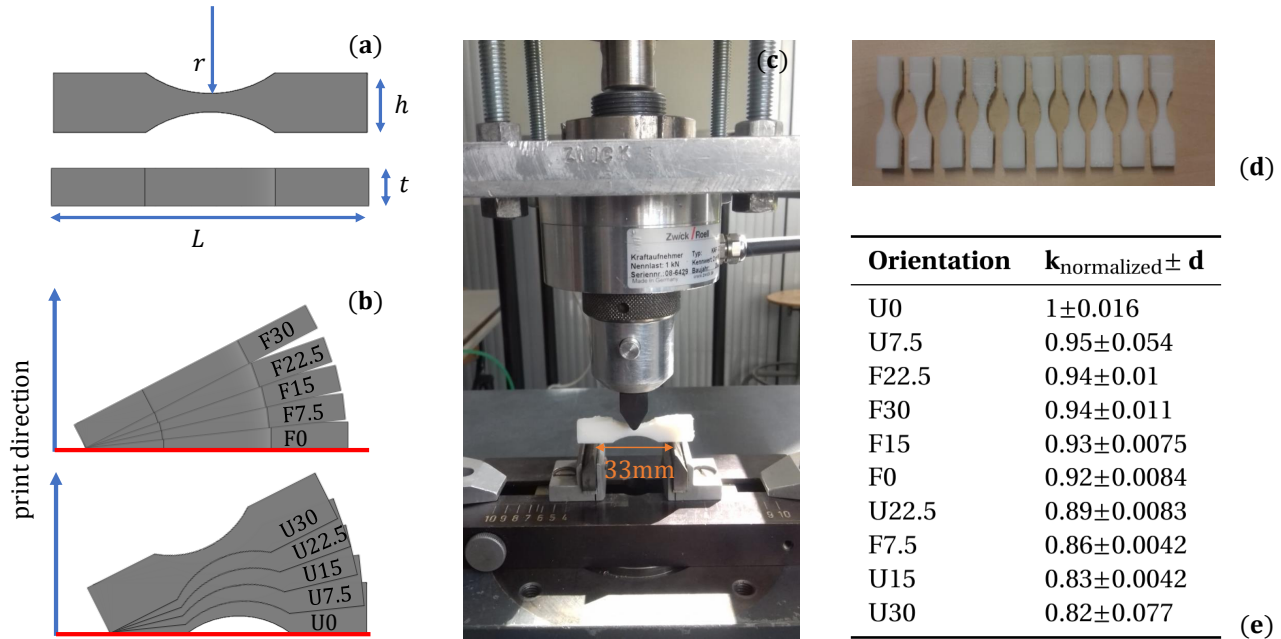


**Figure 5.5:** (a) The design parameters of a notch flexure. (b) The print orientation of the specimen with respect to the print plate (red line). The letter 'F' and 'U' indicates the position of the specimen, which can be flat (F) or upright (U). The number defines the angle between the plate and the sample. (c) The fabricated notch flexures. (d) The experimental setup and (e) The normalized stiffnesses for each orientation. Standard deviations 'd' are obtained by repeating the experiment for each sample five times.

## 5.2.3 Notch flexure stiffness results

The stiffnesses are normalized with the most stiff configuration and are listed in Figure 5.5(e). Since thickness variations are present between the fabricated samples, the stiffness is corrected for geometrical deviations.<sup>2</sup> Finally, a stiffness difference of 18% between the most and less stiff configuration is observed. There seems no relation between the print orientation and the observed stiffness. Nevertheless, the highest value in stiffness of orientation U0 seems logical. According to the test frame, printed layers are stacked along the loading direction. As a consequence, a laminated kind of design exists which is beneficial in terms of bending stiffness. The huge spread is cause for a concern in the field of printing mechanisms in 3D with deposition modeling techniques. This spread still remains unexpected, nevertheless a similar research to PLA samples also shows a maximum of 15% stiffness difference [6]. This study explores the field of additive manufacturing of compliant hinges and the outcome gives a motivation to show this build plate effect on a benchmark mechanism.

<sup>2</sup>The stiffness of a notch hinge goes as follows:  $k \sim t^3 \cdot \left(\frac{h}{2r}\right)^{0.5}$  [10]. Since  $t$  is of the highest order and therefore the most dominant term in determining the stiffness, corrections are made for the thickness. After printing, the geometry of the specimens is measured using a caliper and the scaling is applied.

### 5.3 Benchmark design testing

Notch hinges, fabricated in different printing orientations, shows a spread of 18% in stiffness due to inhomogeneities in the material. This outcome gives a motivation to print the compliant inverter, a benchmark mechanism in the field of designing compliant mechanisms using TO. Moreover, this study will evaluate whether 3D printing techniques like FDM are suitable for fabricating auxetic designs in 3D. Thus, the goal for this section is to evaluate and investigate by an experiment the influence of the print orientation on the output trajectory for a given input displacement.

A benchmark compliant mechanism, the inverter, is generated utilizing the 99-lines of code in MATLAB [31]. The boundary conditions for this design problem and the optimal density distribution after using a B-spline fit (as in Section 4.2) are presented in Figure 5.6. Further optimization and design aspects are explained in Appendix E.

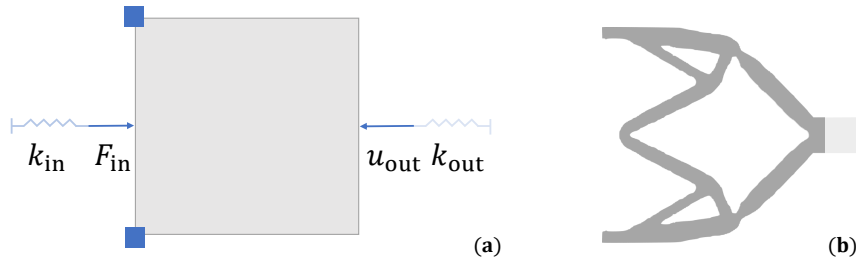


**Figure 5.6:** (a) The design problem with boundary conditions at the input and output ports for optimizing an inverter mechanism;  $k_{in} = 0.1$ ,  $k_{out} = 0.1$  and  $f_{in} = 1$ . The objective function is defined such that  $u_{out}$  is maximized. (b) The 2D geometry of the compliant inverter after a B-spline fit. The light gray area is added to the original geometry (dark gray) for testing purposes.

#### 5.3.1 Mechanism fabrication

A 3D structure is created by extruding the 2D geometry such that mechanisms can be fabricated. Designs are positioned at the baseplate as in Figure 5.7 with the following orientations:

- Orientation F0: the most trivial orientation. The inverter is 3D printed flat on the baseplate without any layer wise variation in z-direction.
- Orientation F30: the inverter is rotated over an angle of 30 degrees along the y-axis. Test results from previous section shows that this print orientation significantly differs in terms of stiffness with respect to other orientations.
- Orientation U0: the inverter is rotated 90 degree around the x-axis

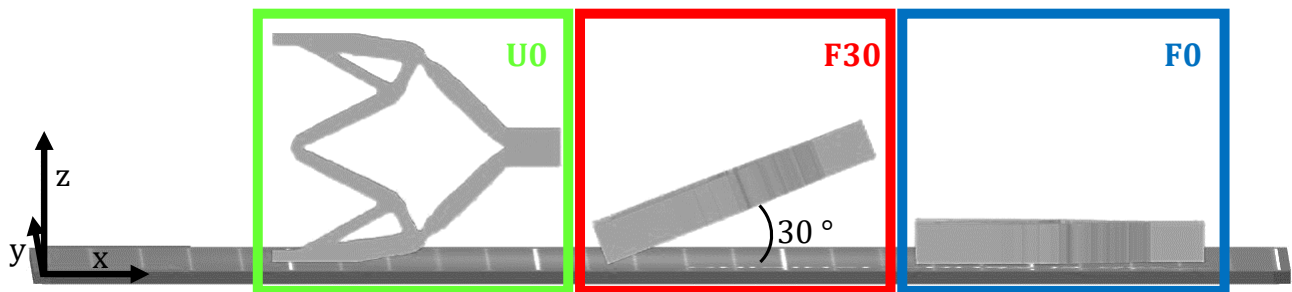


**Figure 5.7:** Orientations of inverters with respect to the print plate.

It is observed that the fabricated samples positioned under an angle exhibit a rough surface. Because of the layering of the stacked layers such an effect occurs. Moreover, the removal of support material affects the design and to some extent the performance. These observations are noted to address on beforehand orientation F30 and U0 might not perform as expected.

### 5.3.2 Experimental procedure

Fabricated parts are experimentally tested on their output trajectory, while performing an compression test as in Figure 5.8. The inverter is actuated vertically at the top with a velocity of 0.01mm/s until a displacement of 2mm. The most upper part

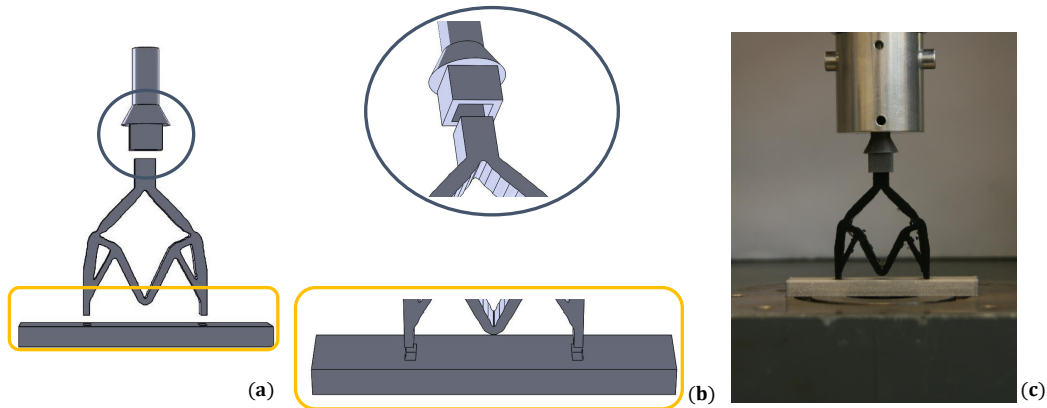


**Figure 5.8:** The experimental setup in schematics (a-b) and in practice (c). At the top of the mechanism (blue box) a connector is inserted, which consist of a circular part such that it fits in the head of the press. The bottom of the mechanism (orange box) is inserted in rectangular plate with slots.

of the mechanism is guided by a shape fitted connector, which is inserted in the press. In this way, a straight input trajectory is ensured. The most lower part is placed into a fixed plate to mimic to boundary conditions as defined in the optimization. During physical testing, the region as shown in Figure 5.9(a) is recorded by taking photographs for each load step. A similar strategy is used for evaluating Poisson's ratios from an auxetic design and explained in depth in the upcoming section. The in-plane x- and z- coordinates of that region are evaluated for each load step. From there on, displacements are defined by taking displacement differences between the current and previous load step. These displacements result in an output trajectory. For each design, above mentioned experimental procedure is performed three times one the same specimen. In between each recurrence of the experiment, the specimen is not removed or replaced from the setup.

### 5.3.3 Compliant mechanism testing results

Figure 5.9(b) shows the paths of all three designs: the dashed line represents the desired output path and the transparent curve denotes the error band as found by repeated testing. It becomes clear, the print orientation of the 3D printed design highly influences the trajectory of the mechanism. Orientation F0 shows hardly any deviations in x-direction, whereas orientations F30 and U0 tend to diverge from the desired output path. Main deviations are probably caused by the stacking and orientation of the 3D printed layers at the hinges. Probably, due to the infill at and around the hinges this mechanisms shows undesired behavior. Orientation U0 and F30 consist of hinges in several orientations. Previous testing of notch flexures shows already variations in stiffnesses for printing under an angle, which was also demonstrated in this experiment. The variance in stiffness will lead to a difference in displacements at that point. As a result, it is likely the mechanism as a whole gives unwanted displacements. Fabricated designs further on in this project are printed using orientation F0. The choice for this orientation is trivial and performs the best.

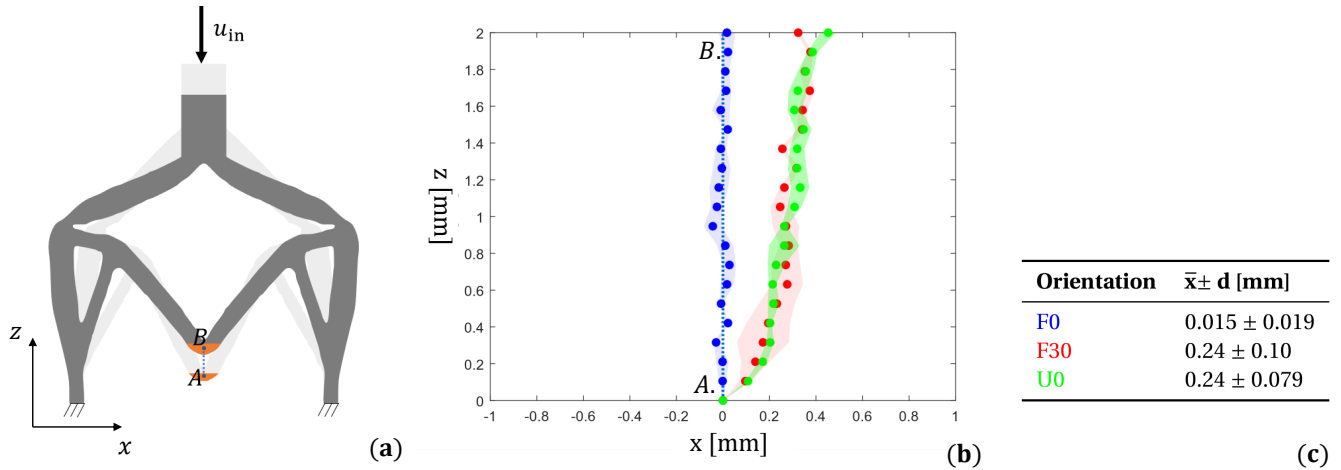


**Figure 5.9:** (b) Output trajectory for inverters for an actuated displacement  $u_{in}$  pointing downwards (a). The blue, red, green samples represents orientation U0, U30 and F30, respectively. The error band (transparent) represents the difference between the minimal and maximal mechanism displacement in x-direction. (c) The average output displacements in x-directions and their deviations.

## 5.4 Auxetic structures testing

This section describes the experimental setup for auxetic designs testing in Section 5.4.1. The strategy to extract Poisson's values from a compressed configuration is explained in Section 5.4.2 and experimentally obtained Poisson's values are reported Section 5.4.3. Finally, relevant findings are reported about non-auxetic response, the measuring location and clamping aspects of an auxetic design in Section 5.4.4, Section 5.4.5 and Section 5.4.6, respectively.

### 5.4.1 Experimental procedure

To obtain deformations of the design, a compression test is executed using a draw bench of the type Zwick/Roell Z005. The experimental procedure as described in this section is used for all experiments. As already stated, the sample is located between the ground and the press as shown in Figure 5.10. A rigid plate is connected to the press to create a surface between the press and the fabricated sample. The plate is wrapped with blue 3M Scotch tape, which exhibits sufficient roughness to hold the top part of the sample in position.

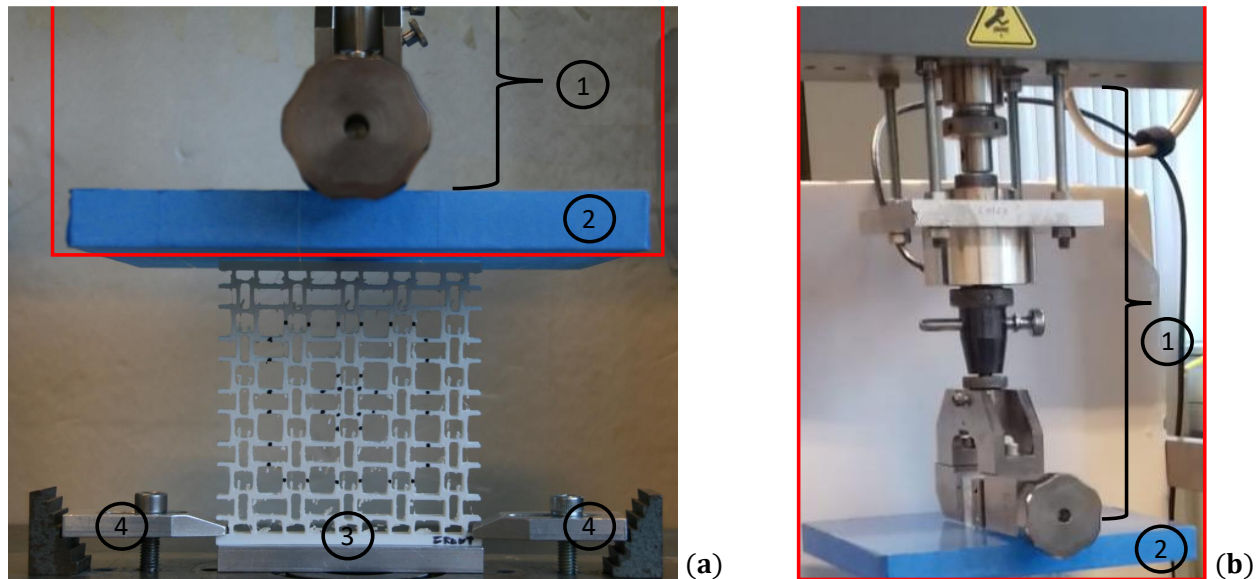


**Figure 5.10:** (a) Experimental setup for auxetic designs compression with a zoomed image (b) of the press. This figure shows the undeformed configuration of the auxetic design. (1) Represents the press, (2) the rigid (blue) plate, (3) the adjacent bar fabricated at top and bottom of the auxetic design and (4) the frog clamps.

The press is actuated by displacements and moves gradually downwards with a velocity of 0.1mm/s. To assure a full contact between both surfaces, a pre-stress is used before starting the measurement. The challenge is to apply a displacement such that geometrical (and material) non-linear effects do not play a dominant role. For exceeding small strains geometrical non-linear effects already arises (as discussed in previous chapter). However, literature suggests to apply finite strains to obtain a platform of constant Poisson's value as a function of applied displacements [37]. During the first loading steps, the sample is not fully settled between the sample and the press and finite strains are needed. Therefore, a uniaxial strain of 4% is applied for all designs and the author is aware of possible deviations for finite strains.

### 5.4.2 Image processing

Before the experiment starts, black dots or lines are marked on the surface of the sample (their influence is discussed in Section 5.4.5). During compression of the structure, photographs of the deformed configurations are made with a camera: Canon EOS 400D. A succession of photographs are obtained by continuously shooting with a frame speed of 3 frames per second. Based on these shots, image processing is performed and the positions of these marked regions are extracted as visualized in Figure 5.11. Poisson's ratio are calculated from the averaged displacements in transverse (x-direction) and longitudinal (y-direction) direction. From the frame in Figure 5.11 the Poisson's ratio is calculated as a function of the uniaxial strain  $\epsilon_u$ . The same definition for uniaxial strain has been used as defined in the numerical section (Equation (4.1)) and the

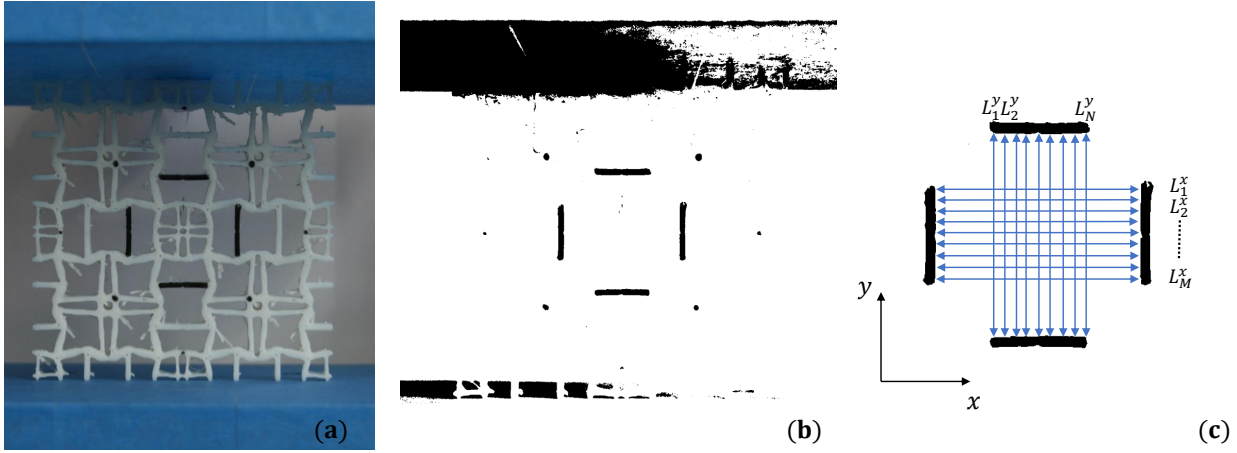


**Figure 5.11:** Procedure to process the image for measuring Poisson's values. (a) Image of the fabricated sample during compression at  $\epsilon_u = 0.5\%$ ; (b) the color to black-white conversion and (c) the image of the frame without noise. The difference in length between the opposite pair of lines has been taken at multiple positions to ensure a sufficient amount of data points.

experimental Poisson's value is defined as

$$v(\epsilon_u) = \frac{\bar{L}_x(\epsilon_u) - \bar{L}_x(\epsilon_u = 0)}{\bar{L}_y(\epsilon_u) - \bar{L}_y(\epsilon_u = 0)} \frac{\bar{L}_y(\epsilon_u = 0)}{\bar{L}_x(\epsilon_u = 0)}, \quad (5.1)$$

where  $\bar{L}_x(\epsilon_u)$  and  $\bar{L}_y(\epsilon_u)$  denote the average lengths between the lines as function of the uniaxial strain and they are defined as

$$\bar{L}_x(\epsilon_u) = \frac{1}{M} \sum_{i=1}^M L_x^i(\epsilon_u) \quad \text{and} \quad \bar{L}_y(\epsilon_u) = \frac{1}{N} \sum_{i=1}^N L_y^i(\epsilon_u), \quad (5.2)$$

with  $M$  and  $N$  the amount of arrows between the horizontal and vertical opposite pair of lines, respectively. The lengths between the opposite pairs of lines in the undeformed configuration are denoted by  $\bar{L}_x(\epsilon_u = 0)$  and  $\bar{L}_y(\epsilon_u = 0)$ . This image processing strategy is executed for all experimentally tested designs. and the corresponding frames (dashed lines in red) from which Poisson's values are calculated are shown in Figure 5.12. To minimize boundary effects (as investigated in Section 4.5), we decided to select a frame which outlines the most central unit cell.

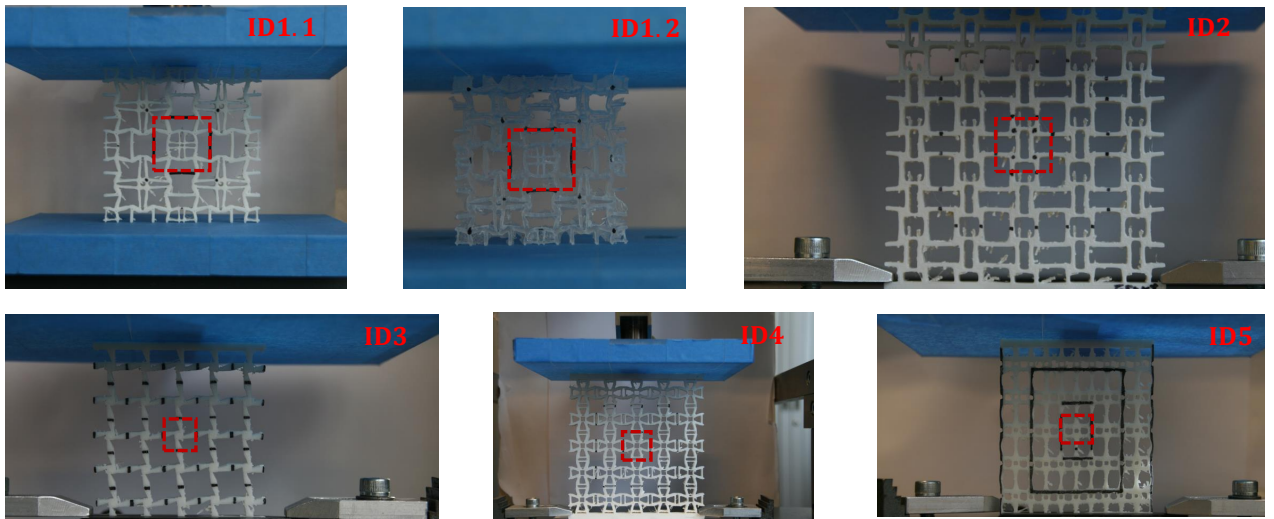


**Figure 5.12:** Measurement frames for auxetic design testing.

### 5.4.3 Results

The experimental outcome is shown in Figure 5.14. Poisson's values as function of the uniaxial strain for 5 fabricated designs are plotted in the most left column. Corresponding compressed configurations are shown at the right column. For completeness, the test results are compared with the numerical outcome as described in Section 4.5. For 5 experimentally compressed auxetic designs the Poisson's values and also the auxetic behavior is consistent with the homogenized value. One kind of chiral design doesn't performs as expected and the underlying reasons are discussed in Section 5.4.4. From the physical tests, the following is observed:

1. For small strains  $\epsilon_u$  the experimental and numerical responses match to a high extent. For increasing displacements in terms of magnitude, the numerical calculated Poisson's values becomes more negative and diverge from the homogenized value. This may be caused by material non-linearities which play to start a role. This kind of non-linearity is not considered in the finite element models and might give another response for finite strains. Note, the Poisson's ratio of design ID2 rapidly changes for increasing strains. This structure is a chiral auxetic with rotating parts which are sensitive for non-linear responses.
2. For increasing uniaxial strains, the experimental responses show an almost constant platform for  $\epsilon_u \geq 1\%$ . This behavior is in line with earlier research [48]. The tendency of the compressed design to become more auxetic (thus lower Poisson's values) is to a lower extent observed in the experimental test.
3. For the sample fabricated with PDMS the response in terms of Poisson's value fluctuates significantly. The very low stiffness of the sample (the Young's modulus is in the order of 1 MPa [17]), makes it difficult to compress the structure gradually with the press. In all probability, the sample will already compress due to its own weight. Moreover, the stress-strain relation for PDMS is non-linear, also for small strains [17]. Thus, material non-linearities are present for all applied displacements. This type of non-linearity is not incorporated into the optimization scheme which might cause these offsets. Also, the non dissolvable parts of the mold that are still present in the sample might contribute to an unreliable outcome.
4. For several experiments, an offset in terms of Poisson's values is founded for  $\epsilon_u \leq 0.5\%$ . Because there is a small gap between the press and the upper part of the sample such deviations arise. This gap is mainly caused by the warping phenomena: the upper surface of the design is not fully flat. This 'settling-effect' is motivated by evaluating the force-strain response as in Figure 5.13. For small strains ( $\epsilon_u \leq 0.5\%$ ) the slope is less steep with respect to larger strains ( $\epsilon_u \geq 0.5\%$ ): the stiffness is significantly lower and indicates that the surface of the press does not make full contact with the samples' surface.

The experiments seems representative since the error bands (or the minimal and maximal deviations for multiple tests) are small or negligible. The Poisson's value response graphs (Figure 5.13) confirms this, because the response curves overlap to a large extent.

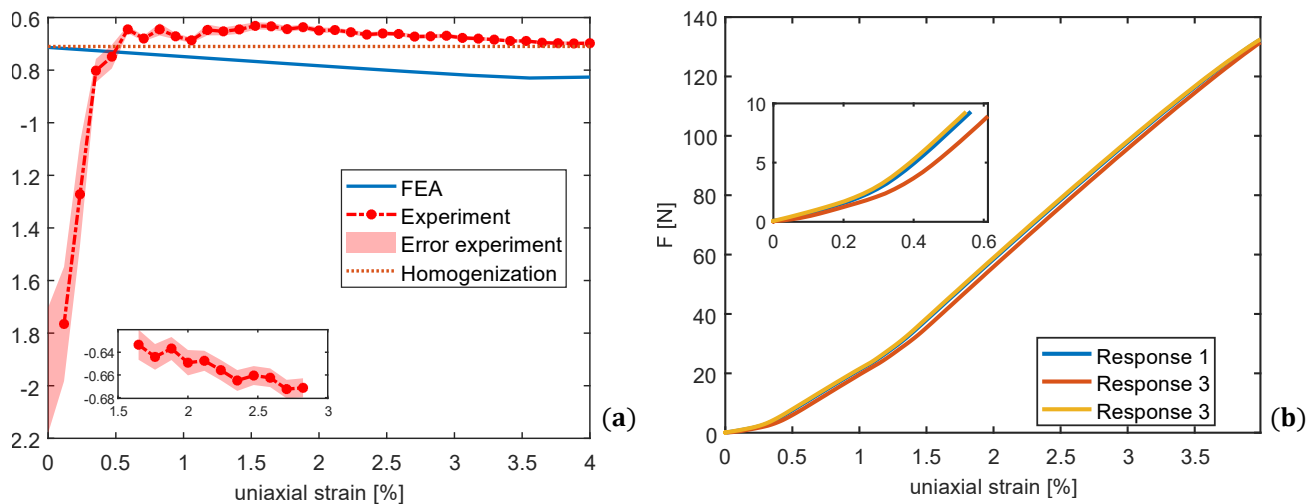
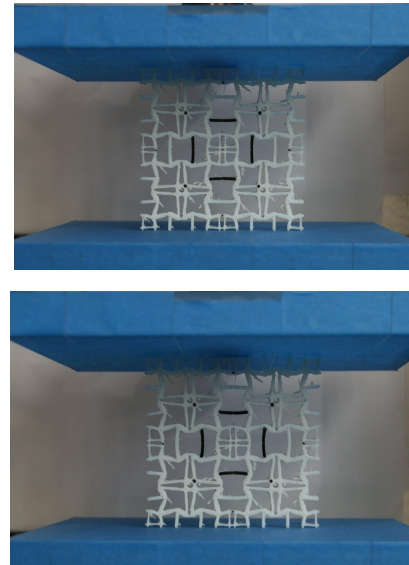
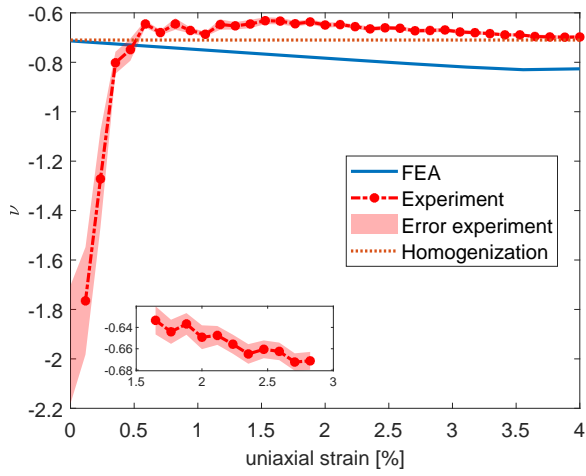
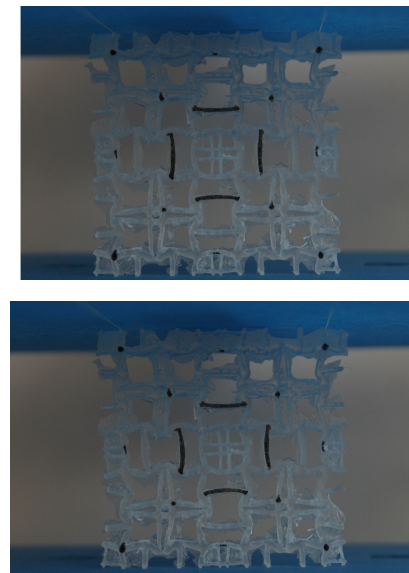
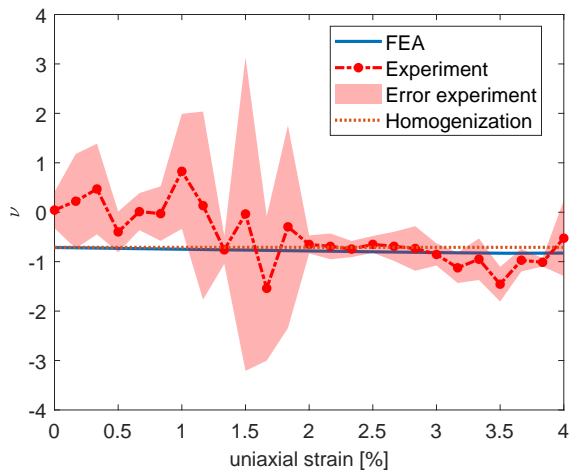


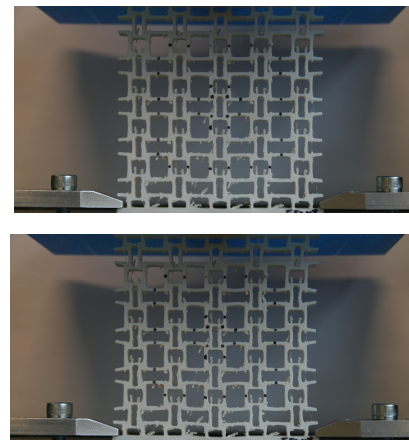
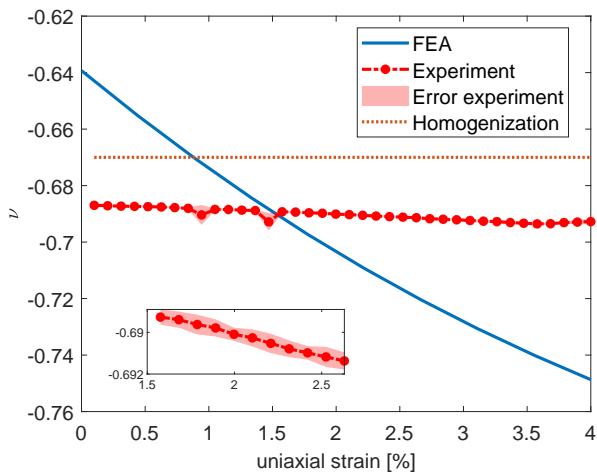
**Figure 5.13:** Applied force as function of uniaxial strain  $\epsilon_u$  for compressing a structure three times (b) and the Poisson's value as function of uniaxial strains (a).



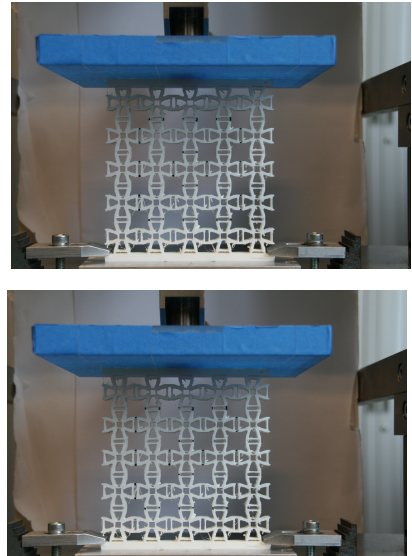
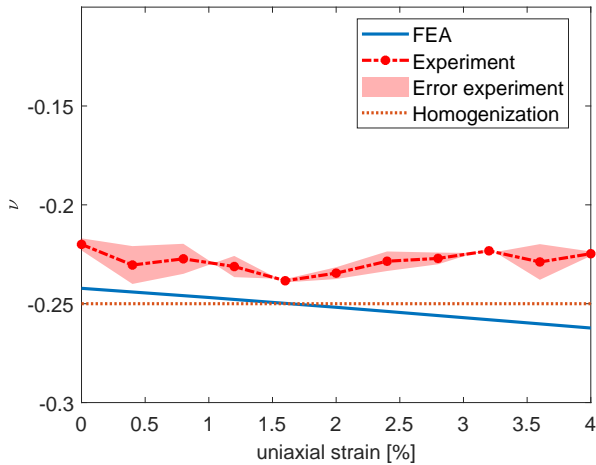
Poisson's values and deformed configuration for design **ID1.1**



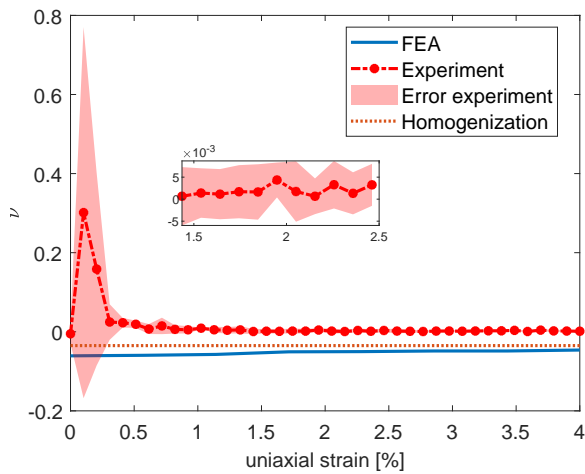
Poisson's values and deformed configuration for design **ID1.2**



Poisson's values and deformed configuration for design **ID2**



Poisson's values and deformed configuration for design ID4



Poisson's values and deformed configuration for design ID5

**Figure 5.14:** Experimental obtained Poisson's values for uniaxial strains until 4 %. All blue lines represent the Poisson's values obtained by simulations using similar boundary conditions. The upper and lower peaks of the error band (shaded area) represents the maximal and minimal measured Poisson's value during the experiment. All red dashed lines denote the homogenized Poisson's values. The right column shows for each design ID the compressed configurations at  $\epsilon_u = 2\%$  and  $\epsilon_u = 4\%$ .

#### 5.4.4 Non-auxetic behavior

The compressive state for design ID3 shows a remarkable configuration. During the first loading steps the structure gradually shrinks, but quite rapidly global buckling occurs. Under a compressive load, the structure has the tendency to fall into a shear mode instead of gradually shrinking in both horizontal and vertical direction. Both, from the experiment and simulation the global buckling mode appear, as shown in Figure 5.15(b) and Figure 5.15(c), respectively. Ideally, the structure must shrink by simultaneous rotations of the disks as in Figure 5.15(a). Consequently, the adjacent ligaments can fold around that disk which results in horizontal shrinkage (orange arrows) and thus auxetic behavior. The non-auxetic behavior can be caused by the following:

- The bending moment executed on the cylindrical part is too small and thus a rotation is not obtained. Due to the small 'arms', insufficient torque is applied on the rotational part.
- Manufacturing errors: the design seems sensitive for geometrical changes in the geometry due to printing errors. Since the cylindrical parts must rotate simultaneously, equal material distribution is preferred. More or less deposited material around the ligaments and/or cylindrical parts might give (less) material at unwanted positions, causing the metamaterial not to perform as expected.
- A similar unit cell is observed in literature and the author also established that this type of auxetic design does not properly shrink for a compressive load [23]. They do not discuss reasons for this behavior, but relevant expressions for the components of the compliance tensor are given. It becomes clear, the compliance for shear is the most dominant term in the compliance tensor which may cause the obtained shear mode.

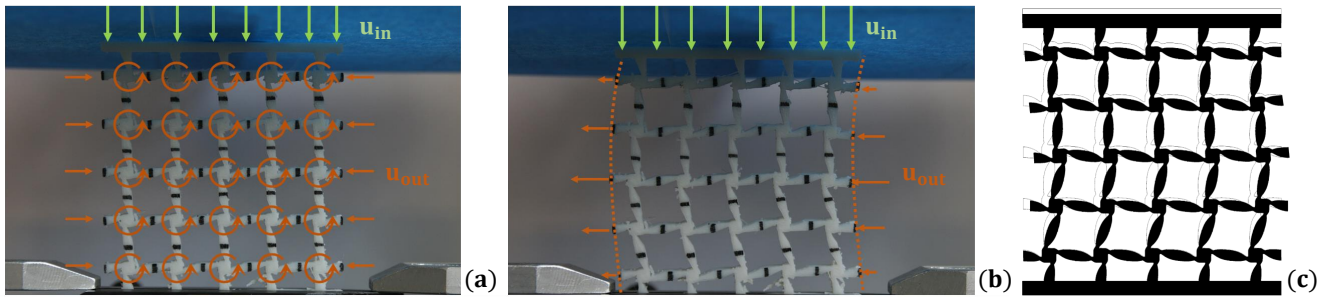


**Figure 5.15:** Expected deformation mechanism (a) and experimentally (b) and numerically (c) obtained deformed configuration. The green and orange arrows denote the direction of the input and output displacements, respectively.

#### 5.4.5 Influence of measuring location

The Poisson's ratios as plotted and discussed in Section 5.4.3 are obtained by tracking marked lines. However, evaluating the Poisson's values by following the locations of points instead of lines during an experiment gives a different outcome. Figure 5.16 plots the result as a function of the uniaxial strain: a systematic error between the homogenized value and the experimental outcome of approximately 15% is found. This might be caused by a (i) measuring frame located near to the boundaries and/or (ii) an insufficient amount of data points from which strains are calculated. The experimental outcome matches with the numerical outcome to a certain extent, so the experiment itself seems to be correctly executed. This outcome motivates the choice to determine auxetic behavior based on multiple points (*e.g.* lines) at the boundaries of a unit cell.

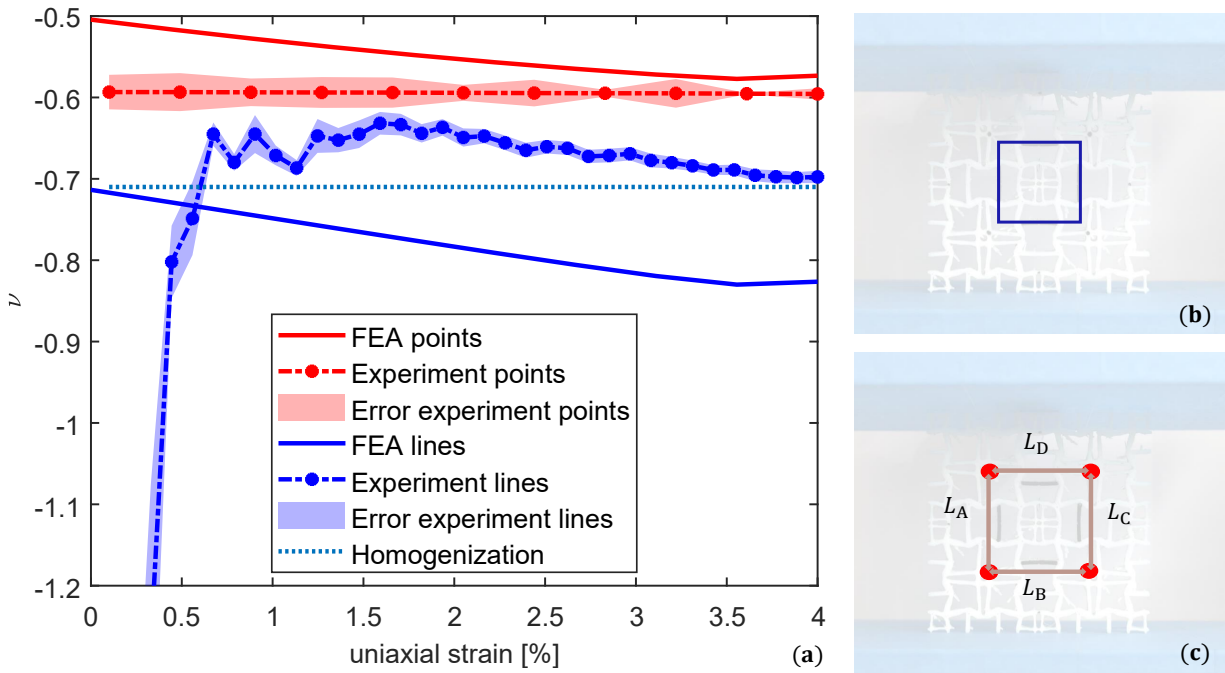


**Figure 5.16:** (a) Poisson's values for increasing uniaxial strain based on measuring displacements between lines and points as shown in (b) and (c), respectively. Poisson's values based on points positions are calculated by  $\nu(\epsilon_u) = \frac{L_D(\epsilon_u) - L_D + L_B(\epsilon_u) - L_B}{L_A(\epsilon_u) - L_A + L_C(\epsilon_u) - L_C} \frac{L_A + L_C}{L_B + L_D}$ , with  $L_A, L_B, L_C$  and  $L_D$  the original lengths.

### 5.4.6 Clamping aspects

During the project improvements for properly clamping the lower part of the sample are made. Initially, the fabricated sample is just placed on a rigid platform without additional clamping mechanisms. However, small movements of the lower part are observed which are undesired. Moreover, a fixed boundary can be representatively modeled and predicted using finite elements. Therefore, it was chosen to fix the lower part of the sample by a so-called 'frog clip'. The clip pushes the sample to the ground by an adjusted screw as in Figure 5.17(c). The clip is connected to the rectangular bar of the sample to not influence the auxetic behavior of the central unit cells.

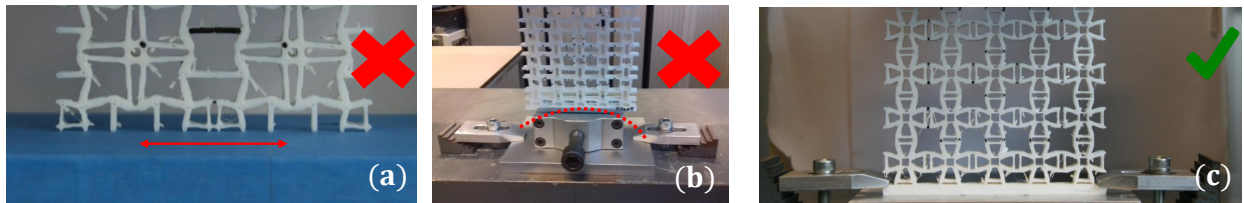


**Figure 5.17:** Clamping possibilities utilized during the project. Releasing the lower section as in (a) may give movements sideways and a clamping as in (b) is only feasible for designs with small horizontal lengths. A structure clamped with the 'frog clamp' (c) is preferable.

# Chapter 6

## Discussion

An enormous amount of knowledge is both applied and gathered in this thesis work. However, obtained knowledge and understanding principles of optimizing auxetic unit cells gave critical thoughts about some of the results. This section starts with a discussion point about the optimization strategy. Further on, shortcomings of the utilized manufacturing technique are discussed, numerical validation aspects are argued and possible causes for discrepancies between the expected and experimentally obtained responses are highlighted.

### 6.1 Optimization

As stated in Section 3.1 the choice of the objective function is supported by existing literature. However, the continuation parameter might influence the optimization routine. Therefore, designs with and without a continuation formulation are compared with each other. In the work of Zhang, the objective is defined as a squared difference problem between the target stiffness matrix and the homogenized stiffness matrix [46]. One of their results (without continuation) is compared with an optimal layout (with continuation), using the same parameter settings. Both designs are highly comparable in terms of final layout, as shown in Figure 6.1. It is concluded that, at least for this case, the continuation parameter has no significant influence on the result, and it even appears unnecessary.

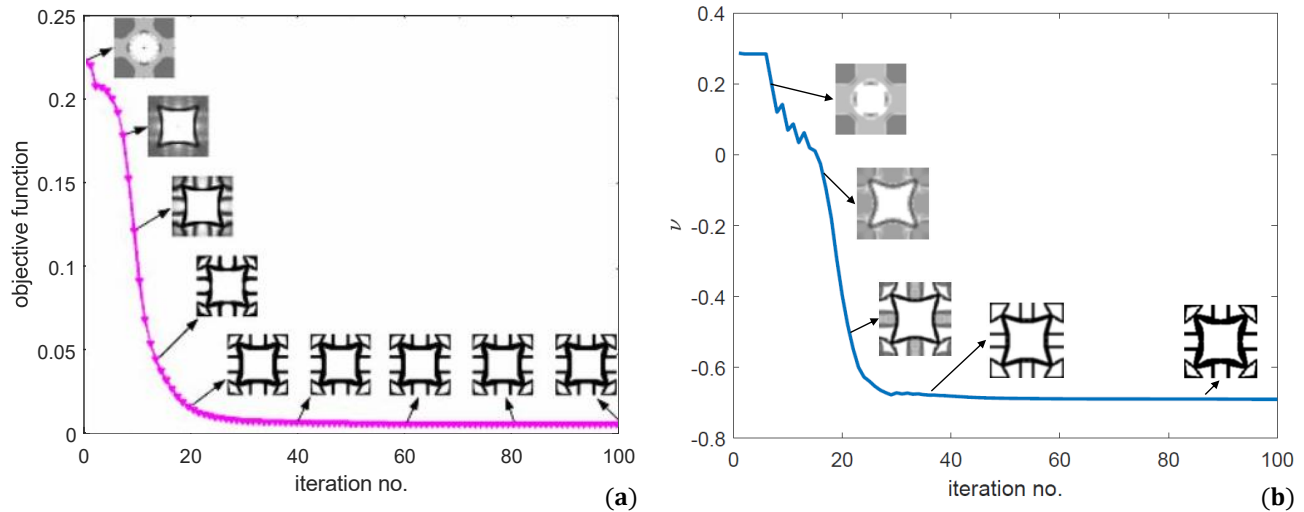


**Figure 6.1:** Iteration history of a design [46] without continuation terms in the objective (a) and with continuation terms in the objective (b).

## 6.2 Manufacturing

In Section 5.2 and Section 5.3 a variation in print settings is investigated: the print orientation of the specimens. The experiment results in observations and *possible* causes for discrepancies between expectations and the results. Only, for the dominance of this printing parameter a conclusions can be drawn: the print orientation highly influences the mechanism performance. In all probability, other print parameters do have an effect on the performance of the fabricated specimen, as already investigated to some extent by Chacon *et al.* [6]. As a consequence, no firm conclusions about the dominance of a variation in print orientations compared to other print setting can be made.

## 6.3 Numerical validation

Towards the numerical validation, two discussion points arise: geometrically non-linear effects and asymmetry in terms of auxetic behavior.

### 6.3.1 Geometrically non-linear effects

The Poisson's values from Section 4.5.2 have the tendency to become more negative for increasing uniaxial strain. Also, for increasing strains the Poisson's values diverge from the target value. In all probability, this is caused by the applied geometrically non-linearities during the numerical studies. This type of non-linearity is applied to obtain the compressed configuration for finite strains. However, during the optimization procedure structures are optimized in the linear regime and geometrical non-linearities are **not** taken into account. As a consequence, their auxetic response is only valid for small deflections.

### 6.3.2 Asymmetry of auxetic designs

In Section 4.4 we demonstrated that the cause of assymetrical auxetic response lies in geometrical asymmetry. Moreover, an asymmetric division of the (finite) elements of the geometry might also contribute to some asymmetry. For a linear elastic analysis, buckling might not occur and this phenomena is untouched. However, for a geometrically non-linear analysis (which is performed in Section 4.5.2) buckling might come in for compressing a structure with finite strains. When this is the case, one would expect that the asymmetry vanishes to a certain extent for a tensile load. To investigate the sensitivity of a design with respect to buckling, a design with system size  $n = 5$  is both compressed and extended for a set of uniaxial strains. Deformed configurations are obtained by utilizing the loading scenario as in Figure 4.7 and geometrical non-linearities are applied to observe possible buckling effects. The Poisson's value differences for each unit cell individually are represented by the contour plot as in Figure 6.2(a). For an extension of the design, the asymmetry almost vanishes while compression results in different Poisson's values along the symmetry line. To quantify the asymmetry for increasing applied displacements, Poisson's values differences of opposite unit cells are defined by

$$S_{Aa} = \sum_{i=1}^5 A_i - a_i, \quad (6.1a)$$

$$S_{Bb} = \sum_{i=1}^5 B_i - b_i, \quad (6.1b)$$

with  $A_i$ ,  $B_i$ ,  $a_i$  and  $b_i$  values according to Figure 6.2(a). Values for  $S$  are expressed in percentage points: the higher the value for  $S$ , the more asymmetry is present in the deformed configuration. This numerical study clearly shows that for increasing uniaxial strains, a compressed design becomes more asymmetric in terms of Poisson's values. More interestingly, in-plane buckling occurs at the most lower unit cells Figure 6.2(b) which probably declares the asymmetric response. However, an extended structure does show a tendency to a symmetric response for increasing strains. Numerical studies with higher magnitudes of uniaxial strains would be interesting to continue the graphs in Figure 6.2(c). However, material non-linearities must be incorporated to come up with representative responses for further extension of the design.

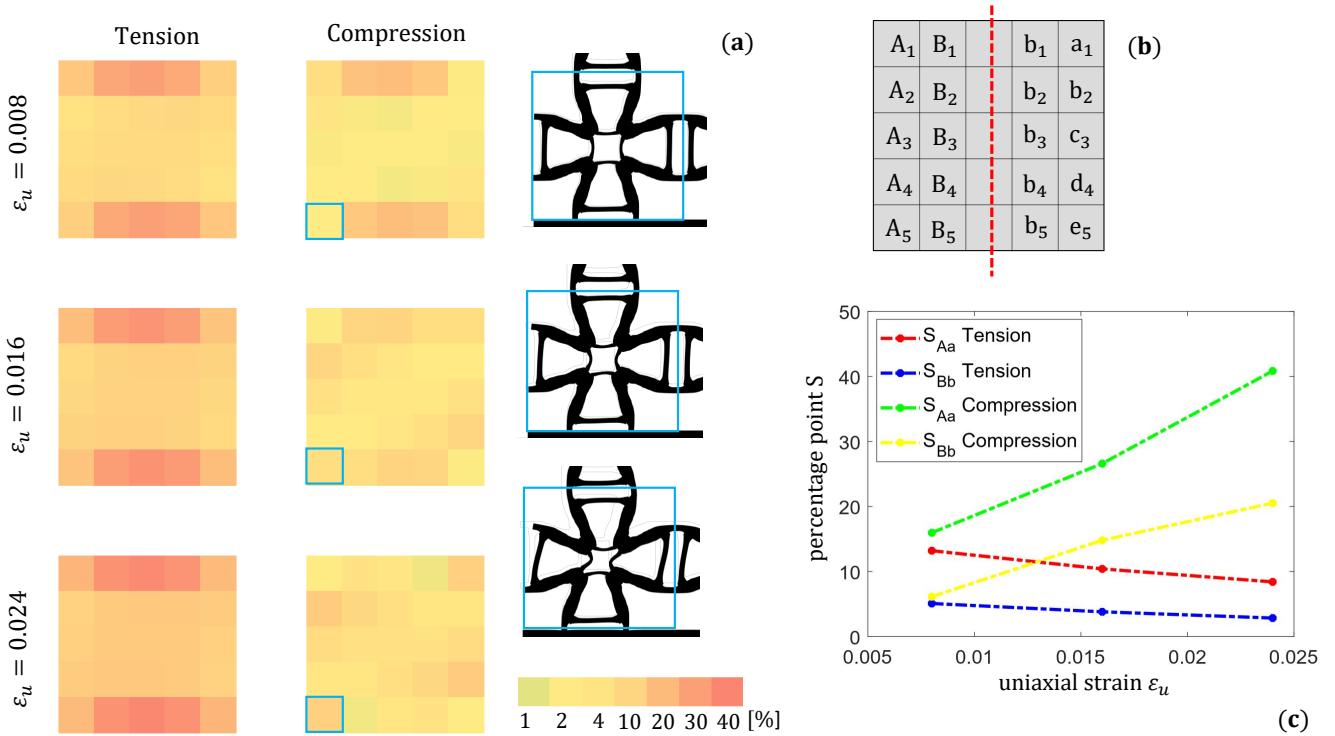


**Figure 6.2:** (a) Poisson's values differences with respect to the target value for both extending and compressing a patch of 5 by 5 unit cells. Buckled configurations (enlarged with a factor 3) of the most lower left unit cell are shown in the blue boxes. The variety on colors at pairs of sides Aa and Bb clearly shows the asymmetry for compressive loads. (b) Labeling of the unit cells with the symmetry axis (red dashed line). (c) Differences between opposite column of unit cells (Aa and Bb) expressed in percentage points.

## 6.4 Experiments

In this project the focus is on generating and fabricating auxetic unit cells in 2D. For exploratory purposes this is beneficial since less expensive optimizations are needed and it allows for a better understanding of the working principle of the design compared to 3D. The working principles of 3D auxetic designs might be harder to explain, visualize and experiment with. However, out-of-plane effects are not incorporated during the optimization, but exist in reality. As shown, the warping of the fabricated part (Table 5.1) does give an inhomogeneous thickness of the printed structure. Moreover, an additional out-of-plane source comes in while compressing a structure: out-of-plane bending or eventually buckling. The latter is not observed during the experiment. Nevertheless, the fabricated design is not infinitely stiff in out-of-plane direction and this brings some errors.

Multiple causes might contribute to the fluctuating response of the PDMS sample during the experiment. In addition to non-linear material and geometrical effects, the own weight of the sample might dominate the auxetic response during the compression test. The latter is also not taken into account during the optimization and might contribute to discrepancies between the expected and observed auxetic response. The stiffness of the PDMS design is at least two orders lower in terms of magnitude compared to auxetic designs made using FLEX65 filament. Since Poisson's values mainly significantly differ during small strains ( $\epsilon_u \leq 2\%$ ), the press might not fully exert displacements on the top surface of the structure which gives a divergence in auxetic response.

# Chapter 7

## Conclusions

The reader is reminded of the research aim as stated in the introduction:

**The generation and numerical and experimental validation of manufacturable and functional mechanical metamaterials using topology optimization.**

This research aim is evaluated by going through the tasks as in Figure 7.1. Firstly, optimization results and aspects are outlined. Further on, conclusions are drawn from numerical studies. Finally, manufacturing aspects are addressed and conclusions are drawn about the experimental outcome from compression tests of auxetic designs. Below, the main conclusions for each task are given in bullets and the corresponding contribution of the author is summarized at the end of each task.

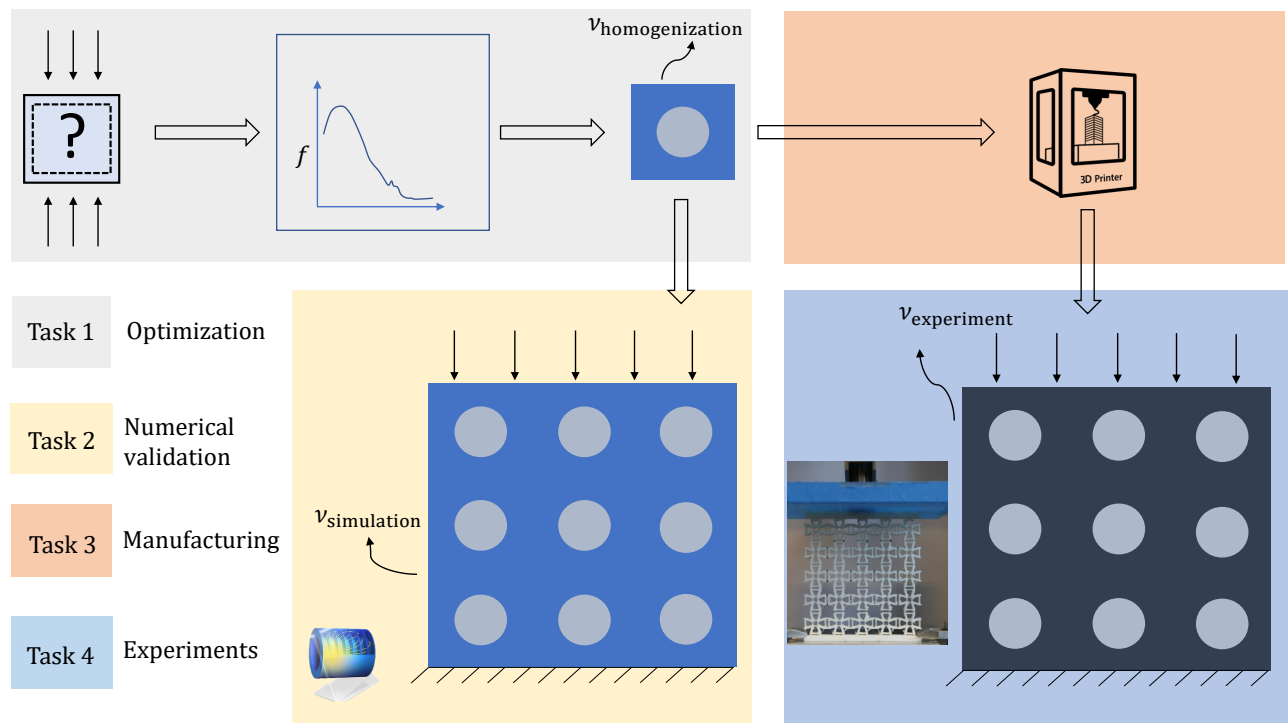


**Figure 7.1:** Approach to optimize, fabricate and validate auxetic designs during this thesis project.

## Optimization

From the utilized energy-based topology optimization approach with periodic boundary conditions, the following conclusions are drawn:

- The use of a continuation term in the objective function works well.
- The optimized layout of a unit cell is sensitive to the initial material distribution. As a consequence, novel auxetic unit cells are optimized for varying initial density distributions.
- Novel auxetic geometries are generated exhibiting homogenized Poisson's values between 0 and -0.71.
- The optimization formulation is capable of generating chiral auxetic designs.
- Some of the optimized layouts show similarities with existing geometries, designed without a TO procedure, which confirms the optimization strategy makes sense.

**This research expands the collection of repeatable auxetic geometries by utilizing a topology optimization approach under periodic boundary conditions. Both re-entrant and chiral structures can be optimized by a suitably chosen initial density field.**

## Numerical validation

The conclusions drawn from the numerical studies are as follows:

- Poisson's values calculated based on energy versus deformation result in the same values for a square unit cell and equivalent values for an auxetic unit cell.
- An auxetic design with sliding boundary conditions better represents periodic behavior near to the boundaries compared with a design with fixed boundaries.
- The Poisson's value in a patch of unit cells at the most central cell is hardly affected by the type of boundary conditions.
- In a finite patch of unit cells, the most central cell shows a Poisson's value close to the periodic case.
- In a finite patch of unit cells, Poisson's values of the boundary cells differs the most from the target value.
- For uniaxial strains until 0.5%, the obtained Poisson's value for a simulated compression test matches the homogenized Poisson's value to a large extent; a typical difference of 3% was observed in this regime.
- For uniaxial strain above 0.5% the Poisson's ratios of re-entrant auxetic structures show a stable response with respect to the applied strain, whereas the auxetic response of chiral structures rapidly changes.

**Strategies to measure a Poisson's value based on energy and deformations are developed and both methods result in equivalent values. This research clearly shows that for a patch of auxetic unit cells the choice of boundary conditions influences the auxetic behavior throughout the design.**

## Manufacturing

From manufacturing specimens with the fused deposit modeling technique the conclusions are:

- The orientation of a notch flexure specimen with respect to the print plate significantly influences the stiffness of the as-fabricated sample; a maximal spread in terms of stiffnesses of 18% was found.
- The orientation of a compliant mechanism with respect to the print plate affects the output trajectory of the as-fabricated mechanism. For a target ratio of 0 between horizontal and vertical displacements, a ratio of 0.0075 was observed for a design printed flat on the build plate. A ratio of 0.12 was found for a design printed under a 30 degree angle with respect to the build plate.
- The fabricated samples do show minute differences in geometry, mainly caused by manufacturing tolerances.

- It is feasible to fabricate an auxetic design made out PDMS. However, an auxetic design made out this material is too compliant for experimental testing.

**The print orientation highly influences both the stiffness and output trajectory of specimens fabricated with the fused deposition modeling technique.**

## Experiments

The best practices are used to compress auxetic designs with minimized test uncertainties. The outcome of physical experiments of 5 auxetic designs result in the following conclusions:

- The experimentally obtained Poisson's values match the homogenized value to a certain extent: typical differences of 8% are found.
- The Poisson's value calculation based on marked lines results in a more representative response compared to those measured based on marked points. A deviation between the experimental and homogenization-based Poisson's value was found of 4 and 17% for the lines and point measure, respectively.
- Discrepancies between the experimental and homogenized outcome during the first loading steps are caused by small gaps between the sample and press.

For a particular chiral design, interesting discrepancies were found between the experimental and expected response. An in-plane buckled configuration during compression was observed. The main causes of this behavior may lie in the sensitivity for manufacturing errors and the large compliance in shear.

**This project experimentally showed that novel auxetic geometries, fabricated with the fused deposition modeling technique, do give expected auxetic behavior under a compressive load.**

## Final conclusion

Taking the above four aspects into account, the main conclusion of this this work is as follows:

Numerical investigations show that a finite amount of unit cells already resembles a mechanical metamaterial. This work shows that effective material properties are not representative at every position at the design for a fixed boundary. However, a representative test frame in the center of the design is present and must be chosen to evaluate auxetic behavior. The experimentally tested novel auxetic designs generated new knowledge towards the validation of mechanical metamaterials. It is shown that the upcoming and user-friendly additive manufacturing technique, FDM, is suited to generate and validate optimized 2D geometries. Moreover, the experimental outcome is case-dependent and simulations of experiments is recommended for every new design.

Fabrication and experimental validation of 3D geometries is seen as a next challenge, since the print orientation highly influences the performance of a printed mechanism. Also, validation of fabricated specimens remains challenging, thus recommendations for further research are listed in the next chapter.

# Chapter 8

## Outlook

The relevant recommendations and points of attention for future work are as follows:

1. The experimental validation of mechanical metamaterials for large applied strains,  $\epsilon_u \geq 5\%$ . Research towards auxetic structures for large strains is quite novel. Recently, Zhang and Sun developed a method to design such structures using non-linear homogenization [45]. Relevant experimental studies are mainly performed for structures designed without a structural optimization method and performed once [7].
2. The generation and validation of mechanical metamaterials with auxetic properties in three dimensions. The existing optimization formulation can be expanded for optimizing 3D unit cells and a possible implementation for periodic boundary conditions in three dimensions is proposed by Mi *et al.* [12].
3. The design of a compliant mechanism, located around the boundaries of an auxetic design, to mimic the boundary conditions as used in TO. The boundary conditions as used in the experiment highly limit the displacements at the clamped sections. Also, the free boundaries at the most left and right are not periodic, which is the case in the optimization routine.
4. The continuation of research towards AM of compliant mechanisms using FDM techniques. This production technique is quite novel and unexplored, so design possibilities and challenges are open. Next to printing orientations, the dominance of other print parameters must be investigated.
5. The design of auxetic structures for stiff and lightweight purposes. This application field is unaddressed in current research, whereas auxetic structures seem beneficial for generating stiff and lightweight structures. Literature suggests that the flexural rigidity (and also the stiffness) significantly increases for materials with high absolute Poisson's values [26]. This thought is motivated by deriving expressions for an in-plane bending dominated structure. The deflection  $\delta$  of such a structure is

$$\delta = \frac{12FL^3(1 - \nu^2)}{Et^3}, \quad (8.1)$$

which brings the following relation:

$$\delta \sim 1 - \nu^2. \quad (8.2)$$

The dependence of the Poisson's ratio on the deflection becomes clear from this relation. A Poisson's value close to -1 could give negligible deflections. Thus, an increase of the absolute Poisson's value would give a decrease in deflections and allows the design of more stiff structures. Designing both stiff and lightweight structures is often preferable for structural design problems. Therefore, a preliminary case study is performed for in-plane bending of a plate with a support structure. This case is quite general, but obtained knowledge can be used to develop novel support structures for *e.g.* adaptive mirrors. So, a 2D finite element analysis, using plane-strain conditions is performed with boundary conditions as in Figure 8.1. The structure consists of a slab aluminium and a underlying material with unit material properties. A parametric sweep of Poisson's ratios is applied and maximal deflections are evaluated; the response is plotted in Figure 8.1. The graph shows a significant effect of materials with Poisson's values towards -1 and the outcome supports further research towards auxetic structures for lightweight applications.

6. The fabrication of designs obtained with the so-called *robust formulation* [38]. Consequently, under- and overprinting of the deposited material can be captured while utilizing an FDM technique. The manufacturing tolerances can to some extent be incorporated into the optimization scheme while utilizing a Heaviside threshold projection. Especially for FDM techniques, this approach seems advantageous since parts are not very accurately fabricated.

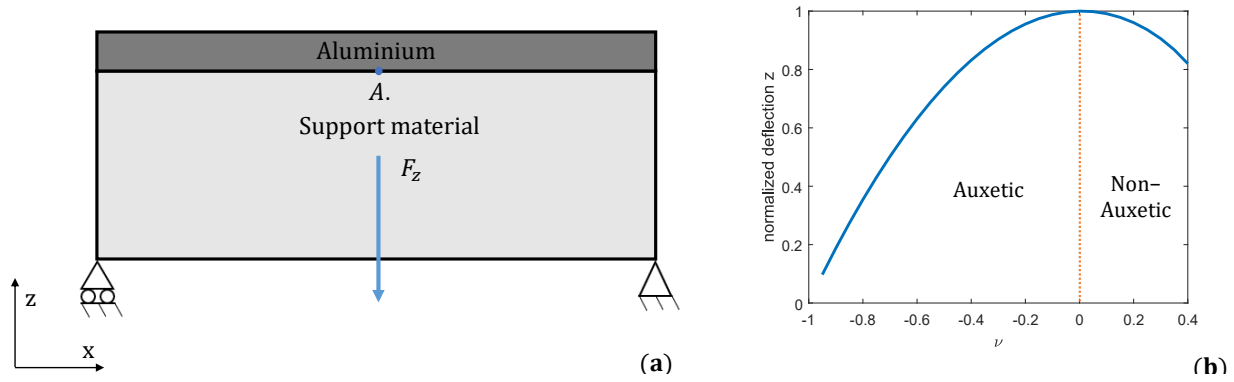


**Figure 8.1:** Normalized deflections at point A for a variety on Poisson's ratios (b) using a loading scenario as in (a). The load represents a body force of both the support material and the aluminum slab. Note that the outcome shows min-max deflections with ratio of 1:10 which is highly unrealistic. The support material is assumed as completely solid, whereas auxetic structures do have void regions in the material.

7. In cooperation with Penn State university an effort has been made to assemble a buildplate with specimens which can be fabricated out *e.g.* aluminium or metal using selective laser sintering. The fabricated parts made by another print technique can be tested on their material properties such that valuable knowledge can be gathered. The designed buildplate is envisioned as in Figure 8.2 and it will hopefully be printed soon.

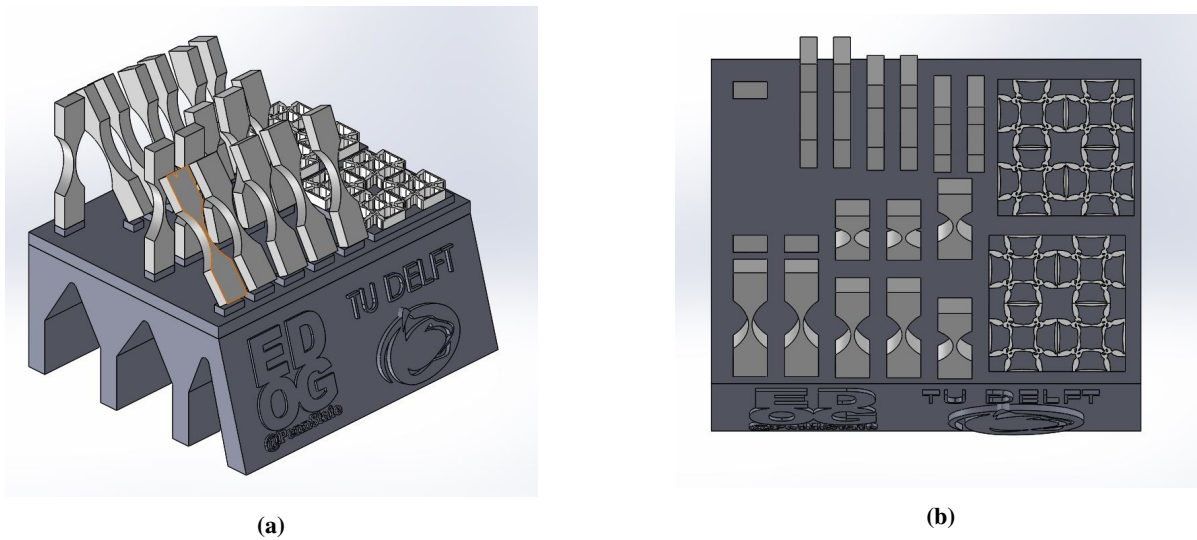


**Figure 8.2:** (a) An isometric view and (b) top view of the designed buildplate.

8. A TO implementation which allows for multi-scale optimization. For varying microstructures in the design (at the bulk scale) boundary effects can be captured and novel auxetic structures can be explored. Existing designs obtained by a multi-scale TO are already reported and can be extended for material design problems [32, 36, 47].

# Appendices

# Appendix A

## Derivations of design sensitivities

### A.1 Design sensitivities for minimal compliance

Design sensitivities for minimal compliance design problems with respect to the design vector  $\rho$  are derived from the objective function

$$f = \mathbf{F}^\top \mathbf{u}, \quad (\text{A.1})$$

which is subjected to the equilibrium equations

$$\mathbf{K}\mathbf{u} = \mathbf{F}, \quad (\text{A.2})$$

with  $\mathbf{K}$ ,  $\mathbf{u}$  and  $\mathbf{F}$  the symmetric global stiffness matrix, element displacement vector and force vector, respectively. The objective function is written as an augmented response for efficiently computing of the sensitivities. The corresponding Lagrangian is defined as

$$\mathcal{L} = \mathbf{F}^\top \mathbf{u} + \lambda^\top (\mathbf{K}\mathbf{u} - \mathbf{F}), \quad (\text{A.3})$$

with  $\lambda$  the Lagrange multipliers. The partial derivate of Equation (A.3) with respect to  $\rho$  is

$$\frac{\partial \mathcal{L}}{\partial \rho} = \frac{\partial \mathbf{F}^\top}{\partial \rho} \mathbf{u} + \mathbf{F}^\top \frac{\partial \mathbf{u}}{\partial \rho} + \lambda^\top \left( \frac{\partial \mathbf{K}}{\partial \rho} \mathbf{u} + \mathbf{K} \frac{\partial \mathbf{u}}{\partial \rho} - \frac{\partial \mathbf{F}}{\partial \rho} \right). \quad (\text{A.4})$$

Terms which consist terms of  $\frac{\partial \mathbf{u}}{\partial \rho}$  are grouped and it is assumed forces are independent of the design variables. These conditions bring the following expression

$$\frac{\partial \mathcal{L}}{\partial \rho} = \cancel{\frac{\partial \mathbf{F}^\top}{\partial \rho} \mathbf{u}} + \lambda^\top \left( \frac{\partial \mathbf{K}}{\partial \rho} \mathbf{u} - \cancel{\frac{\partial \mathbf{F}}{\partial \rho}} \right) + \frac{\partial \mathbf{u}}{\partial \rho} \left( \mathbf{F}^\top + \lambda^\top \mathbf{K} \right). \quad (\text{A.5})$$

To avoid computation of state vector derivatives,  $\lambda$  is chosen such that  $\frac{\partial \mathbf{u}}{\partial \rho}$  vanishes. Therefore, the following condition must holds:

$$\frac{\partial \mathbf{u}}{\partial \rho} \left( \mathbf{F}^\top + \lambda^\top \mathbf{K} \right) = 0, \quad (\text{A.6})$$

which results in

$$\lambda^\top = -\mathbf{F}^\top \mathbf{K}^{-1}, \quad (\text{A.7})$$

and backsubstitution of the outcome for  $\lambda^\top$  of Equation (A.7) in Equation (A.5) gives

$$\frac{\partial \mathcal{L}}{\partial \rho} = -\mathbf{F}^\top \mathbf{K}^{-1} \frac{\partial \mathbf{K}}{\partial \rho} \mathbf{u}, \quad (\text{A.8})$$

and using Equation (A.2) gives the expression for the design sensitivities

$$\frac{\partial \mathcal{L}}{\partial \rho} = -\mathbf{u}^\top \mathbf{K}^\top \mathbf{K}^{-1} \frac{\partial \mathbf{K}}{\partial \rho} \mathbf{u}. \quad (\text{A.9})$$

Finally, the sensitivities of the design variables with respect to the objective function arise as

$$\frac{\partial f}{\partial \rho} = -\mathbf{u}^\top \frac{\partial \mathbf{K}}{\partial \rho} \mathbf{u}. \quad (\text{A.10})$$

## A.2 Design sensitivities for maximal output displacement

For design problems in which output displacements at output ports are optimized, the objective is defined as

$$f = \mathbf{L}^T \mathbf{u}, \quad (\text{A.11})$$

with  $\mathbf{L}$  values which take zero except the element which corresponds to the output degree of freedom. Also, for this type of problem the adjoint method has been utilized. The augmented response is defined as

$$\mathcal{L} = \mathbf{L}^T \mathbf{u} + \lambda^T (\mathbf{K}\mathbf{u} - \mathbf{F}), \quad (\text{A.12})$$

and corresponding sensitivities with respect to the design variables

$$\frac{\partial \mathcal{L}}{\partial \rho} = \mathbf{L}^T \frac{\partial \mathbf{u}}{\partial \rho} + \lambda^T \left( \frac{\partial \mathbf{K}}{\partial \rho} \mathbf{u} + \mathbf{K} \frac{\partial \mathbf{u}}{\partial \rho} - \frac{\partial \mathbf{F}}{\partial \rho} \right), \quad (\text{A.13})$$

or in rearranged form under the assumption forces are independent of the design variables

$$\frac{\partial \mathcal{L}}{\partial \rho} = \lambda^T \left( \frac{\partial \mathbf{K}}{\partial \rho} \mathbf{u} - \frac{\partial \mathbf{F}}{\partial \rho} \right) + \frac{\partial \mathbf{u}}{\partial \rho} (\mathbf{L}^T + \lambda^T \mathbf{K}). \quad (\text{A.14})$$

To avoid computation of state vector derivatives,  $\lambda$  is chosen such that  $\frac{\partial \mathbf{u}}{\partial \rho}$  vanishes. Therefore, the condition must hold

$$\frac{\partial \mathbf{u}}{\partial \rho} (\mathbf{L}^T + \lambda^T \mathbf{K}) = 0, \quad (\text{A.15})$$

which results in

$$\lambda^T = -\mathbf{L}^T \mathbf{K}^{-1}. \quad (\text{A.16})$$

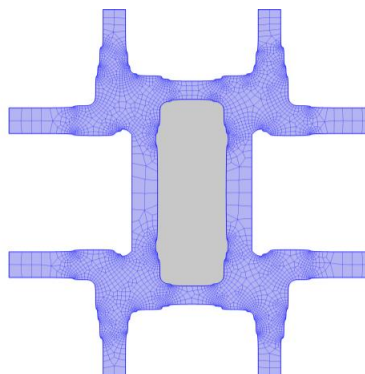
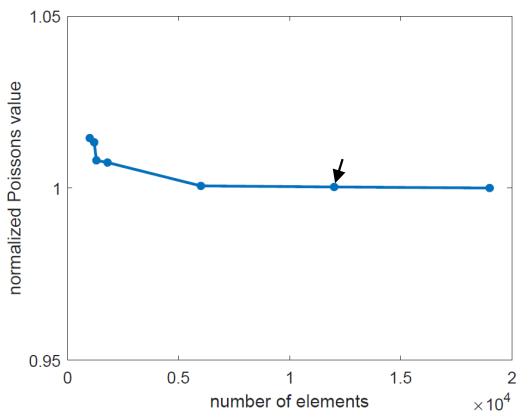
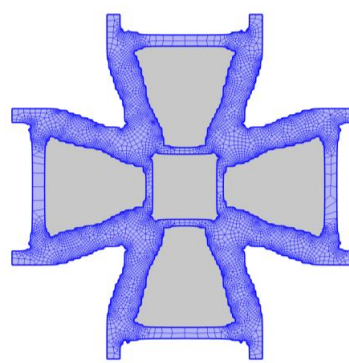
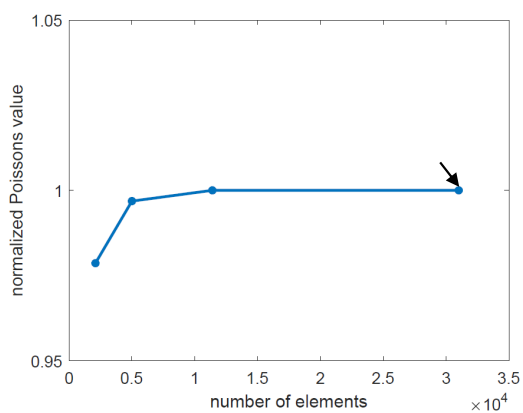
Backsubstitution of  $\lambda$ , as obtained from Equation (A.16), in Equation (A.13) gives

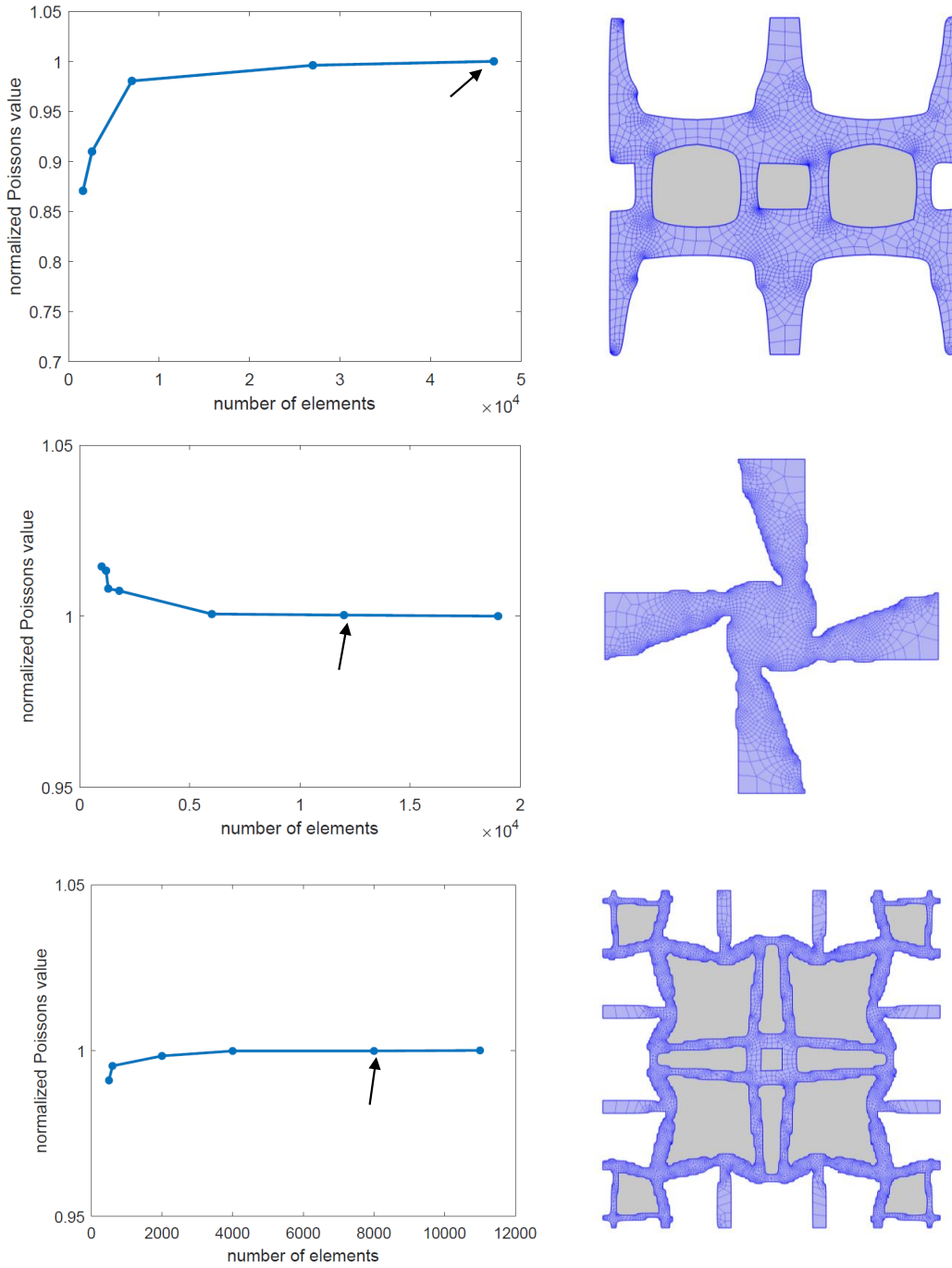
$$\frac{\partial \mathcal{L}}{\partial \rho} = \lambda^T \frac{\partial \mathbf{K}}{\partial \rho} \mathbf{u}, \quad (\text{A.17})$$

in which  $\frac{\partial \mathcal{L}}{\partial \rho}$  represents the design sensitivities for this type of design problem.

## Appendix B

# Mesh convergence of auxetic unit cells

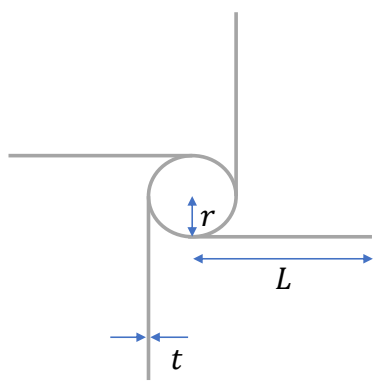
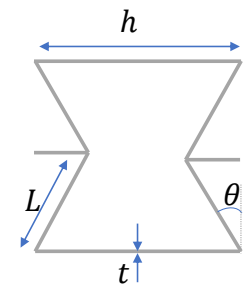




**Figure B.1:** Convergence for increasing discretization sizes and discretized unit cells. The design are discretized (in blue) with the amount of finite element as pointed in the corresponding graph.

# Appendix C

## Auxetic structures comparison

|                                     | Chiral auxetic                                                                     | Re-entrant auxetic                                                                   |
|-------------------------------------|------------------------------------------------------------------------------------|--------------------------------------------------------------------------------------|
|                                     |  |  |
| DoF's                               | 3 (principal directions+rotation)                                                  | 2 (principal directions)                                                             |
| DoF's are constrained by            | Number of ligaments                                                                | Magnitude of design parameters                                                       |
| Deformation mechanism               | Stretching and bending                                                             | Stretching, bending and hinging [22]                                                 |
| Main deformation mechanism          | Rotation                                                                           | Hinging and bending                                                                  |
| In-plane bending stiffness          | Relative low                                                                       | Relative high                                                                        |
| <i>Poisson's ratio aspects</i>      |                                                                                    |                                                                                      |
| Dependent on applied strain?        | Yes                                                                                | No                                                                                   |
| Sensitive for thickness variations? | Yes                                                                                | Yes and more sensitive w.r.t. chiral auxetics                                        |
| Dependent on geometrical angles?    | No                                                                                 | Yes                                                                                  |

**Table C.1:** Comparison between chiral and re-entrant auxetic structures. Characteristics are consulted (if not explicitly stated) from Kolken *et al.* [18].

## Appendix D

### Notch flexures

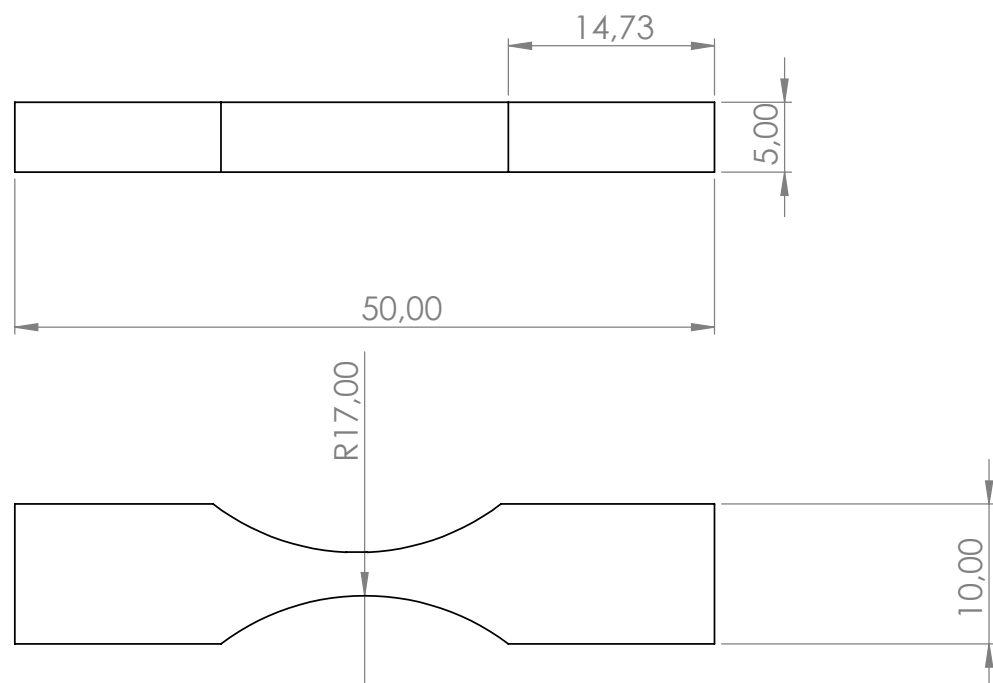
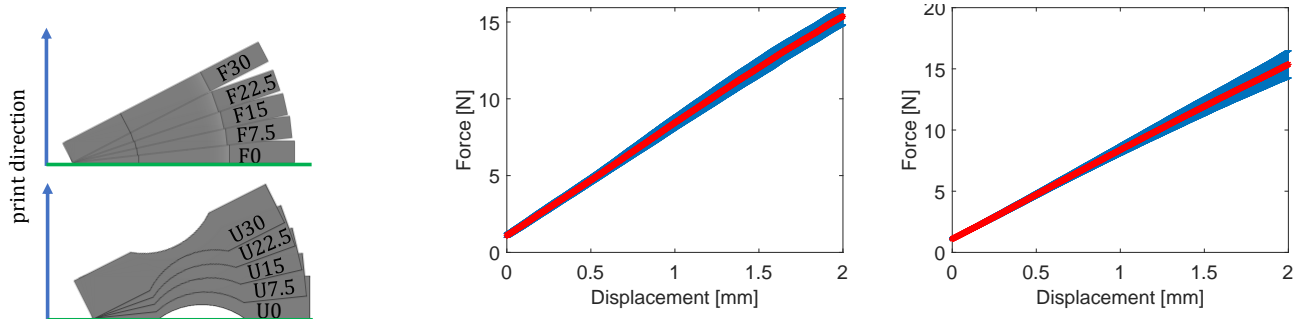


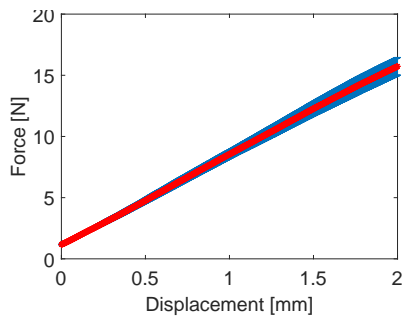
**Figure D.1:** Dimensions of the notch flexure.



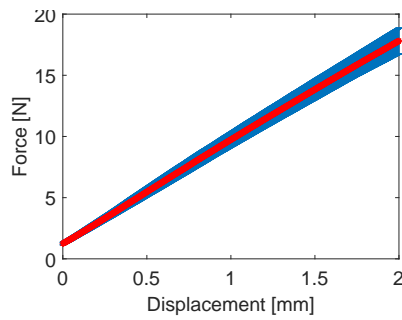
(a) Orientation of the fabricated notch flexures

(b) F0

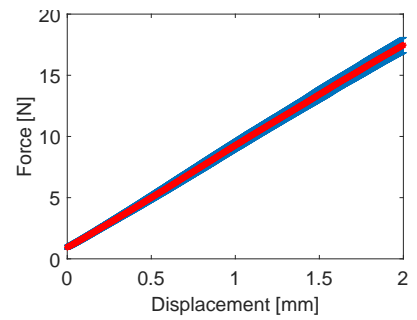
(c) F7.5



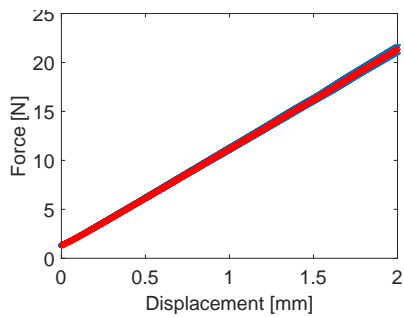
(d) F15



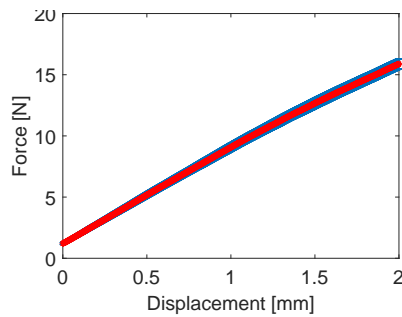
(e) F22.5



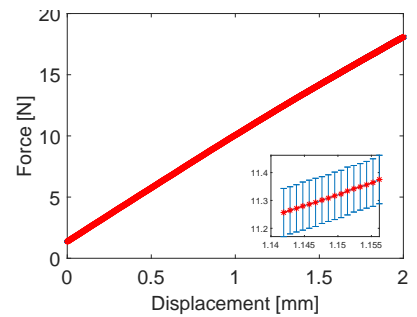
(f) F30



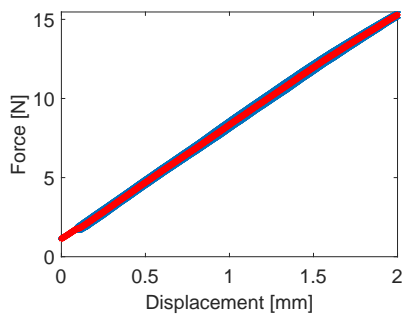
(g) U0



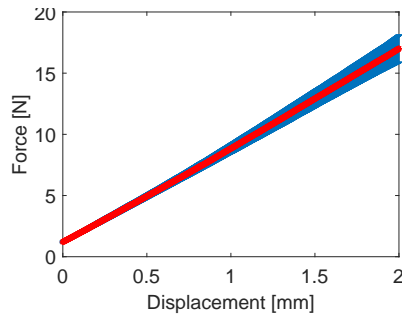
(h) U7.5



(i) U15



(j) U22.5



(k) U30

**Figure D.2:** (a) Print orientations of the specimens with respect to the print plate (green line). (b)-(k) Force-displacements responses for each printed orientation obtained from the three-point bending test. The upper and lower values of the blue (error) band denote the maximal and minimal tested forces. 68

## Appendix E

# Design of a compliant inverter

The well-know 99 lines of code in MATLAB for design problems using TO is used to design a compliant inverter [31]. This code is initially purposed for obtaining layouts with minimal compliance. Slightly changes in the existing code are made to optimize designs for compliant mechanism synthesis. The goal of the optimization is to maximize the displacement  $u_{\text{out}}$  performed on a workpiece modelled by a spring with stiffness  $k_{\text{out}}$ . The optimization formulation is defined as

$$\begin{aligned}
 & \underset{\rho}{\text{minimize}} && f(\rho) = \mathbf{I}^T \mathbf{u} \\
 & \text{subject to} && \mathbf{K}\mathbf{u} = \mathbf{F} \\
 & && \frac{1}{|\Omega|} \sum_{e=1}^N v_e \rho_e \leq V_{\text{max}} \\
 & && 0 \leq \rho_e \leq 1, \quad e = 1, \dots, N
 \end{aligned} \tag{E.1}$$

with  $\mathbf{K}$  the global stiffness matrix,  $\mathbf{u}$  and  $\mathbf{F}$  the displacement vector and external force vector respectively. The design variables are denoted by  $\rho$ . All values of the vector  $\mathbf{I}$  are zero except the element which corresponds to the output degree of freedom, which is taken as one. The allowable volume of the design domain is bounded by 30% volume fraction,  $V_{\text{max}}$ . The material interpolation scheme (SIMP) is identical as fully explained in Section 2.4. Sensitivities of the objective function with respect to the design variables are calculated by the adjoint sensitivity analysis as derived in Section A.2. The design domain with corresponding boundary conditions are in Figure E.1 and parameter settings for testing benchmark compliant mechanism designs using TO are consulted from literature [38].

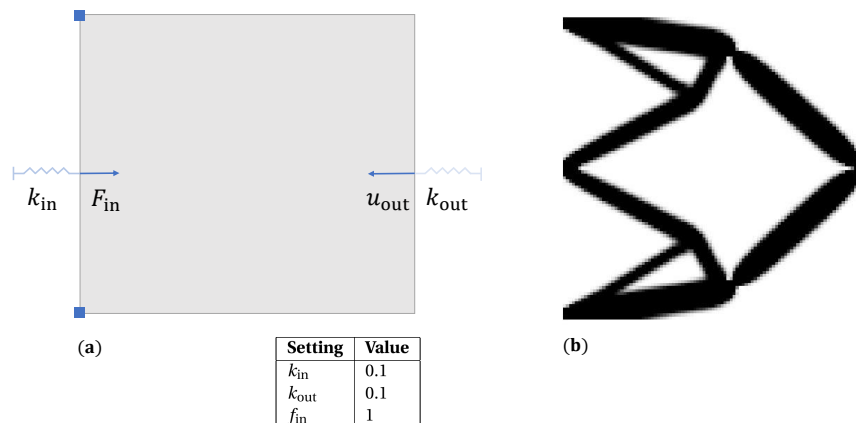


**Figure E.1:** Compliant inverter problem definition and final design. (a) Design domain and boundary conditions for the compliant inverter with corresponding parameter values. (b) Final density distribution of the compliant inverter

# Bibliography

- [1] Datasheet FLEX65 filament. URL: <http://www.lay3rs.nl/wp-content/uploads/2015/08/Datasheet-FLEX65-filament-Lay3rs.pdf>.
- [2] A. Alderson, K.L. Alderson, D. Attard, K.E. Evans, R. Gatt, J.N. Grima, W. Miller, N. Ravirala, C.W. Smith, and K. Zied. Elastic constants of 3-, 4- and 6-connected chiral and anti-chiral honeycombs subject to uniaxial in-plane loading. *Composites Science and Technology*, 70(7):1042–1048, jul 2010. URL: <https://linkinghub.elsevier.com/retrieve/pii/S0266353809002814>, doi:10.1016/j.compscitech.2009.07.009.
- [3] Erik Andreassen, Anders Clausen, Mattias Schevenels, Boyan S. Lazarov, and Ole Sigmund. Efficient topology optimization in MATLAB using 88 lines of code. *Structural and Multidisciplinary Optimization*, 43(1):1–16, 2011. arXiv:9605103, doi:10.1007/s00158-010-0594-7.
- [4] Erik Andreassen, Boyan S. Lazarov, and Ole Sigmund. Design of manufacturable 3D extremal elastic microstructure. *Mechanics of Materials*, 1(69):1–10, 2014. doi:10.1016/j.mechmat.2013.09.018.
- [5] Katia Bertoldi, Vincenzo Vitelli, Johan Christensen, and Martin Van Hecke. Flexible mechanical metamaterials. *Nature Reviews Materials*, 2, 2017. doi:10.1038/natrevmats.2017.66.
- [6] J.M. Chacón, M.A. Caminero, E. García-Plaza, and P.J. Núñez. Additive manufacturing of PLA structures using fused deposition modelling: Effect of process parameters on mechanical properties and their optimal selection. *Materials & Design*, 124:143–157, jun 2017. URL: <https://linkinghub.elsevier.com/retrieve/pii/S0264127517303143>, doi:10.1016/j.matdes.2017.03.065.
- [7] Anders Clausen, Fengwen Wang, Jakob S. Jensen, Ole Sigmund, and Jennifer A. Lewis. Topology Optimized Architectures with Programmable Poisson’s Ratio over Large Deformations. *Advanced Materials*, 27(37):5523–5527, oct 2015. URL: <http://doi.wiley.com/10.1002/adma.201502485>, doi:10.1002/adma.201502485.
- [8] Andrew D. Cramer, Vivien J. Challis, and Anthony P. Roberts. Microstructure interpolation for macroscopic design. *Structural and Multidisciplinary Optimization*, 53(3):489–500, 2016. doi:10.1007/s00158-015-1344-7.
- [9] Engineers Edge. Common Plastic Molding Design Material Specification, 2000. URL: <http://www.engineersedge.com/plastic/materials{ }common{ }plastic.htm>.
- [10] Janssen Precision Engineering. Precision point, 1996. URL: <https://www.janssenprecisionengineering.com/wp-content/uploads/Flexure-hinge-or-elastic-hinge.pdf>.
- [11] Juan A Gallego and Just Herder. Synthesis Methods in Compliant Mechanisms : An Overview. In *Mechanisms and Robotics Conference*, number January, Delft, 2010. doi:10.1115/DETC2009-86845.
- [12] Jie Gao, Hao Li, Liang Gao, and Mi Xiao. Topological shape optimization of 3D micro-structured materials using energy-based homogenization method. *Advances in Engineering Software*, 116:89–102, feb 2018. URL: <https://linkinghub.elsevier.com/retrieve/pii/S0965997817308086>, doi:10.1016/j.advengsoft.2017.12.002.
- [13] Jie Gao, Huipeng Xue, Liang Gao, and Zhen Luo. Topology optimization for auxetic metamaterials based on isogeometric analysis. *Computer Methods in Applied Mechanics and Engineering*, 2019. doi:10.1016/j.cma.2019.04.021.
- [14] Jos~ Miranda Guedes and Noboru Kikuchi. Preprocessing and postprocessing for materials based on the homogenization method with adapte finite elements. Technical report, University of Michigan, 1990. URL: <https://deepblue.lib.umich.edu/bitstream/handle/2027.42/28363/0000128.pdf?sequence=1&isAllowed=y>.

- [15] Jakob S. Jensen. *Topology optimization*, volume 540. 2012. doi:10.1007/978-3-7091-1309-7\_3.
- [16] Nikos T. Kaminakis, Georgios A. Drosopoulos, and Georgios E. Stavroulakis. Design and verification of auxetic microstructures using topology optimization and homogenization. *Archive of Applied Mechanics*, 85(9-10):1289–1306, 2015. URL: <https://link.springer.com/content/pdf/10.1007/s00419-014-0970-7.pdf>, doi:10.1007/s00419-014-0970-7.
- [17] Myeongsub Kim, Byeong Ui Moon, and Carlos H. Hidrovo. Enhancement of the thermo-mechanical properties of PDMS molds for the hot embossing of PMMA microfluidic devices. *Journal of Micromechanics and Microengineering*, 23(9), 2013. doi:10.1088/0960-1317/23/9/095024.
- [18] H. M.A. Kolken and A. A. Zadpoor. Auxetic mechanical metamaterials. *RSC Advances*, 7(9):5111–5129, 2017. doi:10.1039/c6ra27333e.
- [19] Lirong Lu, Takashi Yamamoto, Masaki Otomori, Takayuki Yamada, Kazuhiro Izui, and Shinji Nishiwaki. Topology optimization of an acoustic metamaterial with negative bulk modulus using local resonance. *Finite Elements in Analysis and Design*, 72:1–12, 2013. URL: <http://dx.doi.org/10.1016/j.finel.2013.04.005>, doi:10.1016/j.finel.2013.04.005.
- [20] Yanhong Ma, Fabrizio Scarpa, Dayi Zhang, Bin Zhu, Lulu Chen, and Jie Hong. A nonlinear auxetic structural vibration damper with metal rubber particles. *Smart Materials and Structures*, 22(8), 2013. doi:10.1088/0964-1726/22/8/084012.
- [21] Manufacturin Guide. Fused Deposition Modeling, 2001. URL: <https://www.manufacturingguide.com/en/fused-deposition-modeling-fdm>, doi:10.1201/9780203910795.ch8.
- [22] I.G. Masters and K.E. Evans. Models for the elastic deformation of honeycombs. *Composite Structures*, 35(4):403–422, aug 1996. URL: <https://www.sciencedirect.com/science/article/pii/S0263822396000542>, doi:10.1016/S0263-8223(96)00054-2.
- [23] Davood Mousanezhad, Babak Haghpanah, Ranajay Ghosh, Abdel Magid Hamouda, Hamid Nayeb-Hashemi, and Ashkan Vaziri. Elastic properties of chiral, anti-chiral, and hierarchical honeycombs: A simple energy-based approach. *Theoretical and Applied Mechanics Letters*, 6(2):81–96, mar 2016. URL: <https://linkinghub.elsevier.com/retrieve/pii/S2095034916000210>, doi:10.1016/j.taml.2016.02.004.
- [24] OLLYDUNCANI. Auxetic materials in sports applications. URL: <https://engineeringsport.co.uk/2018/11/29/auxetic-materials-in-sports-applications/>.
- [25] Kepeng Qiu, Weihong Zhang, Matthieu Domaszewski, and Dominique Chamoret. Topology optimization of periodic cellular solids based on a superelement method. *Engineering Optimization*, 41(3):225–239, 2009. doi:10.1080/03052150802414718.
- [26] D. Rayneau-Kirkhope. Stiff auxetics: Hierarchy as a route to stiff, strong lattice based auxetic meta-materials. *Scientific Reports*, 8(1):1–10, 2018. URL: <http://dx.doi.org/10.1038/s41598-018-30822-x>, doi:10.1038/s41598-018-30822-x.
- [27] Alex Remennikov, Dulara Kalubadanage, Tuan Ngo, Priyan Mendis, Gursel Alici, and Andrew Whittaker. Development and performance evaluation of large-scale auxetic protective systems for localised impulsive loads. *International Journal of Protective Structures*, 2019. doi:10.1177/2041419619858087.
- [28] D. Schurig, J. J. Mock, B. J. Justice, S. A. Cummer, J. B. Pendry, A. F. Starr, and D. R. Smith. Metamaterial electromagnetic cloak at microwave frequencies. *Science*, 2006. arXiv:arXiv:1011.1669v3, doi:10.1126/science.1133628.
- [29] Ole Sigmund. Design of material structures using topology optimization. *Department of Solid Mechanics*, (August), 1994.
- [30] Ole Sigmund. Tailoring materials with prescribed elastic properties. Technical report, Technical University of Denmark, 1994. URL: <https://pdf.xuebalib.com/xuebalib.com.12180.pdf>.
- [31] Ole Sigmund. A 99 line topology optimization code written in matlab. *Structural and Multidisciplinary Optimization*, 21(2):120–127, 2001. doi:10.1007/s001580050176.

- [32] Raghavendra Sivapuram, Peter D Dunning, and & H Alicia Kim. Simultaneous material and structural optimization by multiscale topology optimization. URL: <https://link.springer.com/content/pdf/10.1007/978-1-4919-1519-x.pdf>, doi:10.1007/s00158-016-1519-x.
- [33] Lorenzo Valdevit, Katia Bertoldi, James Guest, and Christopher Spadaccini. Architected materials: synthesis, characterization, modeling and optimal design. Technical report, Univeristy of California, 2019. doi:10.1557/jmr.2018.18.
- [34] Jason Valentine, Shuang Zhang, Thomas Zentgraf, Erick Ulin-Avila, Dentcho A. Genov, Guy Bartal, and Xiang Zhang. Three-dimensional optical metamaterial with a negative refractive index. *Nature*, 455(7211):376–379, sep 2008. URL: <http://www.nature.com/doi/10.1038/nature07247>, doi:10.1038/nature07247.
- [35] K. P. Vemuri, F. M. Canbazoglu, and P. R. Bandaru. Guiding conductive heat flux through thermal metamaterials. *Applied Physics Letters*, 105(19):193904, nov 2014. URL: <http://aip.scitation.org/doi/10.1063/1.4901885>, doi:10.1063/1.4901885.
- [36] Panagiotis Vogiatzis, Shikui Chen, Xiao Wang, Tiantian Li, and Lifeng Wang. Topology optimization of multi-material negative Poisson’s ratio metamaterials using a reconciled level set method. *CAD Computer Aided Design*, 83(October):15–32, 2017. URL: <http://dx.doi.org/10.1016/j.cad.2016.09.009>, doi:10.1016/j.cad.2016.09.009.
- [37] Fengwen Wang. Systematic design of 3D auxetic lattice materials with programmable Poisson’s ratio for finite strains. *Journal of the Mechanics and Physics of Solids*, (114):303–318, 2018. doi:10.1016/j.jmps.2018.01.013.
- [38] Fengwen Wang, Boyan Stefanov Lazarov, and Ole Sigmund. On projection methods, convergence and robust formulations in topology optimization. *Structural and Multidisciplinary Optimization*, 43(6):767–784, 2010. URL: <https://link.springer.com/article/10.1007/s00158-010-0602-y>, doi:10.1007/s00158-010-0602-y.
- [39] Q. Wang, N. Mitsumura, Q. Chen, A. Sarkar, H. Kurokawa, K. Sekiguchi, and K. Sugiyama. Additive Manufacturing Technologies. In *International Journal of Sustainable Development and Planning*, volume 9, chapter 6, pages 658–668. Springer, New York, 2nd edition, 2014. doi:10.2495/SDP-V9-N5-658-668.
- [40] Wikipedia. Auxetics, 2019. URL: <https://en.wikipedia.org/wiki/Auxetics>.
- [41] Liang Xia and Piotr Breitkopf. Design of materials using topology optimization and energy-based homogenization approach in Matlab. *Structural and Multidisciplinary Optimization*, 2015. doi:10.1007/s00158-015-1294-0.
- [42] Guodong Zhang, Kapil Khandelwal, Graduate Student, and Associate Professor. Computational Design of Finite Strain Auxetic Metamaterials via Topology Optimization and Nonlinear Homogenization. Technical report. URL: <https://arxiv.org/ftp/arxiv/papers/1905/1905.00482.pdf>.
- [43] Huikai Zhang, Yangjun Luo, and Zhan Kang. Bi-material microstructural design of chiral auxetic metamaterials using topology optimization. *Composite Structures*, 195(March 2019):232–248, 2018. doi:10.1016/j.compstruct.2018.04.058.
- [44] Huikai Zhang, Yangjun Luo, and Zhan Kang. Bi-material microstructural design of chiral auxetic metamaterials using topology optimization. *Composite Structures*, 195:232–248, jul 2018. URL: <https://linkinghub.elsevier.com/retrieve/pii/S0263822318306792>, doi:10.1016/j.compstruct.2018.04.058.
- [45] Weihong Zhang and Shiping Sun. 6 th World Congresses of Structural and Multidisciplinary Optimization Scale-Related Topology Optimization from Unit Cell Homogenization to Superelement Model. Technical report. URL: <https://pdfs.semanticscholar.org/5dd3/b0995c3abf104abcfbec9a4bcc30ef4772d.pdf>.
- [46] Yan Zhang, Mi Xiao, Hao Li, and Liang Gao. Topology optimization of material microstructures using energy-based homogenization method under specified initial material layout †. *Journal of Mechanical Science and Technology*, 33(2):677–693, 2019. URL: [www.springerlink.com/content/1738-494x](http://www.springerlink.com/content/1738-494x), doi:10.1007/s12206-019-0123-6.
- [47] B O Zhu, Elina Skouras, Desai Chen, and Wojciech Matusik. Two-Scale Topology Optimization with Microstructures. Technical report. URL: <https://arxiv.org/pdf/1706.03189.pdf>, arXiv:1706.03189v1.
- [48] Hongming Zong, Hongying Zhang, Yiqiang Wang, Michael Yu, and Jerry Y H Fuh. On two-step design of microstructure with desired Poisson ’ s ratio for AM. *Materials & Design*, 159:90–102, 2018. doi:10.1016/j.matdes.2018.08.032.